Design of an electrochemical cell for In-Situ infrared spectroscopy of the carbon dioxide reduction reaction

Jorrit Kroes

Sustainable Energy Technology

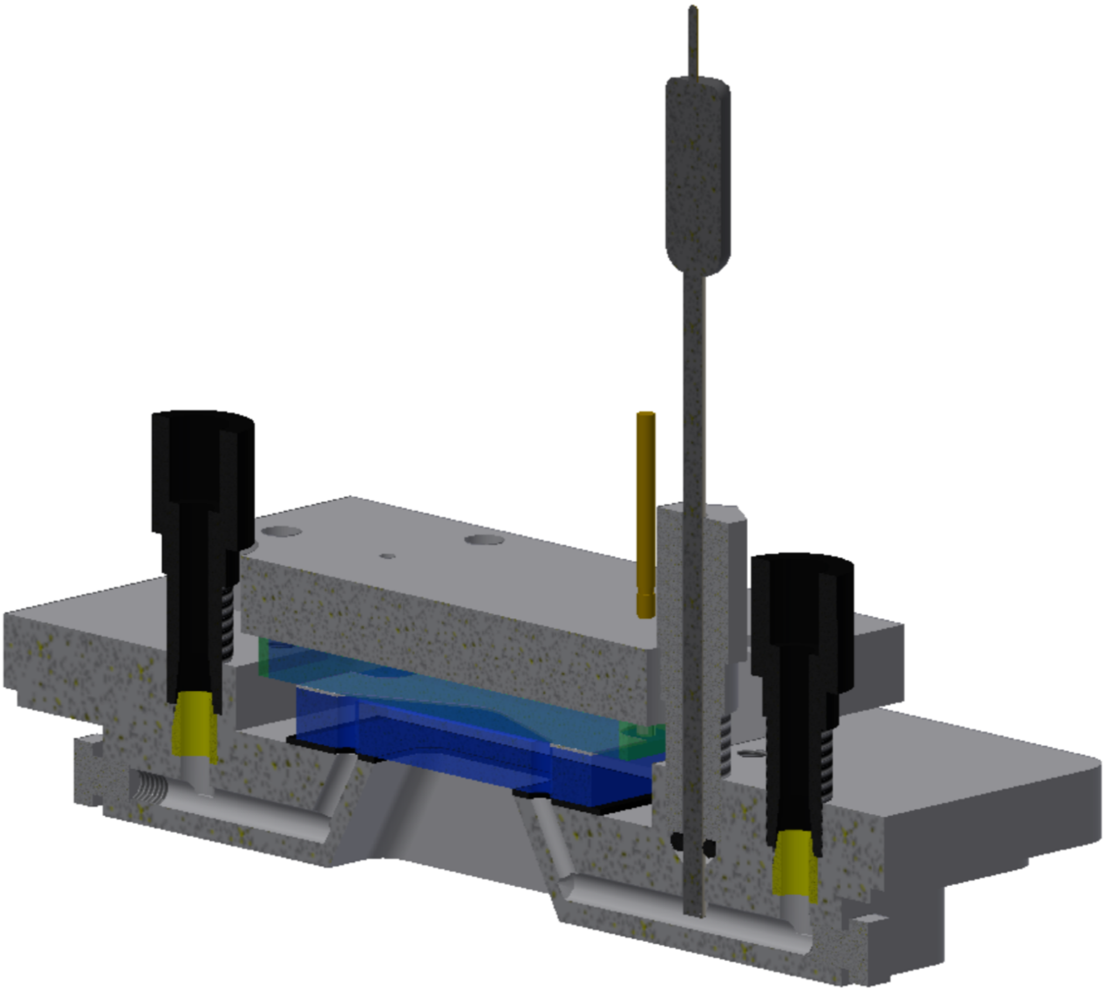

TU Delft

24 January 2018

Design of an electrochemical cell for In-Situ infrared spectroscopy of the carbon dioxide reduction reaction

By

J.H. Kroes

in partial fulfilment of the requirements for the degree of

Master of Science
in Sustainable Energy Technology

at the Delft University of Technology,
to be defended publicly on Thursday March 1, 2018 at 10:00 AM.

Supervisors:	Dr. W.A. Smith	(MECS, TU Delft)
	N.J. Firet	(MECS, TU Delft)
Thesis committee:	Prof. Dr. B. Dam	(MECS, TU Delft)
	Dr. W.A. Smith	(MECS, TU Delft)
	Dr. R. Kortlever	(P&E, TU Delft)

Abstract

The worlds energy demand is increasing however, the majority of the energy supply is still based on fossil fuels. The consumption of fossil fuels results in the emission of carbon dioxide which is one of the main greenhouse gases responsible for the ongoing climate change. In order to reduce the carbon dioxide emissions, more and more energy is produced in a renewable way. Mainly from solar and wind energy. This energy is however intermittent in character and comes in the form of electricity. To overcome the intermittency, the excess produced electricity has to be stored in an efficient reversible way, so that the energy can released again when it is needed. One possible solution that tackles both problems is the electrochemical reduction of carbon dioxide in aqueous electrolytes into highly valuable chemicals, or so called solar fuels. In this study, a new infrared spectroelectrochemical cell with an easy exchangeable electrocatalyst is developed to study the reaction mechanism on a silver catalyst in 0.1 M KCl and 0.1 M $KHCO_3$ electrolytes at applied potentials of -1.4, -1.6 and -1.8 V vs a Ag/AgCl reference electrode. The performance of the new developed cell is compared to the already proven ATR cell configuration. Investigation of the infrared signal strength showed high infrared signals at angles of incidence of the infrared beam between 30° and 45°. The measured infrared absorption spectra in the thin layer flow cell show three absorption bands which are also present in the obtained infrared absorption spectra of the ATR cell. In the ATR spectra however, three further infrared absorption bands can be observed. Due to the lower number of absorption bands present in the FTIR spectra measured in the new designed thin layer flow cell, it can be concluded that despite the high IR signal no new insights on the reaction mechanism of the carbon dioxide reduction reaction can be acquired.

Acknowledgements

I would like to thank Wilson Smith of the MECS group for giving me the opportunity to perform my graduation research project in the field of energy conversion. Further, I would like to express my gratitude to my daily supervisor Nienke Firet for her guidance during this project, helping me with the interpretation of the IR absorption spectra, the provision of the XRD and AFM data and the critical feedback on my report. I would also like to thank Bernard Dam and Ruud Kortlever for being part of the MSc thesis committee and their time and effort for assessing my report. Last but not least, I would like to thank Joost Middelkoop and Herman Schreuders for converting my ideas for the new spectroelectrochemical cell in a technical drawing, so that the new cell could be fabricated, and teaching me how to operate the AJA and PREVAC magnetron sputtering systems, to produce the silver and platinum electrodes, respectively. As both, the fabrication of the new spectroelectrochemical cell and the production of the electrodes were key parts in this study, the performed research would not have been possible without their help.

List of abbreviations

Abbreviation	Definition
AFM	Atomic force microscopy
ATR	Attenuated total reflection
CE	Counter electrode
FT	Fourier-transform
HER	Hydrogen evolution reaction
IR	Infrared
OC	Open circuit
RE	Reference electrode
RHE	Reversible hydrogen electrode
RPM	Rounds per minute
SEIRA	Surface enhanced infrared absorption
SERS	Surface enhanced Raman scattering
SHE	Standard hydrogen electrode
WE	Working electrode
XRD	X-ray diffraction

List of symbols

Symbol	Name	Unit
d_p	Penetration depth of the evanescent wave	[nm]
E	Applied potential	[V]
E_{cell}^0	Standard cell potential	[V]
E_{anode}	Potential of the half reaction at the anode	[V]
$E_{cathode}$	Potential of the half reaction at the cathode	[V]
E_{cell}	Theoretical cell potential	[V]
E_{RHE}	Potential with respect to the reversible hydrogen electrode	[V]
f	Frequency	[Hz]
I	Current	[mA]
J	Current density	[mA cm^{-2}]
n_1	Refractive index of the ATR crystal	[-]
n_2	Refractive index of the sample	[-]
Q	Flow rate	[mL min^{-1}]
t	Time	[s]
θ_e	Effective angle of incidence	[°]
θ_f	Face angle of the ATR crystal	[°]
θ_s	Set angle on the ATR accessory	[°]
λ	Wavelength	[nm]
v	Wavenumber	[cm^{-1}]

Table of Contents

Abstract 1
Acknowledgements 1
List of abbreviations 3
List of symbols 3
1. Introduction 9
2. Literature review 11
  2.1. Reduction of atmospheric carbon dioxide 11
  2.2. Electrochemical reduction of CO_2 12
    2.2.1. Required electric potential 12
    2.2.2. Hydrogen evolution reaction 13
    2.2.3. Electrolytes for the CO_2 reduction reaction 14
    2.2.4. Sustainable and economic viable CO_2 reduction products 15
    2.2.5. The effect of the used electrocatalyst on the CO_2 reduction products 16
    2.2.6. Electrochemical reduction of CO_2 on a silver electrode 17
  2.3. Vibrational spectroscopy 18
    2.3.1. Theory 18
    2.3.2. Infrared spectroscopy 19
    2.3.3. Raman spectroscopy 20
    2.3.4. Surface enhanced vibrational spectroscopy 21
  2.4. In-Situ infrared spectroelectrochemical cells 22
    2.4.1. Internal reflection cell configuration 23
    2.4.2. External reflection cell configuration 25
    2.4.3. Alternative cell configurations 27
    2.4.4. Results of studies using the introduced cell configurations 28
  2.5. Infrared absorption bands in the CO_2 reduction reaction on silver 30
3. Limitations of the current and requirements for the new spectroelectrochemical cell 35
  3.1. Limitations of the current spectroelectrochemical cell 35
  3.2. Requirements for the new spectroelectrochemical cell 36
4. Design of the new In-Situ IR spectroelectrochemical cell 39

5. Experimental 41
  5.1. Setup 41
    5.1.1. ATR cell 41
    5.1.2. Thin layer flow cell..42
  5.2. Electrode preparation...43
    5.2.1. ATR cell 44
    5.2.2. Thin layer flow cell..44
  5.3. Experiments...45
    5.3.1. ATR cell 45
    5.3.2. Thin layer flow cell..47
6. Results and discussion..51
  6.1. ATR cell configuration..51
    6.1.1. Reference IR absorption spectra 51
    6.1.2. CO_2 reduction reaction 57
    6.1.3. Summary...70
  6.2. Thin layer flow cell configuration 71
    6.2.1. Calibration of the pump 72
    6.2.2. Electrochemistry..72
    6.2.3. Set angle ATR accessory..74
    6.2.4. Reference FTIR absorption spectra...76
    6.2.5. CO_2 reduction reaction..77
    6.2.6. Summary...84
  6.3. Comparison ATR and thin layer flow cell configuration.......................................85
    6.3.1. Bulk crystallinity of the silver working electrodes 86
    6.3.2. Surface structure of the silver working electrodes 88
    6.3.3. Current density vs time characteristics 89
    6.3.4. IR absorption spectra 90
    6.3.5. Summary...94
7. Conclusion 97
8. Recommendations 99
Bibliography 101

Appendix 105
  I. FTIR absorption spectra measured in the ATR cell 105
    0.1 M KCl 105
    0.1 M $KHCO_3$ 106
    0.1 M K_2HPO_4 107
    0.1 M $KClO_4$ 108
  II. FTIR absorption spectra measured in the thin layer flow cell 109
    0.1 M KCl 109
    0.1 M $KHCO_3$ 110

1. Introduction

Today's energy supply is still mainly based on fossil fuels. The consumption of fossil fuels leads to the emission of carbon dioxide (CO_2) which is one of the main greenhouse gases in the atmosphere. The amount of CO_2 in the atmosphere is increasing and causing undesirable climate change. Therefore, the mitigation of CO_2 is of big importance in order to reduce the climate change. That is why more and more energy is produced in a renewable way. Currently, renewable energy is mainly produced by solar and wind energy and comes in the form of electricity. In contrast to the fossil fuel-based energy supply, the renewable energy supply shows fluctuations in short term, day and night, and long term, seasonal (summer and winter) energy production. In order to overcome these fluctuations, the excess produced electricity during the day and in summer has to be stored in an efficient reversible way so that the energy can be released again when it is needed at night or when more energy is needed in winter.

One possible solution that tackles both problems is the electrochemical reduction of CO_2 in aqueous electrolytes into highly valuable chemicals, or so called solar fuels, as for example syngas or methanol using excess renewable electricity. The problem of the electrochemical reduction of CO_2 is however that it can produce a large variety of products. In order to control the process to selectively produce the desired product it is necessary to understand the exact reaction mechanism of the CO_2 conversion. This can be studied using attenuated total reflexion infrared (ATR-IR) spectroscopy to probe the surface of the electrocatalyst during the reaction by connecting an ATR-IR accessory directly to the electrochemical cell.

In a typical ATR-IR cell configuration, the electro catalyst is deposited directly on the ATR-crystal which restricts the type of material and the deposition methods that can be used for the catalyst resulting in limited surface characteristics. Moreover, it reduces the lifetime of the ATR-crystal significantly.

The aim for this project is therefore to develop a new infrared (IR) spectroelectrochemical cell that allows an easy access for the electrocatalytic sample to be exchanged, while maintaining a high signal from the ATR source. To achieve this goal the following questions, have to be answered. First of all:

- *What types of vibrational spectroscopy exist, how do they work and why is it surface specific?*

For the development of a new spectroelectrochemical cell it is necessary to obtain an overview of the available possibilities. So:

- *What types of spectroelectrochemical cells are used in studies to determine the reaction mechanism in an electrochemical reaction?*
- *What are the advantages and disadvantages of these cells?*

Since this study focuses on the CO_2 reduction on a silver electrode, it is important to know at which wavenumbers the IR absorption and desorption bands of the reaction intermediates and products of the CO_2 reduction reaction occur. Thus:

- *At which wavenumbers do reaction intermediates and products of the electrochemical reduction of* CO_2 *on silver absorb IR radiation?*

The above mentioned are answered in chapter 2. In this chapter, a literature study performed on:

- The general method and mechanisms of electrochemical reduction of CO_2.
- The effect of the used electrocatalyst on the selectivity of the reaction products and on how to improve the catalytic activity.
- The working principle and surface enhancement of vibrational spectroscopy.
- Developments of spectroelectrochemical cells and obtained results.
- IR absorption bands present in the CO2 reduction reaction.

Based on the obtained answers from the literature study and the knowledge and experimental experience from previous research with the ATR cell, the two following questions came up:

- *What are the limitations of the current used ATR spectroelectrochemical cell?* And
- *What are the requirements for the new spectroelectrochemical cell?*

These questions are answered in chapter 3. Based on the obtained results from the literature study and experience from the current ATR spectroelectrochemical cell a new concept spectroelectrochemical cell for the electrochemical reduction of CO_2 will be designed and fabricated. The new design of the IR spectroelectrochemical cell is introduced and described in chapter 4. The performance of the new IR spectroelectrochemical cell will be tested experimentally and compared to the results obtained with the ATR cell. The experimental set up and the performed experiments are described in chapter 5. The aim of the experiments is to answer the main research question:

- ***Does information obtained from the new spectroelectrochemical cell give new insights on the electrochemical reduction mechanism of*** CO_2 ***on a silver electrode?***

About the experiments:

- The desired silver catalyst will be fabricated by magnetron sputtering and the crystal and surface structure will be characterized by XRD and AFM respectively.
- The silver electrocatalyst will be placed as the working electrode in the spectroelectrochemical cell.
- IR spectrometry is used to determine the chemical molecules on the electrode surface to gain information on the reaction mechanism.
- Experimental results are compared to results from literature.

In chapter 6, the results of the performed experiments are presented and discussed, and the main research question is answered. Subsequently, the obtained results in this study are summarized and conclusions are drawn in chapter 7. Finally, chapter 8, completes this thesis with recommendations for further research. The expected result of this master project is that from the, in the new designed spectroelectrochemical cell which consist of an easily exchangeable working electrode, measured IR spectra new insights on the reaction mechanism of the electrochemical reduction of CO_2 on electrocatalytic surfaces can be acquired.

2. Literature review

In this chapter, an overview of the literature on the electrochemical reduction of CO_2, vibrational spectroscopy and In-Situ spectroelectrochemical studies is given. First, several methods to reduce the atmospheric concentration of CO_2 are introduced in section 2.1. Since this thesis deals with the electrochemical reduction of CO_2 a more in-depth review of this method is given in section 2.2. For the design of a new In-Situ spectroelectrochemical cell it is first necessary to understand how vibrational spectroscopy works. That is why in section 2.3 the working principle of the two most common vibrational techniques, IR and Raman spectroscopy, is described. In order to develop a new In-Situ spectroelectrochemical cell, possible cell configurations obtained from literature research on In-Situ spectroscopic studies are introduced in section 2.4. In order to determine possible reaction intermediates and products of the CO_2 reduction reaction with IR spectroscopy one needs to know at which wavenumbers these intermediates and products absorb IR radiation. Therefore, this chapter concludes with the assignments of IR absorption bands in section 2.5. These assignments are based on spectroscopic studies of the CO_2 reduction reaction and other reactions of small organic molecules as, their reaction intermediates and products correspond to the reaction intermediates and products present at the CO_2 reduction reaction.

2.1. Reduction of atmospheric carbon dioxide

As already introduced before, the increasing amount of CO_2 in the atmosphere is one of the main reasons for the ongoing climate change. In order to mitigate the negative impacts of the climate change the amount of CO_2 in the atmosphere has to be reduced. Large scale CO_2 emitters, especially fossil fuelled power plants, already have to capture their CO_2 since environmental regulations inhibit them to emit it into the atmosphere. The problem is now what to do with the captured CO_2? Over the past decades two main techniques emerged. Geological CO_2 sequestration and molecular conversion [1].

Extracted gas and oil fields are widely present all over the world and can be filled by feeding in the captured CO_2. Since this technique has not been in operation for very long, the long-term impacts of geological CO_2 sequestration are uncertain due to the potential of leaking. Furthermore, in a renewable and sustainable future fossil fuels are not used anymore. However, in such a future there will be still a need for a carbon source. CO_2 could be a possible option for a carbon source when applying a CO_2 neutral cycle.

In comparison to sequestration, molecular conversion is a more attractive process since it allows the valorisation of CO_2 as a feedstock to produce useful chemicals such as syngas and methanol [1]. Therefore, the conversion of CO_2 has been studied intensively in the last couple of years using thermochemical, electrochemical, and photochemical methods [2].

The thermochemical conversion of CO_2 proceeds via a reforming process. It requires high reaction temperatures and pressures and an equivalent amount of hydrogen as the reducing agent. Currently hydrogen is mainly produced by methane steam reforming which is not sustainable, but hydrogen can also be produced using renewable energy via electrolysis of water. However, the compression of hydrogen to high pressures and the high operating temperatures of the reforming process cost an enormous amount of energy making this conversion method unfavourable.

Only a few studies of photochemical processes have been reported to be photo catalytically active for the reduction CO_2 [2]. The selectivity and/or production rate of these systems however are far too low to be economically valid.

The electrochemical method for the reduction of CO_2 has numerous advantages over the other above-mentioned conversion processes. It is directly controllable by the adjustment of the applied electrode potential, can have a relatively small footprint, operate near room temperature, requires only a minimal chemical intake, and can be easily scaled-up to suit the application [1], making the electrochemical reduction of CO_2 the most promising method among the molecular conversion methods.

2.2. Electrochemical reduction of CO_2

As described in the previous section, the electrochemical reduction of CO_2 has numerous advantages over the other introduced mechanism to reduce the atmospheric CO_2. Despite these advantages the electrochemical reduction of CO_2 however also raises some problems that have to be overcome.

2.2.1. Required electric potential

Since CO_2 is the final, fully oxidized carbon product of the combustion of organic molecules, it is thermodynamically a very stable molecule and therefore, it has a high initial activation energy for the reduction process. This results in low reaction kinetics [1]. In particular, the single electron reduction of CO_2 to CO_2^- has a very high thermodynamic potential, of $E° = -1.90$ V versus the standard hydrogen electrode (SHE) in aqueous media (pH = 7), making the reaction highly energetic and unfavourable [2]. This high thermodynamic potential can be reduced using multiple proton-coupled electron-transfer steps which occur at lower potentials [1-3]. This results in a wide variety in reaction products which makes the selective production of desired chemicals very challenging. This is because of the similarity of redox potentials for all the reaction pathways. The potentials (E^0) of the possible half reactions with respect to the reversible hydrogen electrode (RHE) and number of protons and electrons associated with several common CO_2 reduction reaction products are presented in Table 1 [3].

Table 1: Potentials for the corresponding CO_2 reduction and oxygen evolution half reactions at the cathode and anode respectively [3]

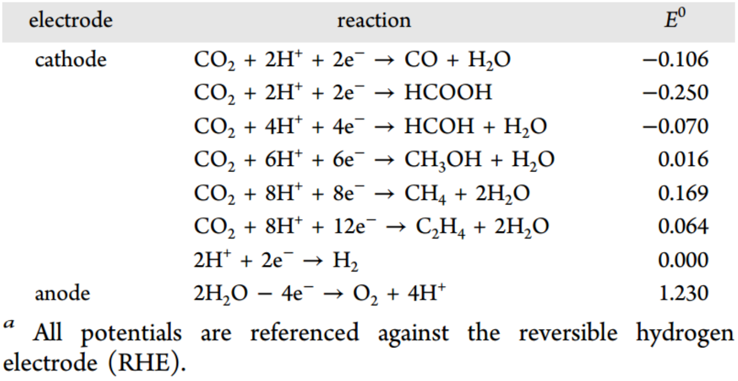

electrode	reaction	E^0
cathode	$CO_2 + 2H^+ + 2e^- \rightarrow CO + H_2O$	−0.106
	$CO_2 + 2H^+ + 2e^- \rightarrow HCOOH$	−0.250
	$CO_2 + 4H^+ + 4e^- \rightarrow HCOH + H_2O$	−0.070
	$CO_2 + 6H^+ + 6e^- \rightarrow CH_3OH + H_2O$	0.016
	$CO_2 + 8H^+ + 8e^- \rightarrow CH_4 + 2H_2O$	0.169
	$CO_2 + 8H^+ + 12e^- \rightarrow C_2H_4 + 2H_2O$	0.064
	$2H^+ + 2e^- \rightarrow H_2$	0.000
anode	$2H_2O - 4e^- \rightarrow O_2 + 4H^+$	1.230

[a] All potentials are referenced against the reversible hydrogen electrode (RHE).

The theoretical cell voltage required for the electrochemical CO_2 reduction is defined by Equation 1 and can be calculated easily for the desired reaction from Table 1.

$$E_{cell} = E_{anode} - E_{cathode} \qquad (1)$$

In practice however, cell voltages often exceed these theoretical voltages because the CO_2 reduction catalysts require overpotentials of several hundred millivolts to achieve satisfactory reaction rates. The overpotential represents energy which is not used in the reaction, waste energy, that can lead to inefficiencies including broad product distributions at the cathode as can be seen from Table 1, and reduced Faradaic efficiencies.

2.2.2. Hydrogen evolution reaction

In addition to the CO_2 reduction reaction a second reaction, the hydrogen evolution reaction (HER), as can be seen in Table 1, takes place at the cathode. These reactions are in competition with each other and an introduced overpotential for the CO_2 reduction reaction can increase the HER, as can be seen from the Pourbaix diagram for CO_2 in water which is presented in Figure 1 [4]. The HER becomes even more dominant when an aqueous based electrolyte is used in the CO_2 reduction reaction. The HER introduces a major challenge for efficient and selective CO_2 electrochemical reduction and therefore, electrocatalysts for CO_2 reduction play an important role because they should minimize the activation barrier for the CO_2 reduction reaction with respect to the HER, driving CO_2 reduction selectively at low over potential with high reaction rates [1]. The role of the electrocatalyst will be discussed in more detail in the is section 2.2.5.

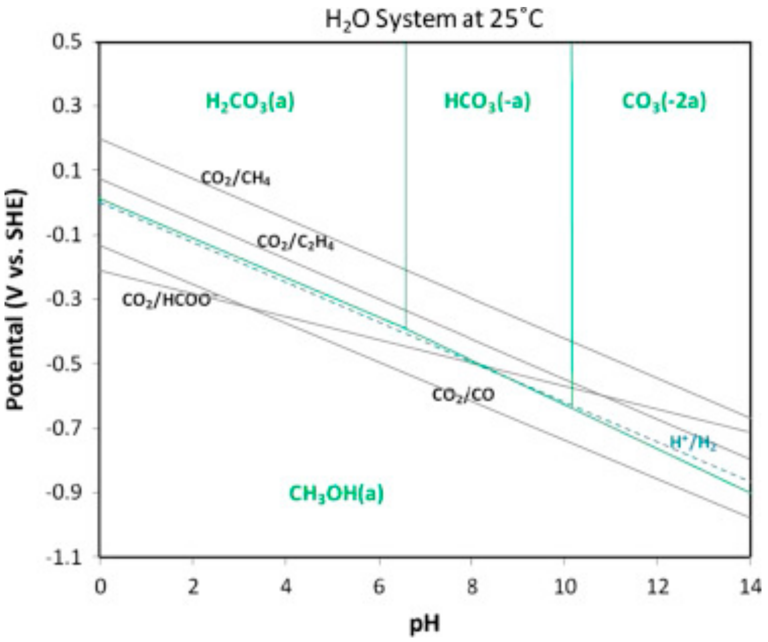

Figure 1: Pourbaix diagram for the carbon dioxide reduction reaction at 25 °C [4]

From the Pourbaix diagram, presented in Figure 1, it can also be observed that the pH of the system is of great importance in the electrochemical reduction of CO_2. It clearly influences the equilibrium activity of the CO_2 reduction and HER. Since, in aqueous conditions, the CO_2 reduction is strongly influenced by the activity of H^+ ions in solution [4].

2.2.3. Electrolytes for the CO_2 reduction reaction

The electrochemical reduction of CO_2 generally uses aqueous electrolytes based on sodium and potassium alkali cations and halide, bicarbonate or hydroxide anions with water as solvent. These inorganic salts are often used due to their high conductivities in water. Additionally, the water in aqueous electrolytes provides protons for the necessary electrochemical proton transfer steps involved in the reaction pathway [5]. Adding CO_2 to the aqueous electrolyte results in an increase in acidity thus a lower pH and an increase in HER. Increasing the pH increases the over potential for the HER but also drives the conversion of CO_2 to HCO_3^- and CO_3^{2-} which are undesirable products in the electrolyte as they lower the activity of the CO_2 reduction [6]. Noticeable is also that both the CO_2 reduction reaction and the HER generate OH^- ions at the catalyst–solution interface, the cathode, influencing the local pH and thus CO_2 concentration. Besides, intermediates of the CO_2 reduction such as CO find a local pH at the electrode that differs from the bulk pH, which may have significant consequences on the selectivity of the reaction [6].

The use of buffer electrolyte solutions can mitigate the conversion of CO_2 into HCO_3^- by neutralizing the OH^- produced at the cathode [4]. In addition, the choice of the solvent, pH, and the presence of certain cations or anions can stabilize reaction intermediates or inhibit their formation and are speculated to aid directly in the choice of certain reaction pathways [6]. That is why most studies use buffer electrolytes like bicarbonate buffers or phosphate buffers to counteract the overall changes in pH. Despite the use of the buffer electrolyte solution, there still might be a significant pH difference with respect to the bulk electrolyte. The local pH at the electrode is determined by the bulk pH of the electrolyte, its buffer strength, as well as the local current density flowing which is in turn dependent on the local surface roughness [6].

The influence of certain anions and cations has also been investigated. The hypothesis is raised that cations play a role in electrochemical reduction of CO_2 either by specifically adsorbing on the electrode and thereby influencing the potential at the outer Helmholtz plane, or by delivering water molecules from their solvation shell to the electrode, which influences the hydrogen coverage on the electrode [6]. Moreover, different cations may have different interactions with negatively charged intermediates of the reaction. Murata and Hori [7] investigated already in 1991 the effect of different cations and found that CO_2 reduction was favourable in Na^+, K^+, and Cs^+ solutions because of the suppressing of the HER.

In most studies, aqueous electrolytes are used in the electrocatalytic reduction of CO_2. CO_2 however, dissolves only poorly in water, 0.034 M [6], leading to low concentrations of CO_2 in a saturated aqueous electrolyte and as already mentioned before, the HER is a competitive reaction in aqueous media and is the major reason of the reduced faradaic efficiency for CO_2 reduction. To challenge this problem, solvents with increased solubility of CO_2 and lower proton concentration can be used. In aprotic solvents, like dimethyl sulfoxide, N,N-dimethyl formamide, or acetonitrile, the major product produced on metal electrodes like Pb, In, Sn, and Hg is oxalic acid/oxalate, whereas CO and carbonate are the major products on Pt, Pd, Au, and Zn electrodes [6]. Combining aqueous with non-aqueous solvents results in a broader reduction product spectrum. In these mixtures the proton availability can be controlled by adjusting the amount of water in an organic electrolyte. This is thus an effective way to control the faradaic efficiency and selectivity for CO_2 reduction [6]. More recently, ionic liquids like EMIMBF3Cl gained significant attention as electrolytes for the reduction of CO_2

because it is able to bind CO_2 via a Lewis base adduct and is active in the reduction of CO_2 [6].

2.2.4. Sustainable and economic viable CO_2 reduction products

As described above, the proton assisted electrochemical reduction of CO_2 can produce a large variety on reaction products. An important question that has to be answered, is to which reduction product the reaction should be steered. Kauffman et al. [3] calculated the electrical input in MWh needed to convert one metric tonne of CO_2 into several products (left axis) based on results of literature studies (red circles) and ideal cases (grey squares) and compared it to the CO_2 emission in tonnes from fossil fuel derived electricity that is needed to produce the products (right axis). The results are presented in Figure 2. As can be seen directly, the reduction of CO_2 using fossil fuel derived electricity results in a non-carbon neutral cycle. Only in the ideal case of the reduction to CO or HCOOH a carbon neutral cycle can be achieved. This result shows that a carbon neutral cycle can only be fulfilled when using renewable carbon free energy. Moreover, it shows that there is a big difference in energy consumption for the production of the different reduction products.

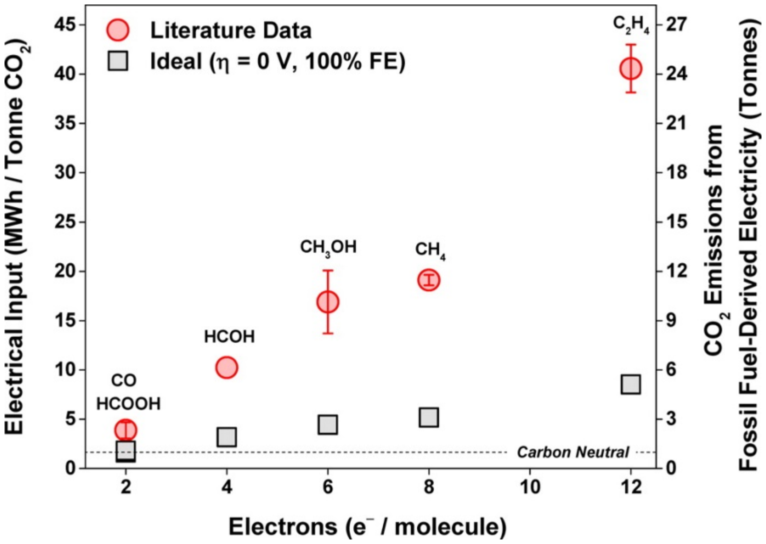

Figure 2: Electrical input needed for the conversion of CO_2 into several products with corresponding CO_2 emissions for the needed electricity [3]

In contrast, Qi and Feng [2] argued that it depends on economics and constructed the following table, Table 2, of the major CO_2 reduction products with their market prices and estimated production cost based on the electricity price. From Table 2 it can be seen that the following reduction products, carbon monoxide, formic acid, formaldehyde and propanol are economical profitable because of the high market price. The market prices of these reduction products however take only the price of the reduction product itself into account and neglect capital cost for the equipment and catalysts, required energy for the separation of the products and the cost of CO_2.

Formic acid, formaldehyde and propanol are liquids and it is very energy intensive to separate these liquid reduction products from the aqueous electrolyte that increases the production costs and could result in an economical unfavourable process [2].

In comparison to the profitable liquid reduction products, carbon monoxide is a gas and can be easily separated from the aqueous electrolyte. Catalysts for the electrochemical reduction of CO_2 have already been researched since the early 1980s [1]. Research showed that noble metals are able to produce CO as major product [2]. A more detailed view and developments on available catalyst will be given in the next section. Furthermore, carbon monoxide is a highly valuable chemical product which is frequently used in current chemical industry [1]. Besides, it is the main building component for synthetic liquid fuels in the well-developed Fischer-Tropfsch process. So despite the high cost of noble metals, that are used as catalysts in the electrochemical reduction of CO_2, the high market price of carbon monoxide and low energy consumption during the reduction reaction, still makes the process economically favourable, making carbon monoxide currently the most promising reduction product [1].

Table 2: Estimated costs for major CO_2 reduction products assuming electricity at a price of \$0.07 per kWh, a cell potential of 2 V (with minimum overpotentials) [2]

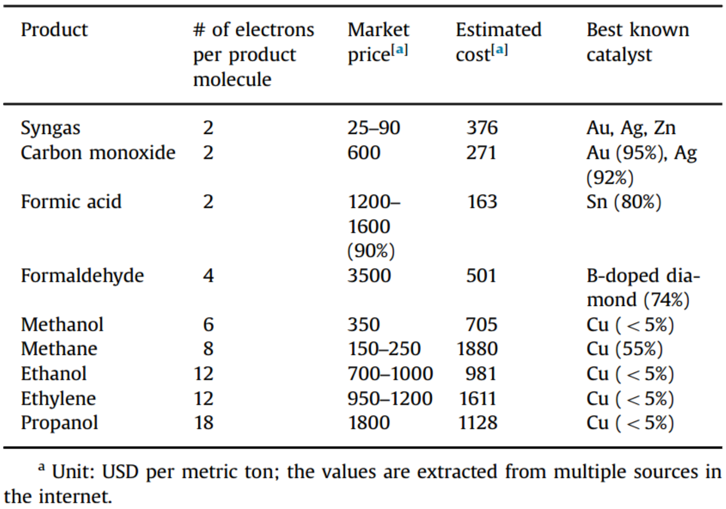

Product	# of electrons per product molecule	Market price[a]	Estimated cost[a]	Best known catalyst
Syngas	2	25–90	376	Au, Ag, Zn
Carbon monoxide	2	600	271	Au (95%), Ag (92%)
Formic acid	2	1200–1600 (90%)	163	Sn (80%)
Formaldehyde	4	3500	501	B-doped diamond (74%)
Methanol	6	350	705	Cu (< 5%)
Methane	8	150–250	1880	Cu (55%)
Ethanol	12	700–1000	981	Cu (< 5%)
Ethylene	12	950–1200	1611	Cu (< 5%)
Propanol	18	1800	1128	Cu (< 5%)

[a] Unit: USD per metric ton; the values are extracted from multiple sources in the internet.

2.2.5. The effect of the used electrocatalyst on the CO_2 reduction products

Electrocatalysts play an important role in the electrochemical reduction of CO_2. Their task is to bind and activate the CO_2 molecule to reduce the high activation energy and resulting overpotential. Furthermore, electrocatalysts can selectively steer the formation of the desired end products [5]. Electrocatalysts for the electrochemical reduction of CO_2 are studied since the early 1980s and research was focused on the catalytic bulk activity of metals in the form of polycrystalline monometallic metals [1, 2]. Nowadays, existing electrocatalysts can be divided into three main groups: Metallic catalysts, Non-metallic catalysts and Molecular catalysts [2]. An overview of available catalysts in these groups is presented in Figure 3 [2].

As described is section 2.2.1, the electrochemical reduction of CO_2 results in a variety of reaction products. Based on the major reduction product, the investigated metal catalysts can be divided into four sub groups which are also indicated in Figure 3. For metals as Sn, In and Pb formic acid is the major reduction product. Copper shows selectivity for hydrocarbons as major reduction product. The reduction product of interest, as augmented in the previous section, 2.2.4, is however CO.

CO is produced as main reduction product at Au, Ag, Zn, Fe, Ni and Pt monometallic electrocatalysts. For the latter three however, the HER rate is way higher than the CO_2 reduction rate [1] because of the low current efficiency making them unfavourable for the CO_2 to CO reduction reaction. Advantages of polycrystalline monometallic electrocatalysts are that they are structurally simple, easy to handle, and robust [2]. Hori et al. [8] studied the catalytic activity of several noble metals and concluded that Au showed the highest catalytic activity in the electrochemical reduction of CO_2. Over the last few years electrocatalysts beyond bulk monometallics have been investigated. Nanostructured monometallics, ion-modified metallics, bimetallics and non-metallic materials show promising results for CO2 reduction [1].

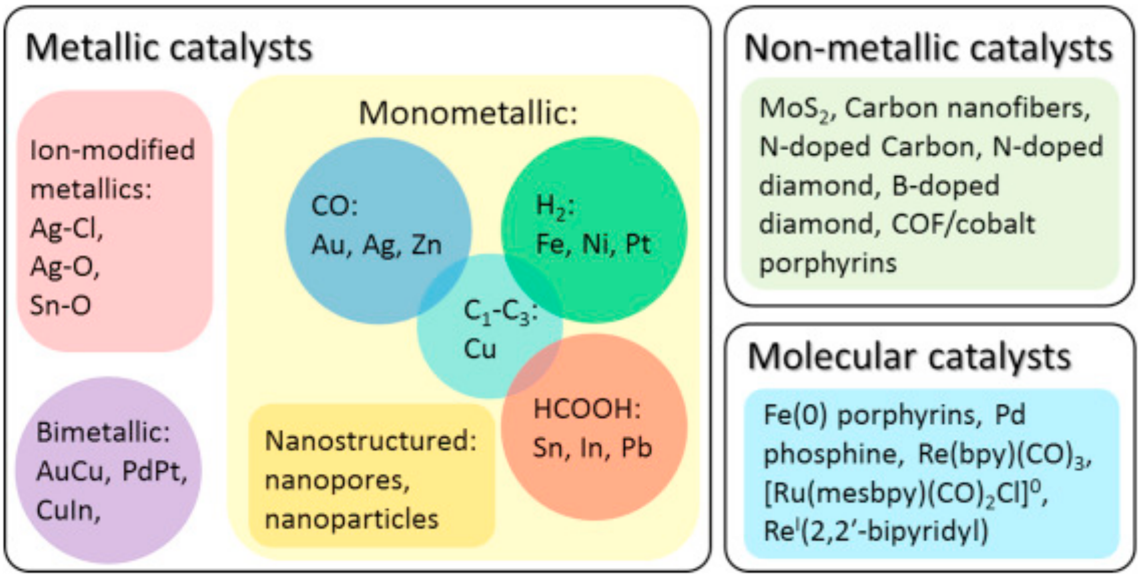

Figure 3: Overview of the studied electrocatalysts for the CO_2 reduction reaction [2]

2.2.6. Electrochemical reduction of CO_2 on a silver electrode

As introduced in the previous section, 2.2.5, gold has the highest catalytic activity in the electrochemical reduction of CO_2 to CO. Since gold is an expensive material it is economical unfavourable to use as an electrocatalyst. Silver which is less expensive has also a high catalytic activity toward CO production [8] and is therefore more suitable. Today, research is performed on bulk silver catalysts to study the exact reaction mechanism and kinetics. However, this will not improve reaction rates and activities [1]. Therefore, on the other hand, research also focuses on investigating new types of catalytic active sites or structures to enhance the efficiency of the electrochemical CO_2 reduction process [1].

Hatsukade et al. [9] investigated the potential dependent activity and selectivity of the electrochemical reduction of CO_2 on metallic silver surfaces under ambient conditions. Based on the results of their study, they gained insight in the reaction mechanism of the reduction of CO_2 on a silver electrocatalyst and observed the production of six major reduction products. The schematic representation of the obtained reaction mechanism is presented in Figure 4 [9].

Key in developing active, selective and stable electrocatalysts is to understand the surface mediated reaction mechanism. A powerful tool to study the surfaces of the electrocatalysts during the reaction is IR spectroscopy which is described in the next section.

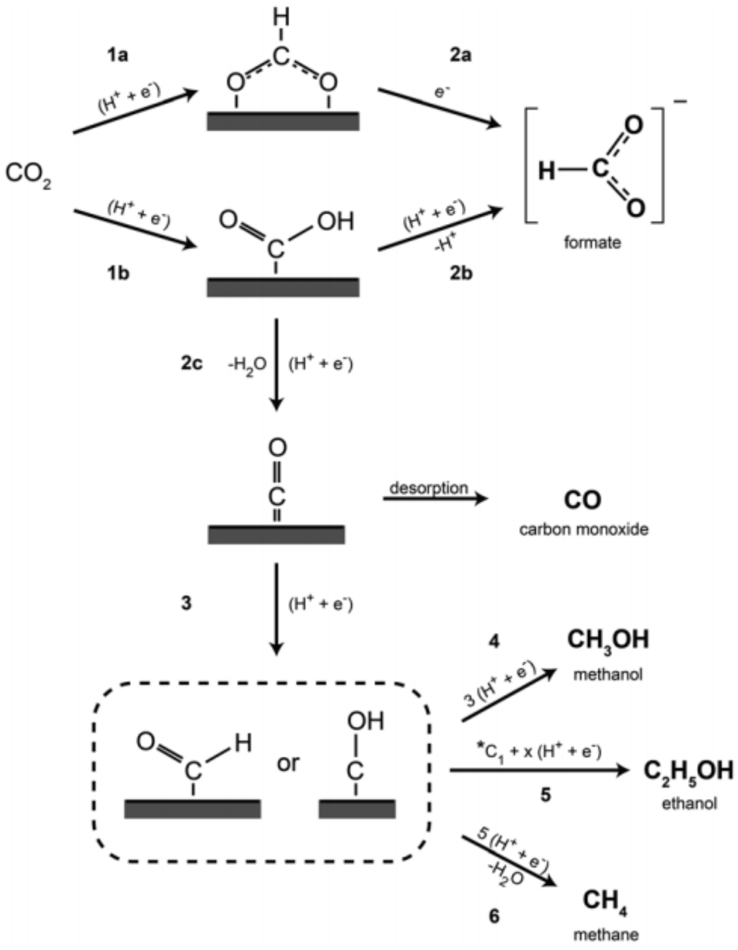

Figure 4: Possible CO_2 reduction pathways on a silver electrocatalyst [9]

2.3. Vibrational spectroscopy

Spectroscopy is the study of the interaction of matter and electromagnetic radiation. Since electromagnetic radiation has wave like properties it can be characterized as a wave by its frequency or wavelength. The frequency of a wave is defined as the number or wave crests that pass a defined point in one second and has the unit Hertz (Hz). The wavelength is defined as the distance of any point on the wave to the corresponding point on the next wave and is measured in nanometres (nm) which corresponds to 10^{-9} meters.

2.3.1. Theory

Vibrational spectroscopy is based on a physical mechanism that is able to excite molecular vibrations. There are two different options: Infrared absorption and Raman scattering. The former is the absorption of light quanta by molecules when irradiated with polychromatic light that include photons with the same amount of energy as the difference between the initial and final vibrational state of the molecule. Since the energy difference between the states is only small, below 0.5 eV, infrared radiation is sufficient enough to introduce vibrational transitions. The latter results from the inelastic scattering of electromagnetic radiation by matter. In contrast to IR absorption spectroscopy, monochromatic irradiation is needed to excite molecular vibrations from scattering.

2.3.2. Infrared spectroscopy

Bonds in molecules behave like vibrating springs and vibrate in stretching and bending motions. A stretch motion is the vibration in the line of the bond that changes the bond length. In contrast, the bending motion occurs not along the line of the bond since it changes the bond angles. Diatomic molecules only show stretching vibrations since there is no angle between the two atoms. Molecules with three or more atoms are more complex. They can have symmetric and antisymmetric stretching and bending vibrations. Furthermore, the bending vibrations can be either in or out of plane. A summary of the present vibrations in molecules is presented in Figure 5 [10].

Each of the presented vibrations of a bond between two atoms in a molecule occurs at a characteristic frequency. In IR absorption spectroscopy, the frequency of the electromagnetic radiation is given as the wavenumber. This is defined as the number of waves that are present in one centimetre and therefore has the unit of reciprocal centimetres (cm^{-1}). When a molecule is irradiated with IR radiation that exactly matches the frequency of the vibration of the bond between two atoms, it can absorb the energy of the IR radiation causing the vibration to be stronger.

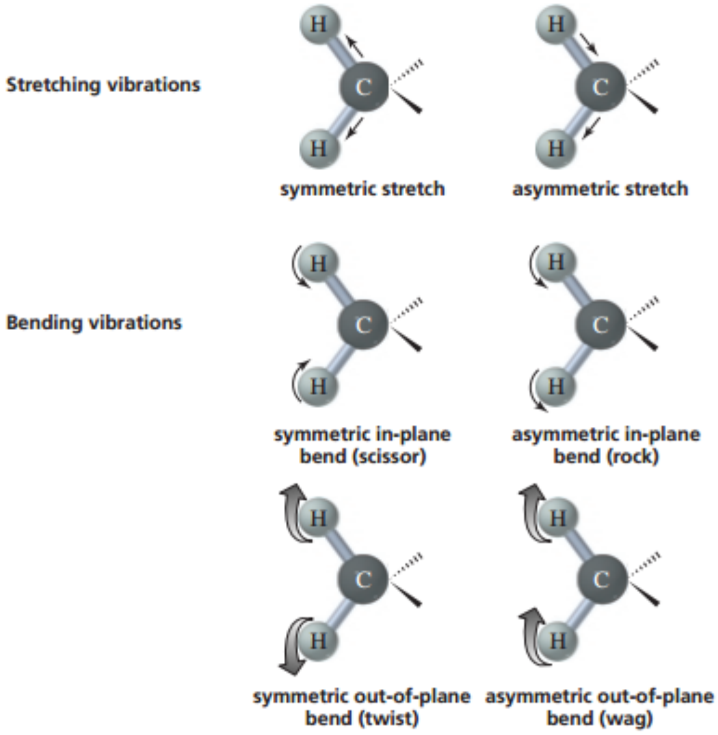

Figure 5: Stretching and bending vibrations in molecules with three or more atoms [10]

An IR spectrum is obtained by scanning the sample with IR radiation and plot the percent of transmission or absorption against the wavenumber. At frequencies where no IR radiation is absorbed, all the IR radiation is transmitted through the sample resulting in 100% transmission. At frequencies where IR radiation is absorbed by the sample this results in a lower percentage of transmission creating spikes in the spectrum. These spikes are called absorption bands and represent a specific bond in the molecule. The obtained spectra can be divided into two regions. The functional group region, from 4000-1400 cm^{-1} and the fingerprint area from 1400-600 cm^{-1}. So, when two different molecules have the same functional groups they can still be differentiated because of the difference in the fingerprint region [10].

It costs more energy to stretch a bond than to bend it. Therefore, absorption bands of stretching vibrations are found in the functional group region, whereas bending vibration bands are situated in the fingerprint region. The intensity of the absorption band depends on the size of the change in dipole moment. The change in dipole moment is caused by the increase in distance between two atoms in a molecule due to the stretching vibration. The greater the change in dipole moment, the more intense the IR absorption. Next to this, the polarity of the bond itself determines the intensity of the absorption band. The more polar the bond, the more intense the absorption. The intensity of the band is furthermore dependent on the number of identical bonds in the molecule and the concentration of the molecule in the sample itself since more molecules result in more IR absorption. Not all the bonds vibrations in molecules are visible with IR spectroscopy. As already mentioned, there has to be a change in dipole moment in the bond to absorb IR radiation. Symmetrical molecules have no dipole moments. Stretching vibrations increase the distance between the atoms indeed but due to symmetry no dipole moment is created and therefore no change in dipole moment is present. Such a vibrational mode is then said to be IR inactive [10].

2.3.3. Raman spectroscopy

Raman spectroscopy uses the change in polarizability property of the molecule with respect to its vibrational motion. When the monochromatic light hits the molecule, it is scattered. The scattered light consists of two different types of scattered light namely, Rayleigh and Raman scattered light [11, 12]. Rayleigh scattering corresponds to scattered light with the same frequency as the incident light, also called elastic scattering, whereas in Raman scattering the scattered light has a different frequency than the incident light, inelastic scattering, and therefore a different energy. Due to the law of the conversation of energy, the difference in energy corresponds to energy change of the molecule, that is the transition between the vibrational states and is the vibrational energy that is gained or lost in the molecule. This inelastic scattering of photons was first discovered by the Indian scientist Raman in 1928. For this reason, this vibrational spectroscopy method is called Raman scattering.

The energy level diagram in Figure 6 [11] illustrates this process. The interaction of the incident photon with the molecule excites the molecule from the zero-vibrational level of the ground electronic state. The excited molecule then relaxes again but can do that in two different ways. The molecule can return to its original energy level (case I in Figure 6) corresponding to Rayleigh (elastic) scattering or to a different energy level (case II in Figure 6) corresponding to Raman (inelastic) scattering. Rayleigh scattering is the most common occurring form of scattering. In one out of million cases however, molecules release energy that is different to the absorbed energy resulting in Raman scattering. The inelastic scattering can be divided into two cases. Usually a molecule releases less energy than absorbed ending up in a higher energy level (case II in Figure 6) which is reflected in a lower wavenumber. This kind of Raman scattering is called Stokes scattering. On the contrary, in some cases the molecule releases more energy than absorbed resulting that the molecule ends up in a lower energy level (case III in Figure 6) corresponding to a higher wavenumber. This type of Raman scattering is called Anti-Stokes scattering. A Raman spectrum is a plot of the intensity against the wavenumber of the radiation [11, 12].

From the energy level diagram, it can also be seen that in both, IR absorption and Raman scattering, the molecule is excited from the ground to an excited state but that in IR absorption this excitation occurs in one step while in Raman scattering two steps are required, excitation and relaxation. As described above, both IR absorption and Raman scattering spectroscopy can provide information about the transition between different vibrational states. However, not all these transitions are active in IR absorption or Raman scattering. The main difference between IR absorption and Raman scattering spectroscopy is, that vibrations that change the dipole moment in a bond between atoms of a molecule are active in IR absorption while vibrations that change the polarizability of a bond in a molecule are active in Raman scattering. So, depending on the molecule, IR absorption and Raman scattering spectroscopy can probe the same or different vibrational transitions. For this reason, using both spectroscopic techniques can support the finding on one technique or even complement it with new information. To make comparison easy, both spectra usually plotted in an analogous way. The y-axis represents the extend of the absorbed IR light in absorbance or the Raman intensities of the scattered light measured in counts per second. For both spectra, the energy of the vibrational transition, corresponding to the frequency of absorbed light and frequency difference between exciting and scattered light, is expressed in wavenumbers and is presented on the x-axis [12].

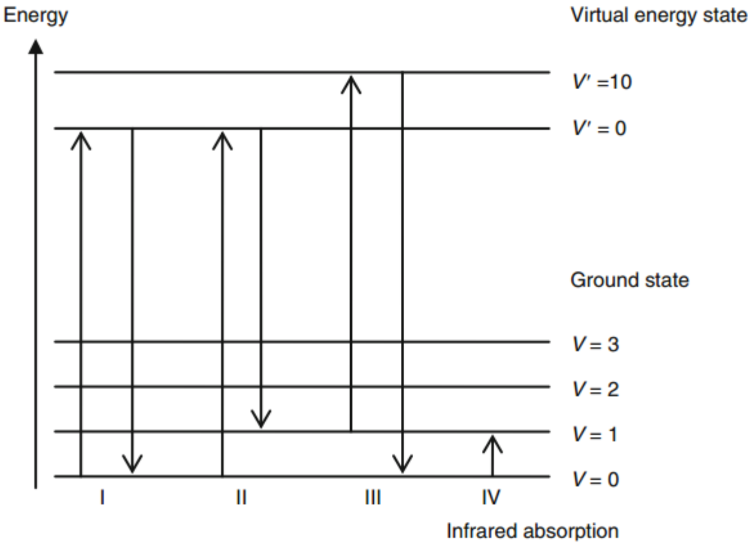

Figure 6: Energy level diagram of I Rayleigh, II Stokes and III Anti-Stokes scattering. IV shows IR absorption [11]

2.3.4. Surface enhanced vibrational spectroscopy

Molecules adsorbed on rough surfaces of certain materials may experience major enhancement of Raman scattering. This enhancement of vibrational bands at metal surfaces is not only restricted to Raman scattering but can also occur during IR absorption. However, in comparison to Raman scattering in a way smaller extent. The enhancement in both cases is metal- and wavelength-specific, such that for the typical spectral range of Raman and IR spectroscopy, wavelengths from 400 to 10000 nm, the metals that can contribute to the enhancement are silver (Ag) and gold (Au) [11, 13].

The surface enhanced Raman effect can be explained by the basis of classical electromagnetic theory. Light is scattered and absorbed by colloidal particles. When the size of the particle is small in comparison to the wavelength of the incident light, the electromagnetic field can effectively couple with the collective vibrations of the free electrons of the metal. These free electrons are called surface plasmons [13]. The incident electric field oscillates with the frequency of the incident light and induces an electric dipole moment in the particles. This induced dipole moment then results in the excitation of the surface plasmons. The excited surface plasmons are causing an additional electric field component normal to the surface in the near field of the sphere. A molecule which is located near the particle can then be excited by the electric field which consequently introduces all possible photo physical and photo chemical processes, including Raman scattering [13].

Enhanced absorption of IR radiation by molecules adsorbed on or in close vicinity to the Ag or Au metal surfaces is also based on the electromagnetic theory. The optically active Ag or Au metal surfaces can be produced by the electrodeless deposition of Ag or Au in vacuum on optically inert support windows. By using this deposition mode a thin metal film with a morphology of interconnected islands with sufficient roughness is created [13]. The incident IR radiation induces an oscillating dipole in the metal islands which leads to an increase in the electric field in the near-field, and consequently to an enhanced absorption by molecules that are located in close proximity to the film. Figure 7 shows the dipole alignment picture [13]. The dipoles can be aligned perpendicular or parallel to the metal surface which is represented in the left and right-hand side of Figure 7 respectively. As can be seen in the right-hand side of Figure 7, a dipole parallel to the metal surface is cancelled out, whereas a dipole perpendicular the metal surface adds up.

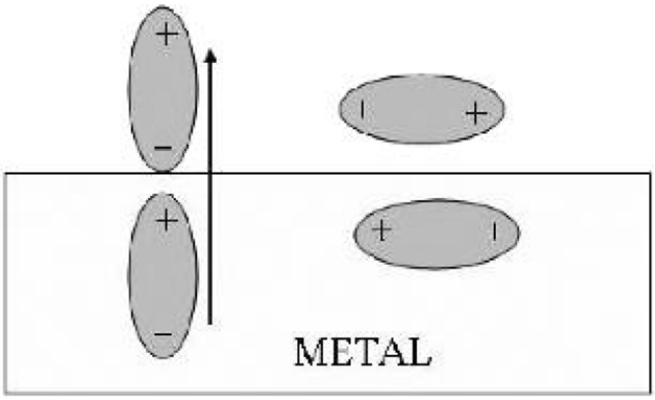

Figure 7: Schematic representation of perpendicular and parallel dipole alignment at the metal surface [13]

As only the electric field component perpendicular to the metal surface is enhanced, SEIRA signals are not detectable for vibrations associated with dipole moment changes parallel to the surface. Signals from s-polarized IR radiation correspond thus to molecules in the electrolyte solution and not to those adsorbed on the metal surface. Since one is only interested in surface adsorbed molecules, which can only be detected when their dipole moment is perpendicular to the metal surface the use of only p-polarized IR radiation ensures that only mainly surface bound molecules are detected as parallel dipoles cannot be detected. As already mentioned in the beginning of this section, the enhancement for SEIRA is distinctly smaller than for SERS as only the field of the incident radiation is enhanced but reaches enhancement factors between 10^2 and 10^3 [13].

2.4. In-Situ infrared spectroelectrochemical cells

Infrared spectroscopy is an important technique for the study of adsorption and catalysis at electrode–solution interfaces. The investigation of electrocatalytic reactions and processes at molecule level is of great importance in the successful development of an electrocatalyst that can steer the reaction in the desired direction. Based on its specific adsorption bands of molecules and surface selection rules, electrochemical In-Situ FTIR spectroscopy is a powerful tool to obtain real-time information about the chemical nature of adsorbates and the solution species involved in electrochemical reactions [14]. Among infrared methods, time-resolved FTIR spectroscopy is a powerful tool to monitor the dynamics of electrochemical processes. Two types of FTIR spectral acquisition modes, step-scan and rapid-scan, can be applied in electrochemical dynamic studies. The step-scan mode is distinct with its fast time-resolution that can achieve up to the nanosecond scale. The main disadvantage of the step-scan mode is that the approach is generally limited to the study of reversible reaction systems. Conversely, the rapid-scan mode can be used to study irreversible processes, although its time-resolution is relative slow (~ms) [15].

However, the main barrier in using infrared radiation to study adsorption and catalysis of electrochemical reactions in aqueous electrolytes is linked to the absorption by the electrolyte itself. Especially, when the studied reactants and products are in low concentrations at the surface of the electrocatalyst or in solution in the electrolyte with respect to the electrolyte concentration. In addition to this, the spectral interference of liquid water itself plays a significant role as the fundamental vibrations, as well as overtone and combination bands, of water set in from 1600 cm^{-1} in IR to 7400 cm^{-1} in near-IR region [16]. Besides, during the reflection at the electrode surface a part of the IR energy gets lost [14].

Two approaches have been developed in order to minimize the IR absorption by the electrolyte in In-Situ FTIR cells. They differ in the mode of IR reflection. One is based on internal reflection, so called Kretschmann or ATR cell, the other is based on external reflection, called thin layer cell [14]. The schematic presentations of the two approaches are presented in Figure 8. In both cases the working electrode (W.E.) is the used electro catalyst. Both configurations are described in detail in the following two sections.

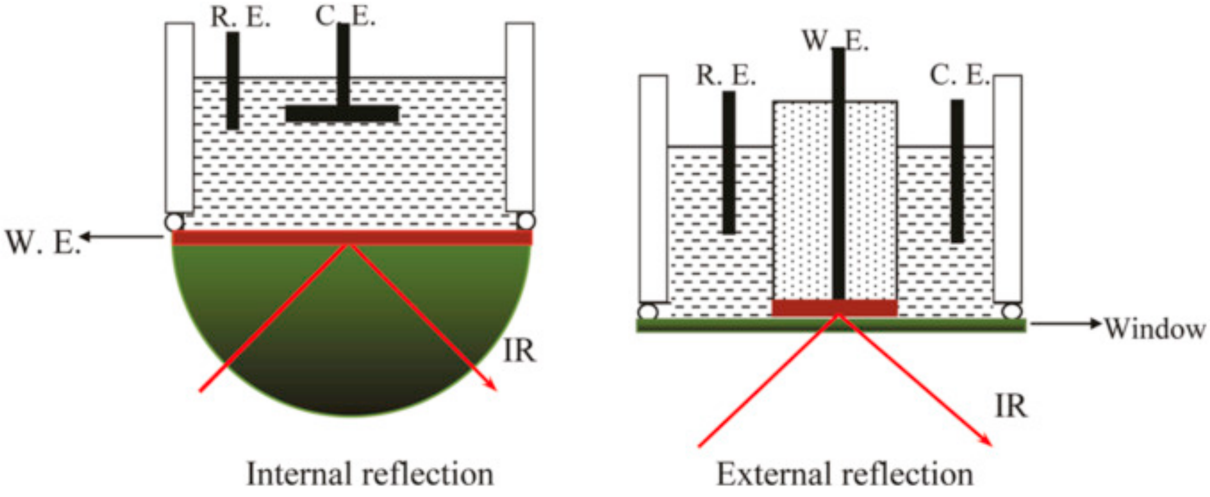

Figure 8: Schematic representation of the internal and external reflection cell configurations [14]

2.4.1. Internal reflection cell configuration

The internal reflection configuration uses attenuated total reflectance (ATR). In this configuration, the electrocatalyst with high refractive index, which acts as the working electrode, is directly deposited as a thin film on an IR transparent ATR crystal [14]. ATR takes advantage of the total internal reflection of light in the ATR crystal that may occur at a flat interface depending on the incidence angle of the IR beam and the difference in refractive index between two media, in this study the germanium ATR crystal and the deposited silver working electrode [17]. As can be seen in Figure 8, the IR beam is focused at back of the electrode and is reflected at the interface of the ATR crystal and deposited electrode. This reflection results in the generation of an evanescent wave that penetrates into the other side of the interface, into the electrode, to a depth of between 0.5 and 2 mm in the mid IR region [17]. Since the working electrode is only a thin layer, in the order of a few nm, the absorbed molecules at the front of the electrode, at the interface with the electrolyte, can be detected. In this configuration, the IR beam has not to pass the aqueous electrolyte resulting that no IR radiation is absorbed by the electrolyte and a strong IR signal can be measured. Furthermore, a thick electrolyte layer can be used which allows free mass transportation to and from the catalytic surface. Despite of this, the diffusion of reactants to and products from the electrode is still ill-defined [18]. However, because the electrocatalyst has to be deposited on the ATR crystal the types of materials and deposition methods are limited [14]. Furthermore, only adsorbed species can be detected effectively [15].

Two different types of internal reflection cell configurations were found in literature [18-20]. Both are constructed in the same way as illustrated in Figure 9 and Figure 10 however they differ in flow mechanism inside the cell. Ataka et al. [20] and Matsui et al. [19] developed a spectroelectrochemical cell in which gas can be passed through a fixed amount of electrolyte which are represented in Figure 9. The left part of this figure shows a typical cross section of an ATR cell and how the electrodes are connected to the potentiostat. The top part of the cell is however missing. The right part shows the exterior of a possible ATR cell with all the electrodes including gas in- and outlet.

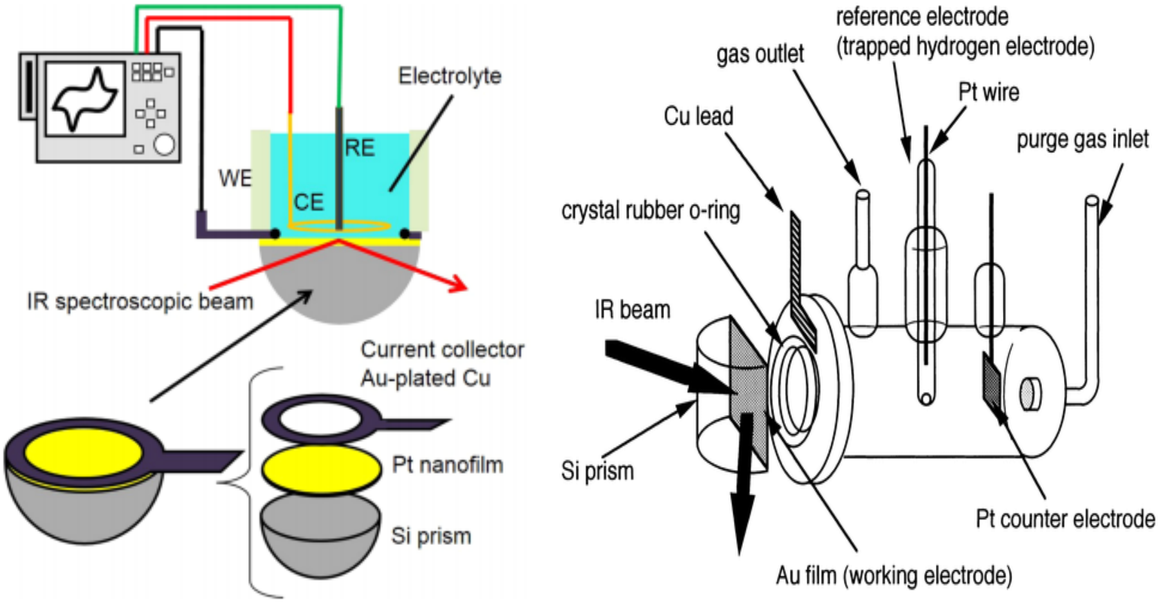

Figure 9: ATR cell configuration with fixed amount of electrolyte and gas flow. Left shows the connection to the potentiostat [19]. Right shows the gas in- and outlet of the cell [20]

The gas can either be dissolved in the electrolyte, when it is in low concentration and low flowrate, and react at the electrocatalyst working electrode or bubbled through the cell at high flow rate and react as a gas at the electrocatalytic working electrode. The latter has the advantage since the bubbling of the gas results in mixing of the electrolyte and thereby creating a uniform concentration profile in the cell. In both cases the resulting gaseous products can be easily transported from the cell via the gas outlet. This is the design of the current in use spectroelectrochemical cell.

In contrast Chen et al. [18] developed a spectroelectrochemical cell in which the electrolyte is passed through the cell as schematically is shown in Figure 10. In this design, the reactants have to be dissolved in the electrolyte before entering the cell. This is achieved by bubbling the gas through the electrolyte batch. The reference and counter electrodes are placed in the electrolyte in- and outlet respectively. In their study, they demonstrate the general potential of in situ ATR-FTIRS studies under continuous flow conditions with well-defined mass transport to/from the electrode, which is particularly important for reaction studies involving dissolved gases or other dilute reactants [18]. The obtained results were in agreement with the results of a previous study however showed faster kinetics. Combining a flow of a thin electrolyte layer to an ATR cell improved the capability of in situ ATR-FTIRS measurements, which allows mechanistic and quantitative spectroelectrochemical kinetic studies of electro catalytic reactions under well-defined mass-transport conditions [18].

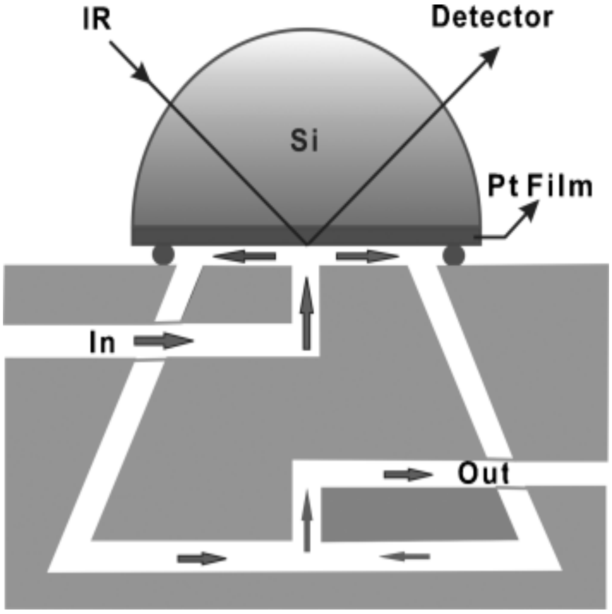

Figure 10: ATR cell configuration with electrolyte flow [18]

2.4.2. External reflection cell configuration

In the external reflection configuration, or thin layer cell, as the name already suggest, the thickness of the electrolyte is reduced to a 1-10 µm thin layer [14] between the IR transparent prism and the electrocatalytic working electrode. Thereby, the IR absorption by the electrolyte is reduced significantly and good IR illumination of the working electrode is ensured. The arrangement is conceptually simple, relying on the collection of the IR beam after reflection from a mirror-like surface [17]. Because the IR beam is reflected externally, no crystal for internal reflection is needed but a IR transparent window like calcium fluoride (CaF_2) is sufficient enough. A big advantage of this method is that the electro catalytic working electrode has not to be deposited on the IR prism itself, so that a wide range of electrode materials can be used [14] and both adsorbate and solution species involved in electrochemical reactions can be determined [15]. Because of this, the external reflection configuration has been employed most widely for in situ infrared spectroelectrochemistry. Due to the thin layer of electrolyte, mass transport from the bulk electrolyte to and from the electro catalytic electrode may be restricted which may result in strongly misleading conclusions on the reaction process owing to the depletion of reactants as well as accumulation and possibly re-adsorption of by-products [18].

In order to minimize the thickness of the electrolyte, the working electrode is pressed against the IR window. One possible way in doing this is illustrated in the left part of Figure 11 developed by Kanamura et al. [21]. A micrometre screw on top of the electrochemical cell presses the working electrode on the IR transparent window. An alternative way is to use a spacer between the IR transparent window and the working electrode [22].

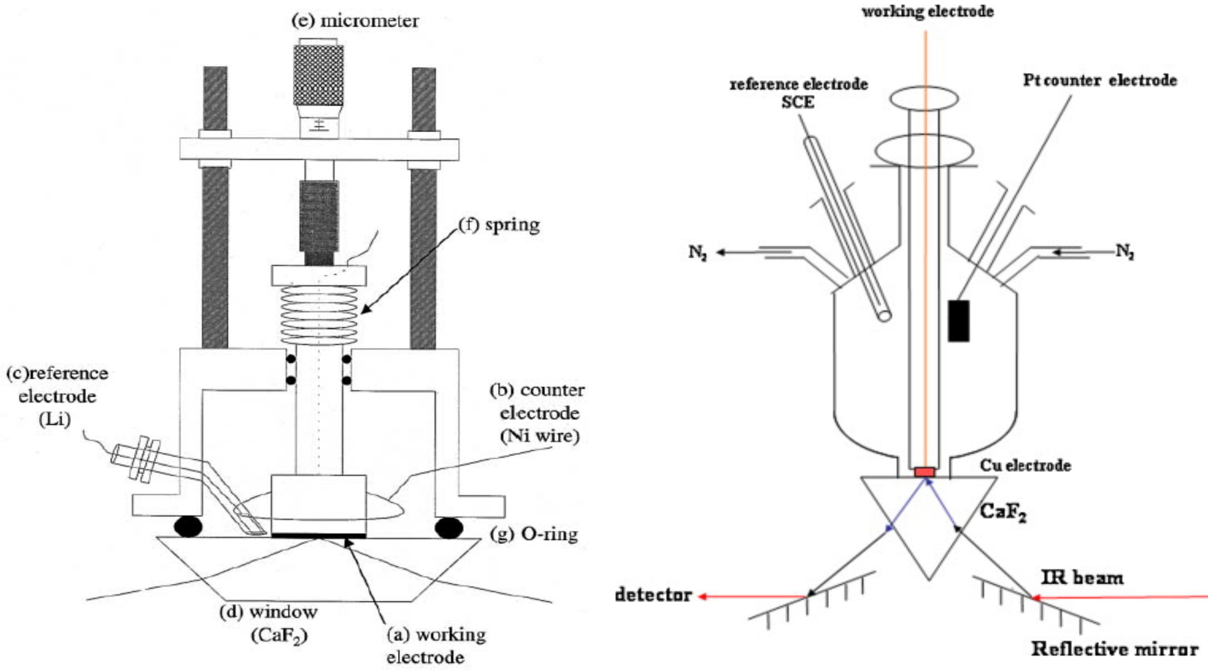

Figure 11: External reflection thin layer cell configuration. Left shows a typical cross section where the WE is pressed against the IR transparent window with a micrometre screw [21]. Right shows the cross section for a batch electrolyte cell with the gas in- and outlet [23]

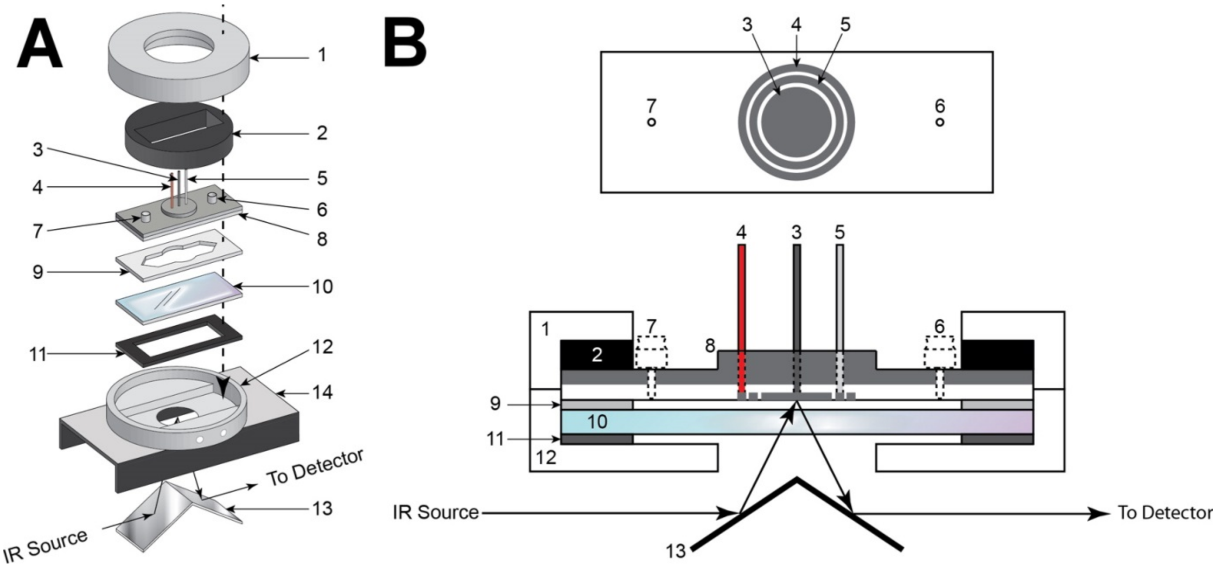

Figure 12: Schematic representation of the external reflection thin layer flow cell configuration. Left breakup of the cell into all its parts. Right bottom cross section of the cell. Right top to view of the electrodes [22]

As for the internal reflection configuration, gas [23] and electrolyte [22] flow cells are developed and studied for the external reflection configuration. The schematic representations of both cells are presented in the right part of Figure 11 and Figure 12 respectively. The gas flow cell operates differently than in the internal reflection configuration. This is due to mass transport limitations. First gas is bubbled through the electrolyte to saturate and mix it to obtain a uniform concentration. Only then the working electrode can be pushed onto the IR transparent window and a measurement can be taken. After the measurement, the working electrode has to be removed from the IR transparent window to allow mixing of the electrode again.

2.4.3. Alternative cell configurations

Most of the infrared studies are based on steady-state approaches. This means that the electrode potential is varied only at a slow scan rate which generally below 10 mV s^{-1} or is held at a constant value during the collection of infrared spectra. Generally, the steady-state infrared spectra are used to clarify the behaviour of cyclic voltammetry. The status of the electrode surface or the electrochemical reactions at a given potential though are frequently dependent on the potential scan rate, resulting that steady-state infrared spectra are inappropriate for use in interpreting the behaviour of cyclic voltammetry at a molecular level [15] and that is why short-lived intermediates and fast kinetics were hardly investigated due to the large time constant of IR cells [24]. If rapid-scan time-resolved FTIR spectroscopy with about 10 ms time-resolution is employed in cyclic voltammetry studies, the potential scan rate can be increased significantly, which definitely enriches transient information in infrared spectra. By combining the molecular information acquired from time-resolved infrared spectra with the kinetic data obtained in a cyclic voltammetry study, the dynamics of complex electrochemical reactions can be understood in great depth on a molecular scale [15, 24].

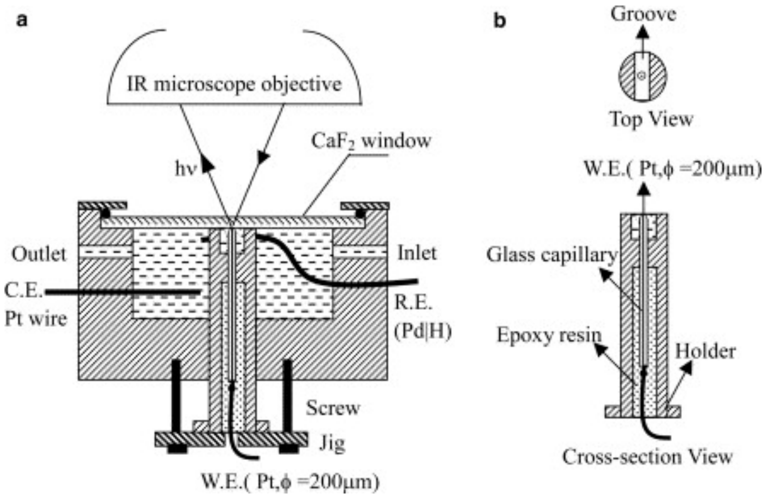

Figure 13: a) Schematic representation of the external reflection thin layer electrolyte flow spectroelectrochmical cell. b) Cross section and top view of the used micro electrode [15, 24]

It is well known that microelectrodes have an outstanding transient performance due to small interfacial capacity. Therefore, they are able increase the potential response rate and to decrease the influence of non-uniformity of current flow [15]. Zhou et al. [15, 24] combined an external reflection thin layer electrolyte flow cell with a micro electrode to overcome the drawbacks of external reflection configuration in transient response and developed a spectroelectrochemical cell for situ step-scan time-resolved microscope FTIR spectroscopy. The schematic of this cell is presented in Figure 13. As can be seen in the right part of the figure, the micro working electrode is placed in a holder. The holder has a groove at the end which is pressed to the IR transparent window so that electrolyte can be passed through the electrode. Since the electrode is fixed in the holder, the thickness of the electrolyte between the IR window and electrode is well known. The results of the studies from Zhou et al. [15, 24] showed that their newly developed In-Situ rapid-scan time-resolved microscope FTIR reflection cell is a promising tool in studying fast dynamic processes and kinetics of electrochemical reactions at molecular level.

Zandi and Hamann [25] combined the two cell designs by using an ZnSe ATR crystal in an external reflection set up as can be seen in Figure 14. Again, the working electrode is pressed against the ATR crystal in order to minimize the thickness of the electrolyte layer. This is indicated by arrow called F. In contrast to other ATR studies, the working electrode is not directly deposited on the ATR crystal but separated by a thin layer of electrolyte. The generated evanescent wave at the crystal-electrolyte interface with a penetration depth between 0.5 and 2 mm is large enough to pass through the electrolyte and is reflected at the working electrode.

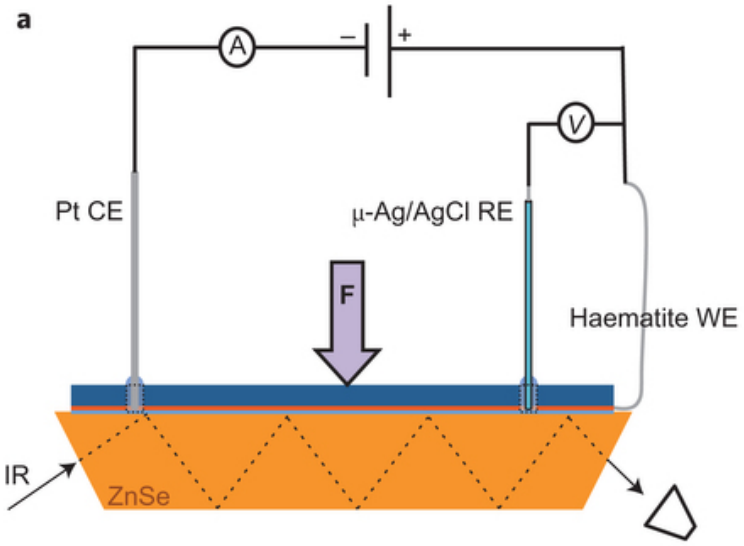

Figure 14: Schematic representation of the ATR cell with a thin layer of electrolyte between ATR crystal and working electrode [25]

2.4.4. Results of studies using the introduced cell configurations

In literature, the majority of studies used one of the above described techniques to study adsorbed species and reaction products of electrochemical oxidation and reduction reactions. Most of them however only conclude with their observations and did not compare it to results of previous or similar studies.

The electro oxidation of ethanol on a palladium electrode in alkaline media in a thin layer cell was investigated by Zhou et al. [26]. A batch cell with a fixed amount of electrolyte was used in this study. They detected adsorbed CO on the Pd electrode which was derived from the dissociative adsorption of ethanol. This adsorption was not detected in previous studies, showing that this type of spectroelectrochemical cell has a high detection sensitivity of adsorbed species on the working electrode. However, due to mass transport limitations as already discussed above the pH in the thin layer decreases in comparison to the bulk pH value by the oxidation reaction. Ultimately, due to the detection of adsorbed CO_2 it can be concluded that all the electrolyte within the thin layer is neutralized.

Machan et al. [22] developed an electrolyte flow cell for the mechanistic understanding of electrocatalysts. They investigated the electrochemical reduction of CO_2 in a thin layer cell with a small volume. Due to the cells small volume, the potential gradient is minimized and distributed uniformly in the cell. Because of this, rapid and quantitative identification of adsorbed species is possible.

The research group of Behm, from the department of Surface Chemistry and Catalysis of Ulm University in Germany, performed several spectroelectrochemical studies using the ATR cell configuration under gas and electrolyte flow conditions [18, 27-29]. Smolinka et al. [27] used an ATR gas flow cell, similar as the spectroelectrochemical cell presented in Figure 9 developed by Ataka et al. [20], to investigate the CO_2 reduction on Pt electrocatalyst and its impact on H_2 oxidation in CO_2 containing fuel cell feed gas. They used surface enhanced infrared adsorption spectroscopy (SEIRAS), which is described in section 2.3.4, to study adsorbed molecules on the surface of the Pt electrocatalyst. The Pt electrocatalyst with a thickness of 50 nm was deposited directly to the Si ATR crystal. The resulting SEIRAS spectra, for different potentials within the under potentially deposited adsorbed hydrogen region, showed despite the high sensitivity only adsorption bands related to CO adsorption and no other spectral bands that could be related to other reaction products, such as COH_{ad}, HCO_{ad}, or $COOH_{ad}$, which were recently proposed for CO_2 reduction on Pt [27]. The same result was obtained for other reduction potentials in both CO_2 saturated sulfuric acid solutions and mixtures of 20% CO_2 in H_2 sulfuric acid solutions, suggesting that CO_{ad} is the only detectable adsorbed product species for CO_2 reduction on Pt electrodes in the under potentially deposited adsorbed hydrogen region. The obtained result corresponds with the conclusions that were drawn in FTIR studies of CO_2 reduction on polycrystalline and single crystal Pt electrodes, although due to the lower sensitivity of those measurements small amounts of other adsorbates could not be ruled out [27].

The kinetics and reaction mechanism of the electro oxidation of formic acid in an ATR electrolyte flow cell configuration were studied by Chen et al. [18]. A schematic representation of the spectroelectrochemical cell is presented in Figure 10. Like Machan et al. [22], they used a small volume cell and used as, in the study of Smolinka et al. [27], Pt as electrocatalyst which is deposited directly onto the Si ATR crystal. Applying an electrolyte flow over the ATR crystal showed a significant improvement of the ATR measurement since they found new observations which showed that previous studies were incomplete. With their new gained insights, they introduced a new reaction pathway [18]. Furthermore, due to the controlled mass transport of reactants and reaction products to and from the electrode the overall reaction kinetics can be determined by measuring the Faradaic current.

Heinen et al. [29] combined the ATR electrolyte flow cell of Chen et al. [18] with an on-line differential electrochemical mass spectrometer to obtain, next to information of adsorbed molecules, a quantitative determination of volatile reaction products. Results of their experiments showed that the combination of these two techniques is a novel tool for electro catalytic studies. In a follow up study Busó-Rogero et al. [28] investigated the oxidation of ethanol on shape-controlled platinum nanoparticles at different pHs. At first glance it seems that they used the same experimental setup as Heinen et al. [29] but when looking closely to the experimental details it can be found that the electrocatalyst is not directly deposited on the ATR crystal itself but on a wafer of the same material as the ATR crystal which is in turn placed on top of the flat side of the ATR crystal in the spectroelectrochemical cell. The resulting ATR spectra showed main absorption bands corresponding to linearly adsorbed CO on the Pt electro catalyst. In contrast to previous studies no acetate absorption band was detected [28]. The absence of the acetate absorption band is because of the electrolyte flow configuration in this spectroelectrochemical cell. The in the reaction formed acetic acid is readily removed from the vicinity of the electrode by the electrolyte flow and thereby, the accumulation of weakly bound acetate on the Pt electrocatalyst is prevented and therefore not detected. The flow of electrolyte through the spectroelectrochemical cell, in this way reduces the accumulation of reaction products on the electrocatalyst surface, thus allowing a better approach to the understanding of the reaction mechanism since mainly stable adsorbed molecules are detected [28].

2.5. Infrared absorption bands in the CO_2 reduction reaction on silver

As described in section 2.3.2, an IR spectrum is obtained by scanning the sample with a range of wavenumbers within the IR domain. The resulting IR spectrum contains absorption bands which are characteristic for bonds between atoms in a certain molecule. In order to assign the present IR absorption bands in the IR spectra obtained during the CO_2 reduction reaction it is essential to know at which wavenumbers the absorption of IR radiation of the reactants, intermediates and products occur. In section 2.2.4 it is discussed that CO, based on the required energy input, market price and easy separation, is a promising reduction product. From section 2.2.5 it followed, that gold showed the highest catalytic activity but due its high price it is economic unfavourable to use. Therefore, silver, which has also a high catalytic activity for the CO formation but is less expensive than gold is more suitable. Based on these two facts, the CO_2 reduction reaction on silver is investigated in this study. As presented in section 2.2.6 Hatsukade et al. [9] found possible reaction mechanisms of the CO_2 reduction reaction on a silver catalyst. Based on these mechanisms, presented in Figure 4, it is expected that CO_2, CO and formate are present during the reaction. Furthermore, due to the competition of the HER, hydrogen is expected to be present as well. Since the CO_2 reduction reaction takes place in an aqueous electrolyte, water and carbonate species are also present.

In literature, no In-Situ IR studies of the CO_2 reduction reaction on silver were found. However, there exist several In-Situ IR studies in which not silver but a different catalyst is used. Furthermore, the above-mentioned molecules are common molecules in reactions of small organic molecules. Especially the oxidation of CO, methanol and formic acid. Observed IR absorption bands and their corresponding assignments in different In-Situ IR studies are presented in Table 3. In these studies, the IR absorption bands result from difference spectra. This means a first IR spectrum is taken at a certain condition. The condition then is changed, and a second IR spectrum is taken. In most cases there is a difference in applied potential between the two spectra. The difference spectrum is the difference between the two spectra. Increases in absorbance indicate an increase in interfacial concentration whereas decreases in absorbance indicating a loss of species absorbing at that wavenumber respectively.

Table 3: Assignment of IR absorption bands in different In-Situ IR studies

Author	Reaction	Catalyst	Electrolyte	Potential	Absorption band [cm^{-1}]	Assignment
Hori [30]	CO_2 reduction	Copper (Cu)	0.2 M $KHCO_3$	-1 V vs RHE	2080	Adsorbed CO
Collins [31]	CO_2 reduction	Palladium (Pd) / Gallium (Ga)	Gas phase	Temperature dependent	1630, 1431, 1225	Asym, sym CO_3, OH surface bound bicarbonate
					3600	Surface bound OH
					1587, 1325	Asym, sym CO_3 bidendate carbonate
					2000, 2090	Bridge, linear bonded CO
					2858,2960	Asym, sym CH_3 of bonded methanol
Baruch [32]	CO_2 reduction	Tin (Sn)	0.1 M K_2SO_4	-1.6 V vs Ag/AgCl	3500, 1650	Water vibrations
					2350	Gaseous CO_2 (doublet)
					1470-1420	Free carbonate ions
					1530-1470, 1370-1300	Monodendate carbonate
					1450	Dissolved CO_2
Pander [33]	CO_2 reduction	Indium (In), Tin (Sn), Lead (Pb), Bismuth (Bi)	0.1 M K_2SO_4	-1.6 V vs Ag/AgCl	1500, 1385	Surface bound carbonates
Heyes [34]	CO_2 reduction	Copper (Cu)	0.5 M $NaHCO_3$	-0.7 V vs RHE	2090	Adsorbed H
					2070	Adsorbed CO
					1500-1450	Adsorbed CO_3
					1650	Adsorbed H_2O
Gao [35]	CO_2 reduction	Palladium (Pd)	1 M $KHCO_3$	-1 V vs RHE	1538, 1338, 1288	Asym, sym OCO, OH dissolved formate
					1350-1450	Dissolved CO_3^{2-}/HCO_3^-
					1784	Multiple bonded CO
					1882	Bridge bonded CO
					1977	Linear bonded CO
					2345	Interfacial CO_2
					1650	Interfacial H_2O
Kumar [36]	Hydrates from CO_2	No	Gas phase	Pressure dependent	2325, 2356	Liquid CO_2
					2343, 2360	Dissolved CO_2
					2337, 2362	Gaseous CO_2
Heinen [29]	CO oxidation	Platinum (Pt)	0.5 M H_2SO_4	1.3 V vs RHE	2100-2000	Linear bonded CO
					1900-1700	Multiple bonded CO
					3650, 1630	H_2O co adsorbed with CO
					3600-3300, 1600	Water displaced by CO at the interface

Author	Reaction	Catalyst	Electrolyte	Potential	Absorption band [cm^{-1}]	Assignment
Gravejat [37]	CO adsorption	Silver (Ag) / Aluminiumoxide (Al_2O_3)	Gas phase	Temperature dependent	2036-2044	Linear adsorbed CO
					2000	Bridge bonded CO
Yang [38]	Methanol oxidation	Palladium (Pd)	0.1 M NaOH	-0.45 V vs Ag/AgCl	1678-1860	Combination of bridge and multiple bonded CO
					1620, 3604	Free H_2O
					1580	Dissolved formate
					1300-1500	Dissolved CO_3^{2-}/HCO_3^-
					2343	Dissolved CO_2
Chen [39]	Formic acid oxidation	Platinum (Pt)	0.5 M H_2SO_4	1.3 V vs RHE	2080	Linear bonded CO
					1850	Multifold bonded CO
					1322	Bridge bonded formate
					3000, 1620	Changes in water adlayer
Vigier [40]	Ethanol oxidation	Platinum (Pt), PtSn	0.1 M $HClO_4$	1 V vs RHE	2050	Linear bonded CO
					2345	Bonded CO_2
					1636	Interfacial H_2O

To create a better overview at which wavenumbers the vibrations of these molecules occur, the assignments of the absorption bands from the different In-Situ IR studies in Table 3 are combined and sorted per molecule. This results in a wavenumber range where the IR vibrations of the molecules of interest occur. The combination of the IR absorption bands and their assignment per molecule is presented in Table 4. Since the wavenumbers for these absorption bands are not for molecules absorbed on silver, these wavenumbers give only an indication where absorption bands might occur during the experiments and represent not the exact values. However, these values will be used to analyse the obtained spectra from the performed experiments.

Table 4: Combination of IR absorption band assignment per specific molecule

Molecule	Wavenumber range [cm^{-1}]	Average wavenumber [cm^{-1}]
Carbon monoxide		
linear	2090-1977	2053
bridge	2000-1808	1923
multiple	1850-1784	1817
3-fold hollow	1730	1730
Carbon dioxide		
interface	2345	2345
dissolved	2352-1450	2048
gaseous	2350	2350
Hydrogen		
surface bound	2090	2090
Water		
co adsorbed with/displaced by CO	3650-3000	3471
	1650-1600	1632
Formate		
dissolved		
asym OCO stretch	1583-1580	1582
sym OCO stretch	1338	1338
OH deformation	1288	1288
bridge bonded	1322	1322
Carbonate		
monodendate		
sym OCO stretch	1300-1371	1348
asym OCO stretch	1400-1530	1475
bidendate		
asym O stretch	1600-1587	1594
sym O stretch	1280-1325	1303
dissolved	1350-1470	1423
Bicarbonate		
surface bound		
asym CO_3^- stretch	1630-1650	1640
sym CO_3^- stretch	1431	1431
OH deformation	1225	1225
dissolved	1300-1500	1400

3. Limitations of the current and requirements for the new spectroelectrochemical cell

Based on the literature review and experience as well as the knowledge obtained during the performed experiments with the ATR cell in the past, first, the limitations of the current used ATR cell and then, the requirements for the new spectroelectrochemical cell are discussed in the following sections.

3.1. Limitations of the current spectroelectrochemical cell

The current spectroelectrochemical cell is an internal reflection, ATR, gas flow cell. As described in section 2.4.1, in this configuration the electrocatalyst, working electrode, is directly deposited onto the ATR crystal, resulting in a limitation of deposition methods and usable materials. Furthermore, the electrocatalyst, working electrode, is not easily exchangeable. Moreover, the thin deposited layer of working electrode may break down during the experiments. The ATR crystal has then to be removed from the cell first, before it can be cleaned by polishing the surface of the ATR crystal and subsequently, a new electro catalytic layer can be deposited, making this a cumbersome and time-consuming step.

In addition to that, the pH value in the cell cannot be measured and controlled. The pH value during the reaction however plays an important role since it has a great effect on the HER and the formation of carbonates in aqueous electrolytes under acidic and basic conditions respectively. The current cell is only small and won't fit the available big pH meter. Moreover, the cell uses a batch electrolyte. So, the pH value can only be measured before and after the experiment. The addition of CO_2 to the electrolyte however lowers the pH value and increases the HER. Both the HER and the CO_2 reduction reaction generate OH^- which increases the pH at the cathode and promote the formation of carbonates. Buffer electrolyte solutions can mitigate this problem. These solutions are based on carbonates or phosphates and are undesirable in spectrochemicalcells since they absorb IR radiation and the resulting absorption bands overlap with expected absorption bands from the surface adsorbed species in the region of interest.

ATR spectra are different from conventional IR transmission spectra [12]. The IR beam is reflected at the interface of the internal reflection element with the electrocatalyst. The reflection generates an evanescent wave which decays exponentially in the electrocatalyst layer resulting in a small effective penetration depth of 0.1 – 5 micrometres. The evanescent wave may be absorbed by molecules on the electrocatalyst surface. The IR beam then loses this energy, attenuation, and this energy loss is measured by the detector. A mathematical correction is needed to transform the energy loss to the absorbance. Most IR software have a standard routine for this transformation. The penetration depth of the evanescent wave is dependent on the IR wavelength, refractive index of the internal reflection element and the electrocatalyst, and the angle of incidence. Within the standard routine the refractive indexes may not be adjusted resulting in the fact that ATR spectra only approximate the IR transmission spectra since the refractive indexes are not constant with wavelength [12].

3.2. Requirements for the new spectroelectrochemical cell

The main requirement for the new spectroelectrochemical cell is the ability to easily exchange the electrocatalyst, working electrode. For this reason, the cell has to be designed in such way that the electrocatalyst is a self-contained part of the cell. As discussed in section 2.4, two configurations are possible to achieve this goal, the thin layer spectroelectrochemical cell and the ATR cell where the electrocatalyst is deposited on a wafer of the same material with the same crystal orientation as the ATR crystal which is placed on top of the flat side of the ATR crystal. For both configurations, the requirements are discussed below.

The thin layer configuration is preferred since on the one hand, the electrocatalyst has not to be deposited on the IR window in comparison to the internal reflection, ATR, setup but can placed in a holder. The holder can be removed easily from the cell and the electrocatalyst can simply be replaced within the holder. On the other hand, due to only a thin layer of electrolyte between the IR window and the electrocatalyst, a high signal to noise ratio is maintained. Another advantage of the thin layer configuration is that simple CaF_2 IR windows as well as Si, Ge and ZnSe crystals can be used to measure IR absorption via external and internal reflection respectively.

To obtain the thin layer of electrolyte between the IR window and electrocatalyst, the electrocatalyst can either be pressed on to the IR window or be separated by a spacer. In both cases the electrocatalyst has to be aligned parallel to the surface of the IR window in order to guide the reflected IR beam properly to the detector. Pressing the electrocatalyst onto the IR window can cause a small misalignment of the electrocatalyst. For example, the elecctrocatalyst can be tilted in comparison to parallel to the IR window. This can cause that the reflected IR beam is not directed back to the detector.

Furthermore, it is difficult to determine the thickness of the electrolyte layer and keep this thickness constant when changing the electrocatalyst. Using a spacer between the electrocatalyst and IR window ensures that the electrocatalyst is aligned parallel to the IR window, that the thickness of the electrolyte layer is well known and is always the same during experiments.

As mentioned in the previous section 2.4.4, the study of Zhou et al. [26] showed a serious limitation of the thin layer cell due to mass transport from the bulk electrolyte to and from the thin layer resulting in a decrease of the pH value and neutralization of the electrolyte in the thin layer. In order to keep the pH value constant in the cell and prevent electrolyte neutralization, electrolyte flow through the cell is needed. To realize this, the electrolyte has to be saturated with CO_2 first. Afterwards, it can be pumped through the cell. The pH of the saturated electrolyte can be measured before entering and after leaving the cell which is representative for the bulk pH and pH in the cell respectively. To allow electrolyte flow through the cell in- and outlet ports have to be positioned on the cell in such way that the electrolyte flow is able to flow along the electrocatalyst.

Furthermore, the spectroelectrochemical cell has to fit on the ATR accessory. The IR window has to be positioned in a holder which can be placed in the accessory. The IR window acts, as in the ATR cell configuration. as the bottom of the cell. To obtain a thin electrolyte layer, with a defined small thickness in the cell, a micrometre spacer on top of the IR window is needed. On top of this spacer a top part is needed with in- and outlet ports for the electrolyte, a holder for the exchangeable electrocatalyst above the IR window and places for the reference and counter electrode. The holder for the electrocatalyst should be between the inlet and outlet ports for the electrolyte to allow electrolyte flow along the electrocatalyst.

The recent study of Busó-Rogero et al. [28] has shown that it is also possible to exchange the electrocatalyst in a spectroelectrochemical cell with ATR configuration. Instead of depositing the electrocatalyst directly onto the ATR crystal, the electrocatalyst is deposited on a wafer of the same material of the ATR crystal and is placed on top of the flat side of the crystal. In order to have no reflection and absorption losses at the interface between the ATR crystal and the used wafer, both have to be the same crystal orientation to fit seamless together when placed on top of each other. The IR beam is then able to pass through the ATR crystal and wafer and is reflected at the interface of the wafer with the electrocatalyst and the resulting evanescent wave can probe the surface of the electro catalyst.

Advantage of this configuration is that electrolyte flow as well as gas flow is possible since there is no thin layer of electrolyte between the IR window and electrocatalyst present. Again, the cell has to fit on the ATR accessory. The wafer has to be placed in a template that fits the ATR accessory. Under the wafer the ATR crystal is placed which has to be pressed against the wafer. This can be accomplished by screwing the crystal holder to the template. Since both electrolyte and gas flow are possible the cell has to be airtight. No thin layer of electrolyte is needed in this configuration and therefore, no micrometre spacer is required but a cell middle section in the orders of centimetre is sufficient enough. Seals between the middle section and ATR accessory and top part of the cell are needed to make the cell airtight. The top part of the cell can be mounted on the middle section and has to include inlet and outlet ports to allow gas or electrolyte flow, and fittings for pH meter, reference and counter electrode. In principle, this setup is almost similar to the already present ATR configuration setup however due to the use of the wafer which has a larger surface than the ATR crystal, the cell can be made a bit larger to fit a pH meter.

The final design of the new In-Situ IR spectroelectrochemical cell takes the in this chapter discussed limitations and requirements into account and is introduced and described in the next chapter.

4. Design of the new In-Situ IR spectroelectrochemical cell

The design of the new In-Situ IR spectroelectrochemical cell is based on the literature study and the requirements that came up from the limitations of the current used In-Situ IR spectroelectrochemical cell. Since the main requirement of the new cell is the ability to easily change the electrocatalyst in the cell, as discussed in the introduction and previous chapter, it has been decided to use a thin layer cell configuration. Especially, because the deposition techniques for the electrocatalyst on the wafer of the material of the ATR crystal remain limited and that after a CO_2 reduction experiment the electrocatalyst has to be removed from the wafer since it is expensive and has to be reused. In the thin layer cell configuration, the electrocatalyst can be deposited on a cheap substrate that after a measurement can be disposed.

To overcome mass transport limitations from the bulk electrolyte to and from the thin layer, electrolyte flow through the cell is needed. This is done by pumping the electrolyte from a reservoir through the cell. In contrast to the ATR cell, CO_2 cannot be added directly to the thin layer cell. It has to be dissolved in the electrolyte first before it can enter the cell. This is done by bubbling the electrolyte reservoir with CO_2 and subsequently pump the with CO_2 saturated electrolyte through the cell.

To obtain a parallel alignment of the electrocatalyst with respect to the IR window a spacer is used in this design. Since the electrolyte is flowing between the IR window and electrocatalyst, the spacer is also responsible for sealing the cell. Furthermore, the thickness of the spacer determines the thickness of the thin layer of electrolyte. In this study, aqueous electrolytes are used. As water absorbs strongly IR radiation, it is essential to keep the layer of electrolyte as this as possible. For this reason, a 25 µm thick teflon spacer is used.

The design of the thin layer flow cell is presented in Figure 15 which shows the cross section of the cell. As can be seen, this design consists of two parts. The first part of the cell is the bottom part of the cell. It acts as a holder to fit onto the ATR accessory. In this part, the electrolyte in- and outlet as well as a slot for the Ag/AgCl reference electrode are placed. The light grey channels represent the fluid channels. The middle of the holder is milled out to allow the IR beam to reach to the IR window. A rubber seal is placed on top of the fluid channels and around the opening for the IR beam to prevent leaking. A calcium fluoride (CaF_2) IR window with drilled holes at the fluid channels of the bottom part of the cell is situated on top of the rubber seal. To ensure a constant thickness of the fluid film between the CaF_2 IR window and the silver working electrode during the experiments, the 25 µm teflon spacer is placed on top of the CaF_2 IR window. Finally, the silver working electrode with an aluminium current collector is placed on top of the teflon spacer.

The second part of the cell is the lid of the cell. It is screwed with eight screws to the bottom part of the cell indicated by the black arrows. Thereby, it pushes the working electrode, teflon spacer and calcium fluoride IR window onto the rubber seal. The teflon spacer, as mentioned before, also acts as a seal so that the electrolyte only can pass through the space between the calcium fluoride IR window and the silver working electrode. The flow path of the electrolyte through the cell is represented by the white arrows. Furthermore, the lid of the cell holds a spring-loaded connector which is pushed on the counter electrode. The Pt counter electrode in this cell is deposited directly on the CaF_2 IR window by magnetron sputtering. During magnetron sputtering process the part of the CaF_2 IR window where the IR beam has to pass through is masked in order to allow the IR beam to reach the silver working electrode and that the reflected beam can reach the detector.

Due to the 25 µm thin layer of electrolyte, the small surface area of the electrocatalyst, and the fact that cell should not leak it is difficult to fit a pH meter near the electrocatalyst. Therefore, the pH of the electrolyte is measured before entering and after leaving the cell in order to detect possible differences in the pH value of the electrolyte before and after the CO_2 reduction reaction.

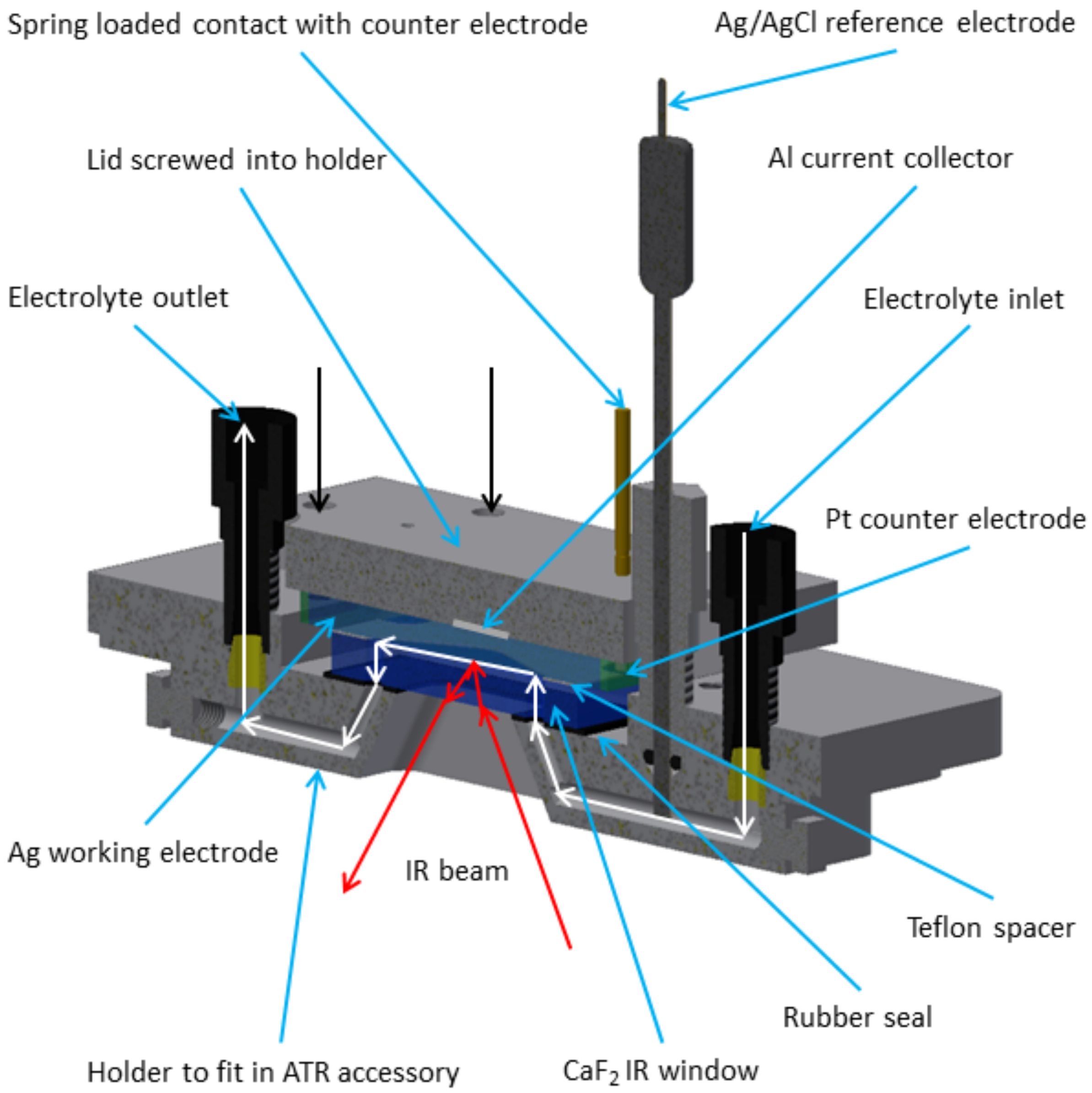

Figure 15: Schematic representation of the cross section of the new spectroelectrochemical cell

5. Experimental

To investigate if the new designed spectroelectrochemical IR cell can give new insights in the reaction mechanism of the CO_2 reduction reaction on a silver electrode a set of comparative experiments are performed. Previous research showed, that it was possible to determine a reaction pathway using the ATR cell configuration. Because of this, the experiments in this study, with the ATR- and thin layer flow cell configuration, are performed under the same conditions in order to compare the results and to investigate if it is possible to determine the reaction mechanism with the proposed new spectroelectrochemical IR cell. In this chapter, first, the experimental setup of the two spectroelectrochemical IR cell configurations are described. This is followed by how the used electrodes in the two spectroelectrochemical IR cell configurations are fabricated. This chapter ends with the description of what experiments are performed in this study.

5.1. Setup

The electrochemical reduction of CO_2 is studied in two different spectroelectrochemical cell configurations: ATR- and thin layer flow cell. Below, the experimental setup of the two cell configurations are described.

5.1.1. ATR cell

The used ATR cell in this study is a bulk electrolyte gas flow cell and consists of three parts as schematically is presented in Figure 16. The bottom of the cell is a germanium ATR crystal which is placed in a holder to fit in the ATR accessory and to attach the middle part of the cell. The working electrode, in this study silver, is deposited directly on the germanium crystal. The electrode preparation is described in detail in section 5.2.1. An aluminium foil current collector is placed along the circular edge on top of the germanium crystal. A teflon liquid cup with a volume of about 6 mL and an inner diameter smaller than the aluminium current collector is placed on top of the germanium ATR crystal and mounted to the holder. The third part of the cell is the top part. It is mounted on the teflon liquid cup and it closes the cell to ensure air tightness. Besides, it acts as a holder for the reference and counter electrodes as well as the gas inlet and outlet ports.

As can be seen from Figure 16, the IR beam has to be directed to the face of the germanium ATR crystal. This is done by the Pike Veemax III ATR accessory. It directs the IR beam from the IR spectrometer via adjustable mirrors to the face of the germanium crystal. The schematic scheme of the Pike Veemax III ATR accessory is presented in the left-hand side of Figure 17. The angle of the IR beam on the face of the germanium crystal can be adjusted between 30 and 80°. The ATR cell is placed with the holder in the Pike Veemax III ATR accessory and the electrodes are connected to a Princeton Applied Research Potentiostat/Galvanostat Model 283. The right-hand side of Figure 17 shows the connected ATR cell placed in the ATR accessory inside the Bruker Vertex 70 IR spectrometer. The black, red and white cable connects the potentiostat via the aluminium current collector to the silver working electrode, platinum counter electrode and Ag/AgCl reference electrode respectively. The CO_2 gas is fed from a CO_2 gas bottle via a teflon tube to the gas inlet of the cell.

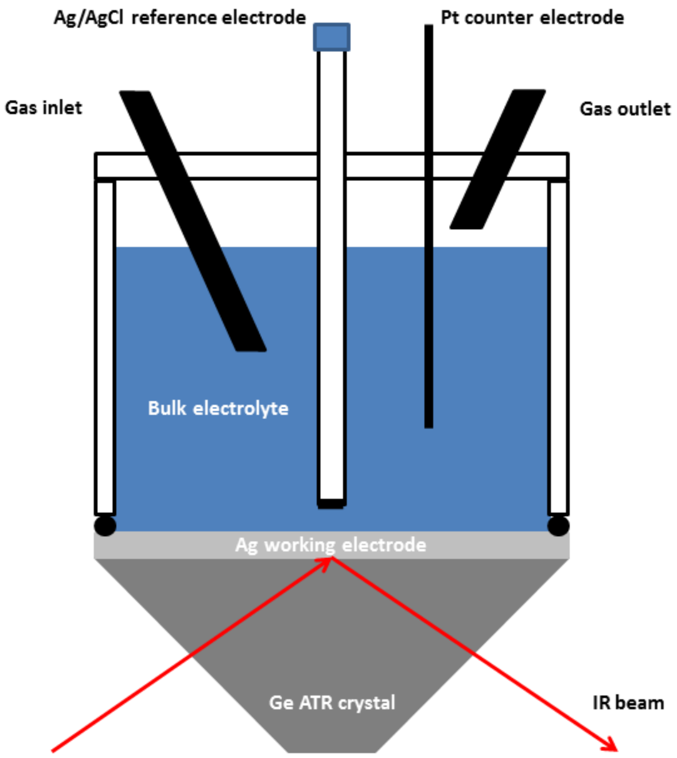

Figure 16: Schematic representation of the ATR gas flow cell configuration

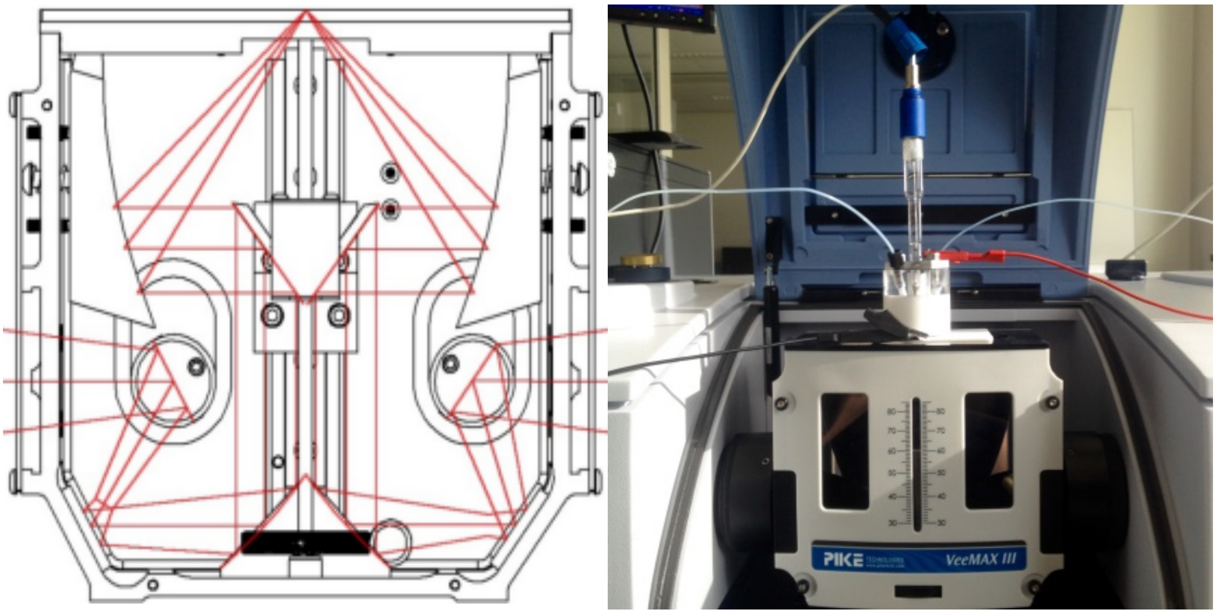

Figure 17: Left: Schematic representation of the Pike Veemax III ATR accessory. Right: To the potentiostat connected ATR cell placed in the Pike Veemax III ATR accessory inside the Bruker Vertex 70 IR spectrometer

5.1.2. Thin layer flow cell

The layout of the thin layer flow cell is already introduced in chapter 4. The schematic representation of this type of cell is shown in Figure 15. In this setup, the silver working electrode is deposited on a conducting titanium foil substrate whereas the platinum counter electrode is deposited on the calcium fluoride IR window by magnetron sputtering. The preparation of the working and counter and electrodes for this setup are described in the section 5.2.2.

The electrolyte is pushed through the flow cell by a variable speed Cole-Parmer Masterflex L/S peristaltic pump. This pump is presented in the left-hand side of Figure 18. The thin layer flow cell is placed like the ATR cell on the Pike Veemax III ATR accessory inside the Bruker Vertex 70 IR spectrometer and is connected to the Princeton Applied Research Potentiostat/Galvanostat Model 283. The right-hand side of Figure 18 shows the to the potentiostat connected flow cell placed in the Pike Veemax III ATR accessory inside the Bruker Vertex 70 IR spectrometer.

The electrolyte enters the cell on the left-hand side via a teflon tube, passes along the Ag/AgCl reference electrode and through the calcium fluoride IR window. It then follows the path defined by the teflon spacer between the calcium fluoride IR window and the silver working electrode. Subsequently, it leaves the cell on the right-hand side where the electrolyte first passes through the calcium fluoride IR window again entering the bottom part before leaving the cell. The electrolyte flow path inside the cell is represented by the white arrows in Figure 15.

The silver working electrode is connected via the aluminium current collector and the lower red cable to the potentiostat. The platinum counter electrode is connected to the potentiostat, via the spring-loaded pin which makes contact to the on the calcium fluoride IR window deposited platinum, by the black cable. The upper red cable connects the Ag/AgCl reference electrode to the potentiostat.

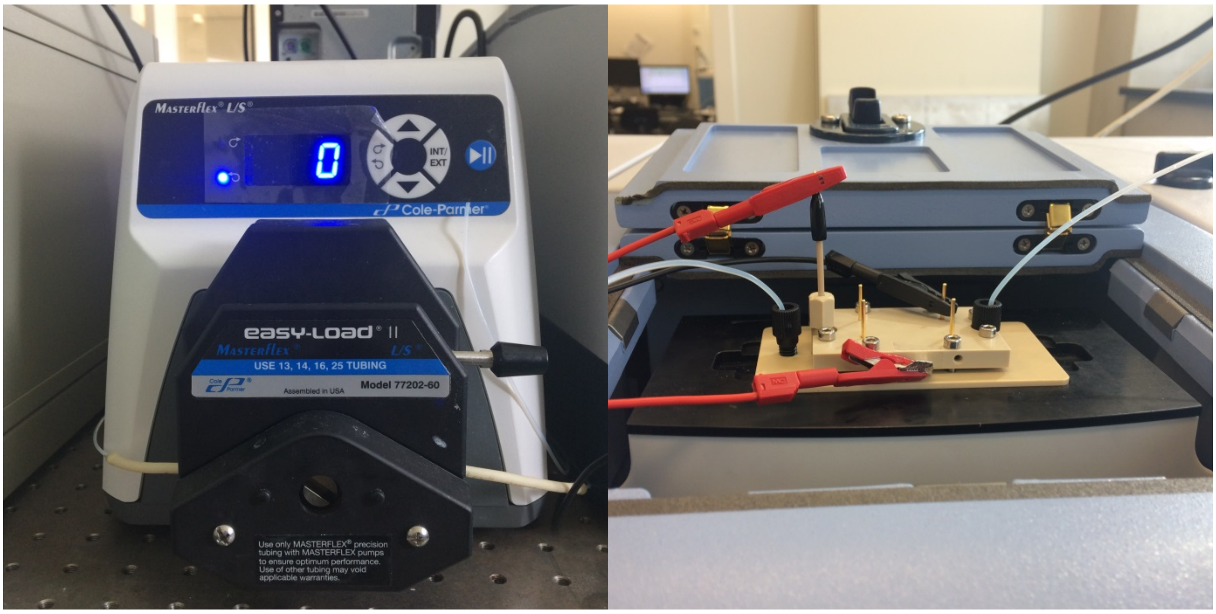

Figure 18: Left: Cole-Parmer Masterflex L/S peristaltic pump. Right: To the potentiostat connected thin layer cell placed in the Pike Veemax III ATR accessory inside the Bruker Vertex 70 IR spectrometer

5.2. Electrode preparation

As described in the previous section, the electrodes in the spectroelectrochemical cell are deposited directly on the top of the IR transparent materials or on a conducting substrate. This is done by magnetron sputtering. Magnetron sputtering is a technique to deposit a thin film of a material on a surface a substrate. In a vacuum chamber argon gas is introduced and a voltage is applied. Free electrons in the chamber are accelerated by the voltage and repelled by the cathode. When the accelerated free electrons hit an argon atom a plasma is generated. The positively charged argon ions in the plasma are accelerated towards the cathode where they hit on the target material. Due to energy exchange atoms and electrons from the target are released which can reach the substrate to form a thin layer.

Magnets behind the cathode trap the free electrons in a magnetic field directly above the target surface so that they cannot reach the substrate and that the recombination with argon ions is limited. Furthermore, when electrons are trapped in the magnetic field, it enhances their probability of ionizing a neutral gas molecule by several orders of magnitude. The increase in available ions significantly increases the rate at which target material is bombarded and subsequently deposited onto the substrate. In the two sections below, the electrode preparation for the ATR- and thin layer flow cell are described.

5.2.1. ATR cell

Before the deposition of the electrode material on the germanium ATR crystal, the surface of the germanium ATR crystal is polished with 1 µm diamond polish solution to ensure a flat surface. After polishing, the germanium ATR crystal is first rinsed with methanol to remove the oil-based diamond polish solution. Afterwards it is rinsed with water to remove the traces of methanol. Subsequently, the germanium ATR crystal is submerged in water and is placed in a EMAG Technologies Emmi-30HC ultrasound sonicator. It is then sonicated with an ultrasound efficiency of 50% for 10 minutes to ensure that the 1µm diamond particles are removed from the surface.

After cleaning the germanium ATR crystal, it is dried with nitrogen and mounted on a sample holder. The sample holder is then placed in the vacuum chamber of the AJA sputtering system. First the substrate, the germanium ATR crystal, is cleaned by bombarding it with argon plasma for 2 minutes at 20 W. Thereafter, a 20 nm layer of silver is deposited at 50 W DC power on the germanium ATR crystal.

From previous performed experiments, it is known that the thin silver layer does not stick well onto the surface of the germanium ATR crystal. Due to this reason, a 5 nm thin adhesive layer of titanium was deposited below the silver layer. This adhesive layer however showed a decrease in the surface enhancement of the infrared absorption. Therefore, the CO_2 reduction experiments are performed with only a layer of 20 nm of silver sputtered directly on the germanium ATR crystal.

5.2.2. Thin layer flow cell

Unlike as in the ATR cell configuration, where the counter electrode is a platinum wire and the silver working electrode is deposited on the optical crystal, the platinum counter electrode is deposited on the optical IR window and the silver working electrode on a titanium foil substrate in the flow cell configuration. Again, before the electrode materials can be deposited on the substrates, the substrates have to be cleaned.

The cleaning procedure for the calcium fluoride IR window is the same as for the germanium ATR crystal and is already described in the previous section. After cleaning the calcium fluoride IR window, it is dried with nitrogen and mounted on a sample holder. The sample holder is then placed in the vacuum chamber of the AJA sputtering system. First the substrate, the calcium fluoride IR window, is cleaned by bombarding it with argon plasma for 2 minutes at

20 W. Then, first a titanium adhesive layer of 5 nm is deposited via magnetron sputtering at 200 W DC power on the calcium fluoride IR window. Finally, a 100 nm platinum layer is deposited at 60 W DC power on top of the titanium on the calcium fluoride IR window.

The preparation of the silver working electrode involves different steps, since titanium foil is used as substrate instead of the germanium ATR crystal or calcium fluoride IR window. First, the titanium foil has to be cut in the right dimensions to fit on top of the teflon spacer in the thin layer flow cell. Then, the titanium foil has to be cleaned to remove all impurities. This is done by first washing the foil with soap followed by four 15 min washing steps in the EMAG Technologies Emmi-30HC ultrasound sonicator at 100% ultrasound efficiency. First in nitric acid, followed by acetone and ethanol and finally with water. Subsequently, the titanium foil is immersed in isopropanol and spin dried. The dried foil is then mounted on a sample holder and placed in the AJA vacuum chamber where it is first cleaned by bombarding it with argon plasma for 2 minutes at 20 W. Then, a 50 nm silver layer is deposited at 50 W DC power on the titanium film.

5.3. Experiments

In this section, the performed experiments with the ATR and thin layer flow cell are introduced and the experimental procedures are described. First, experiments with the ATR cell configuration are carried out. The experiments performed with the thin layer flow cell are based on the obtained results of the ATR experiments and performed under identical conditions in order to be able to compare them.

5.3.1. ATR cell

All measurements with the ATR cell are performed on a germanium ATR crystal with a face angle of 60° and a fixed angle of incidence of the IR beam set by the Pike Veemax III ATR accessory at 60°. First, the reference IR absorption spectra of the different electrolytes are measured. Then, the IR absorption spectra during the CO_2 reduction experiments at different applied potentials in different electrolytes are measured. All the ATR-FTIR spectra are collected with the OPUS software. For each spectrum, 64 scans are collected at a resolution of 4 cm^{-1} and an aperture of 1.5 mm in the wavenumber range of 800-4300 cm^{-1}.

5.3.1.1. Reference IR absorption spectra

Before the CO_2 reduction measurements under applied potential are performed, first, IR reference absorption measurements without applying a potential are carried out on a bare germanium ATR crystal to determine the absorption peaks of air, water and the aqueous electrolytes. The electrolytes used in this study are 0.1 M KCl, 0.1 M $KHCO_3$, 0.1 M K_2HPO_4 and 0.1 M $KClO_4$. To determine the reference IR absorption spectra, the bare germanium ATR crystal is installed in the bottom part of the spectroelectrochemical cell which is then placed on the Pike Veemax III ATR accessory inside the Bruker Vertex 70 IR spectrometer.

First, an air reference IR absorption spectrum is measured. The open and empty cell is placed on the ATR accessory. Since the cell is open, the cell is filled with air from the surrounding. After flushing the ATR accessory with nitrogen for 5 minutes, a background spectrum is taken. After another 5 and 10 minutes, absorption measurements with respect to the background spectrum are taken.

The reference IR absorption spectrum of water is measured against an air background IR absorption spectrum. The measurement procedure is the same as described above. The empty, open with air filled from the surrounding cell is placed in the ATR accessory. After 5 minutes, an air background spectrum is taken. The cell is then filled with water and after 5 and 10 minutes, absorption measurements were performed.

The above introduced electrolytes are measured against a water background IR absorption spectrum. In this case, the cell is filled with water and placed in the ATR accessory. After flushing the ATR accessory with nitrogen for 5 minutes a water background IR absorption spectrum is taken. Then, the water in the cell is replaced by the electrolyte and the IR absorption is measured against the water background IR absorption after 5 and 10 minutes.

Since the ATR accessory is only flushed with nitrogen for 5 minutes, traces of water and CO_2 from the air can still be present inside the ATR accessory that will disturb the IR signal. To investigate this effect, all the above measurements are repeated with atmospheric compensation, a measurement tool in the OPUS software which subtracts water and CO_2 absorption from the measured background and absorption IR spectra.

In the CO_2 reduction measurements, the electrolytes in the cell are saturated with CO_2. This is done by bubbling CO_2 with a flowrate of 6.6 cm^3/min through the electrolyte inside the ATR cell. To investigate the influence of the present CO_2 on the IR absorption spectra of the electrolytes, the same IR absorption measurements are carried out as the measurements performed without CO_2. In these measurements, the cell is closed air tight with the top part of the cell after taking the background IR absorption measurement. CO_2 is bubbled for 15 minutes to saturate the cell, water and the electrolytes respectively. After 15 and 20 minutes, IR absorption measurements are executed with corresponding backgrounds as described above.

Furthermore, the CO_2 reduction reaction takes place at the working electrode. In this study a 10 nm silver layer, is deposited on a 5 nm titanium adhesion layer which is deposited directly onto the germanium ATR crystal. To investigate the effect of these layers on the ATR crystal on the IR absorption spectra the same measurements are conducted as with the bare germanium ATR crystal.

5.3.1.2. IR absorption spectra of the CO_2 reduction reaction

The 5 nm thin adhesive layer of titanium showed a decrease in the surface enhancement of the infrared absorption. Due to this, the experiments on the CO_2 reduction reaction are performed with only a layer of 20 nm of silver sputtered directly on the germanium ATR crystal.

Experiments for the CO_2 reduction reaction are performed with the different electrolytes at three different potentials: -1.4V, -1.6V and -1.8V vs Ag/AgCl reference electrode. The ATR cell is filled with 5 mL of electrolyte, closed airtight and then flushed with CO_2 for one hour to ensure that the electrolyte is saturated with CO_2 before applying a potential.

The ATR cell is placed on the Pike Veemax III ATR accessory within the Bruker Vertex 70 IR spectrometer. The ATR accessory is flushed for an hour with nitrogen to remove contaminants as water vapour and CO_2 from the air, which enter the accessory when placing the ATR cell onto it. This is necessary because otherwise the presence of water vapour and CO_2 inside the accessory will disturb the IR absorption and interfere with the absorption spectra.

After flushing the ATR cell and accessory with CO_2 and nitrogen respectively, background IR absorption measurements are carried out to check the IR absorption signal. A background scan is made and after 10 minutes an IR absorption spectrum is taken. This is repeated three times to ensure a steady flat IR absorption spectrum around 0% absorption.

When the background signal shows the desired shape, the Princeton Applied Research Potentiostat/Galvanostat Model 283 is connected to the ATR cell and the open circuit (OC) voltage is determined. A new background IR spectrum is taken and then the voltage is ramped to one of the above mentioned desired potentials with a rate of 5 mV/s. Ramping of the voltage to the applied potential is necessary to prevent delamination and cracking of the thin layer of silver on the germanium ATR crystal which occurs when the sudden change in applied potential is high. Eleven IR absorption spectra are taken, starting after one minute when the desired potential was reached, in intervals of three minutes. In addition, the current flowing through the cell during the measurement is monitored. After the measurement, also the pH of the electrolyte is measured.

5.3.1.3. Effect of the face angle of the germanium ATR crystal on the IR absorption spectrum during the CO_2 reduction reaction

As introduced in section 2.4.1 of the literature review, ATR-FTIR spectroscopy is based on the evanescent wave which is generated when the IR beam is reflected at the interface of the germanium ATR crystal with the sample. The penetration depth of the evanescent wave depends on the IR wavelength, refractive index of the ATR crystal and the sample, and the effective angle of incidence which is a function of the set angle of the Pike Veemax III ATR accessory and the face angle of the ATR crystal. The calculation of the penetration depth of the evanescent wave is described in detail in section 6.1.2.4 of the results.

Since there are germanium ATR crystals with different face angles available, the penetration depth of the evanescent wave differs. To investigate the effect of the difference in penetration depth of the evanescent wave on the IR absorption spectra during the CO_2 reduction reaction, the CO_2 reduction measurement in 0.1 M $KHCO_3$ at an applied potential of -1.6 V vs Ag/AgCl is repeated on a germanium ATR crystal with a face angle of 45°. The set angle of incidence of the IR beam was kept at 60° in order to compare the resulting IR absorption spectra.

5.3.2. Thin layer flow cell

As mentioned in the introduction of this chapter, the performed experiments with the thin layer flow cell are based on the results from the ATR experiments. The obtained ATR IR absorption spectra in 0.1 M K_2HPO_4 and 0.1M $KClO_4$ did not give any additional information on the present species at the surface of the working electrode. Therefore, experiments with the thin layer flow cell are only performed with the 0.1 M KCl and 0.1 M $KHCO_3$ electrolytes. As in the ATR configuration, all the FTIR spectra are collected with the OPUS software. For each spectrum, 64 scans are collected at a resolution of 4 cm^{-1} in the wavenumber range of 800-4300 cm^{-1}.

Since the thin layer flow cell is a new developed cell, no data on the electrochemical performance and flow rates of the pump exist. Therefore, before starting with the IR absorption experiments the pump has to be calibrated and the electrochemistry of the thin layer flow cell is tested using cyclic voltammetry. Then, as in the performed ATR experiments, first, the reference IR absorption spectra of the electrolytes are measured and subsequently the IR absorption spectra at different applied potentials in with CO_2 saturated electrolytes are measured.

5.3.2.1. Calibration of the flow rate of the pump

The thin layer flow cell is assembled as described in chapter 4. The inlet of the variable speed Cole-Parmer Masterflex L/S peristaltic pump, a teflon tube, is immersed in water. The peristaltic pump is operated by setting the RPM. The pump sucks in the water and pushes it through the flow cell. When the cell is leak free, the flow rate of the pump is determined by setting the RPM and measuring the amount of mL pushed through the cell per minute in a 10 mL measuring cylinder.

5.3.2.2. Electrochemistry of the thin layer flow cell

The electrochemistry of the flow cell is tested using cyclic voltammetry. After assembling the flow cell, it is checked if it is leak free by pumping water through it. The water is then replaced with CO_2 saturated 0.1 M KCl electrolyte and the thin layer flow cell is then connected a Princeton Applied Research AMETEK PARSTAT 4000 potentiostat. First, the influence of the applied potential is investigated by cycling the potential from 0 V to -1.4, -1.6 and -1.8 V vs Ag/AgCl reference electrode respectively and back to 0 V at a flow rate of 1 mL/min. Then, the influence of the flowrate is investigated by cycling at a fixed applied potential of -1.4 V vs Ag/AgCl at 1, 3 and 5 mL/min.

5.3.2.3. Reference IR absorption spectra

The thin layer flow cell is placed on the Pike Veemax III ATR accessory inside the Bruker Vertex 70 IR spectrometer. Before performing the reference IR absorption measurements, the set angle on the Pike Veemax III ATR accessory and the aperture of the IR beam have to be determined which yields the highest IR signal. This is done first with an empty cell, which means there is no liquid between the calcium fluoride IR window and the silver working electrode, and second with water flowing through the cell, by varying the set angle between 30 and 80° on the Pike Veemax III ATR accessory and measuring the IR signal strength. The set angle of on the ATR accessory at which the IR signal is strongest is used during the IR absorption measurements.

The reference IR absorption spectra of the two electrolytes are determined in the same way as in the ATR cell configuration. The Pike Veemax III ATR accessory is flushed for 30 minutes with nitrogen to ensure that no water vapour and CO_2 are present anymore. Water is pumped through the flow cell at 5 mL/min and the IR absorption spectrum is measured and used as background IR absorption spectrum. The water is then replaced by the electrolyte and the IR absorption is measured against the water background IR absorption spectrum.

During the CO_2 reduction measurements, CO_2 is bubbled through the electrolytes. In order to investigate the influence of the present CO_2 in the electrolyte on the IR absorption spectrum, the IR absorption of the with CO_2 saturated electrolyte is measured against the unsaturated electrolyte IR absorption background.

5.3.2.4. IR absorption spectra of the CO_2 reduction reaction

The CO_2 reduction experiments are performed in with CO_2 saturated 0.1 M KCl and 0.1 M $KHCO_3$ electrolytes at the same applied potentials as used in the ATR experiments, -1.4, -1.6 and -1.8V vs Ag/AgCl in order to compare the obtained results, and a flow rate of 5mL/min. The electrolytes are saturated with CO_2 by bubbling CO_2 for one hour through the electrolytes.

The thin layer flow cell is placed on the Pike Veemax III ATR accessory and flushed with nitrogen for one hour to remove contaminants as water vapour and CO_2 from the air, which enter the accessory when placing the thin layer flow cell onto it. This is necessary because otherwise the presence of water vapour and CO_2 inside the accessory will disturb the IR absorption and interfere with the absorption spectra.

The CO_2 saturated electrolyte is pumped through the cell and a background IR scan is made and after 10 minutes an IR absorption spectrum is taken. This is repeated three times to ensure a steady flat IR absorption spectrum around 0% absorption. When the background signal shows the desired shape, the Princeton Applied Research Potentiostat/Galvanostat Model 283 is connected to the ATR cell and the OC voltage is measured. A new background IR spectrum is taken and then the voltage is ramped to one of the desired potentials mentioned above with a rate of 5 mV/s. Four IR absorption spectra are taken, starting at one minute after reaching the applied potential and then in three-minute intervals. During the measurements the current flowing through the cell is also monitored.

5.3.2.5. Influence of the flow rate of the electrolyte on the IR absorption spectra during the CO_2 reduction reaction

The investigation of the electrochemistry of the thin layer flow cell using cyclic voltammetry at a fixed applied potential of -1.4 V vs Ag/AgCl at different electrolyte flow rates of 1, 3 and 5 mL/min showed different current characteristics as is presented in section 6.2.2. In order to investigate the influence of the electrolyte flow rate on the IR absorption spectra during the CO_2 reduction reaction, the CO_2 reduction measurement in 0.1 M $KHCO_3$ at an applied potential of -1.6 V vs Ag/AgCl is repeated with an electrolyte flow rate of 1 and 3 mL/min.

6. Results and discussion

In this chapter, the experimental results are presented, analysed and discussed. First, the results of the performed experiments with the ATR cell configuration are presented and analysed. Previous research performed with this cell configuration showed that it was possible to determine a reaction mechanism for the CO_2 reduction reaction [41]. Therefore, the experimental results obtained in this study will be used as a reference case. Second, the results of the performed experiments with the thin layer flow cell configuration are presented and analysed. Finally, the obtained results from the experiments performed with the thin layer cell configuration are compared to the results obtained with the ATR cell configuration to determine if these results can give new insights in the CO_2 reduction reaction mechanism.

6.1. ATR cell configuration

In this section, the ATR FTIR absorption spectra measured during the CO_2 reduction reaction are presented. First, the IR spectra of the reference measurements of the different electrolytes, 0.1 M KCl, 0.1 M $KHCO_3$, 0.1 M K_2HPO_4 and 0.1 M $KClO_4$, on the bare germanium ATR crystal are presented. Subsequently, these spectra are compared to the ATR FTIR absorption spectra measured on the germanium ATR crystal with a combined layer of 5 nm titanium and 10 nm silver and a single thin silver layer of 20 nm to determine the influence of the thin electrode layer on the absorption spectra.

Then the ATR FTIR absorption spectra of the CO_2 reduction reaction measurements at the three different applied potentials of -1.4, -1.6 and -1.8 V vs Ag/AgCl are presented. Since ATR FTIR spectroscopy makes use of an evanescent wave as described in the literature review, it is dependent on the penetration depth of the evanescent wave. The penetration depth of the evanescent wave is calculated for two germanium ATR crystals with different face angles, 45 and 60° respectively and the IR absorption spectra are compared.

6.1.1. Reference IR absorption spectra

Figure 19 shows the absorption spectra of air, water and the electrolytes without and saturated with CO_2 taken after 10 and 20 minutes respectively. As can be seen there are a lot of disturbances in the IR absorption spectra in the regions between 1400-1900 cm^{-1} and 3600-3900 cm^{-1}. These disturbances are caused by water and CO_2 traces from air which are present inside the ATR accessory. Air can enter the ATR accessory when the cover is removed to place the spectroelectrochemical cell on it. Furthermore, the spectroelectrochemical cell is removed from the ATR accessory after taking the background spectrum to fill the cell with water and replace the water with the electrolytes respectively. Flushing the ATR accessory for 20 minutes with nitrogen is thus not sufficient enough to remove the traces of water and CO_2 from air inside the ATR accessory.

The OPUS IR measurement software has an atmospheric compensation tool. This tool subtracts the IR absorption of the atmosphere from the measured IR absorption spectrum. Figure 20 shows the IR absorption spectra with atmospheric compensation. Comparing these IR spectra to the ones without atmospheric compensation, one can see that the overall shape of the IR spectra does not change and that the disturbances disappeared in the two regions. For this reason, it is assumed that the atmospheric compensation tool can be used on absorption measurements with short flushing times of the ATR accessory to give representative IR absorption spectra. Therefore, all reference IR measurements are performed with the atmospheric compensation tool in order to save time when performing the measurements, since flushing the ATR accessory is a time-consuming step.

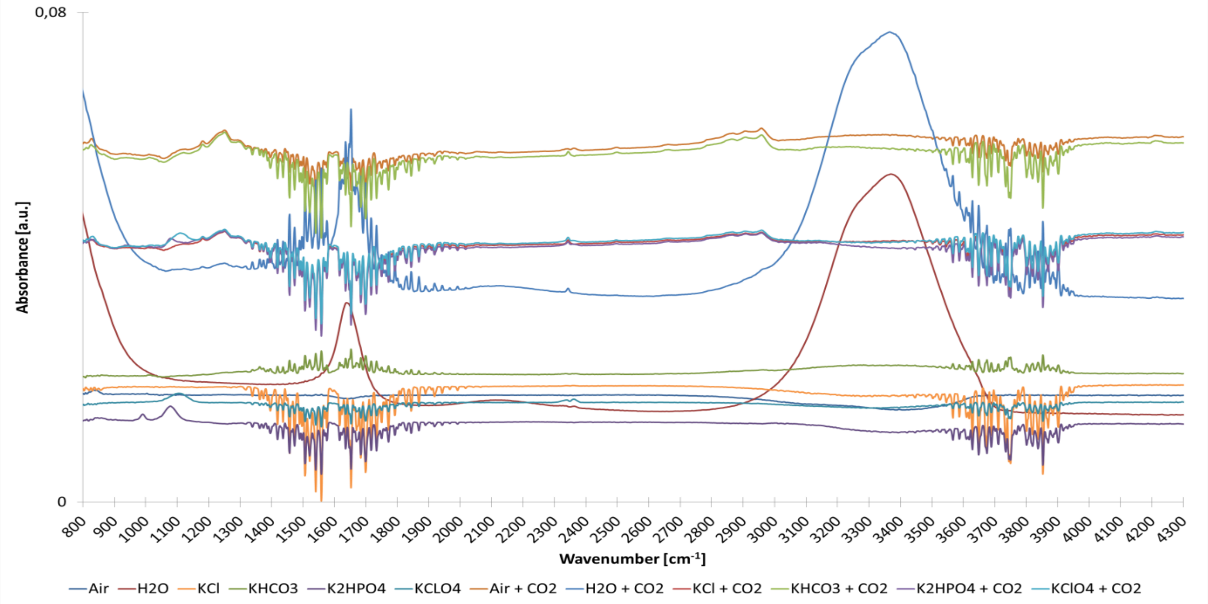

Figure 19: Reference ATR FTIR absorption spectra measured on the bare germanium ATR crystal

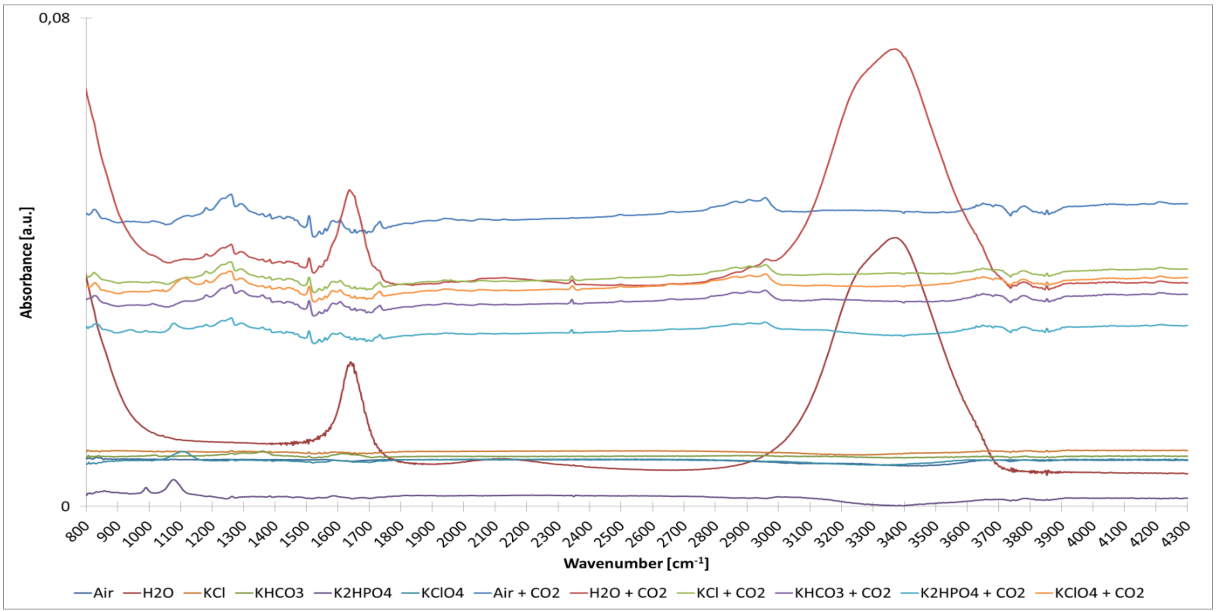

Figure 20: Reference ATR FTIR absorption spectra with atmospheric compensation measured on the bare germanium ATR crystal

For the CO_2 reduction experiments however, to be sure that no traces of water and CO_2 are present in the ATR accessory, the ATR accessory is flushed with nitrogen for at least one hour. Before starting the CO_2 reduction experiments, this is checked by measuring the IR absorption of the electrolyte against the electrolyte IR background spectrum. When the absorption spectrum becomes a flat line, one can be sure that no traces of water and CO_2 are present in the ATR accessory anymore.

6.1.1.1. Bare germanium ATR crystal

Figure 20 shows the absorption spectra of air, water and the electrolytes without and saturated with CO_2 taken after 10 and 20 minutes respectively with atmospheric compensation. These spectra are measured in the way as described in section 5.3.1.1. The IR absorption spectra of water are measured against an air background spectrum and result in strong IR absorption bands compared to the electrolytes which are measured against a water background spectrum. Since water and air are not used in the reduction measurements and in order to get a better look at the IR absorption spectra of the electrolytes which are more important, the IR absorption spectra of water and air are removed. Figure 21 shows the same spectra as in Figure 20 but now without the ones of air and water.

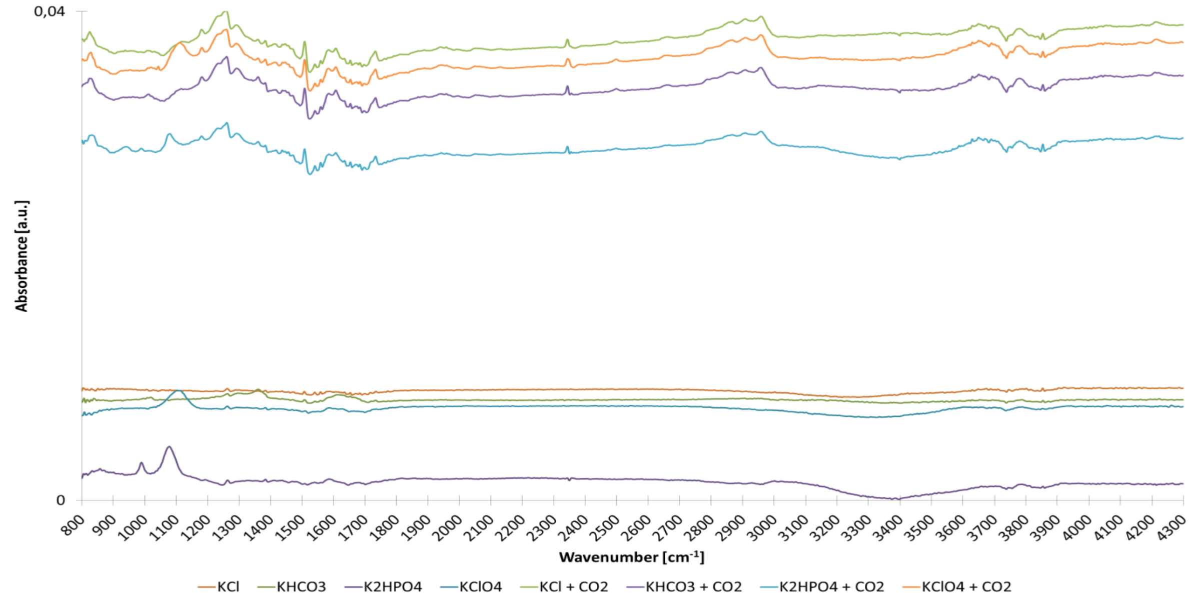

Figure 21: Reference ATR FTIR absorption spectra of the electrolytes with atmospheric compensation measured on the bare germanium ATR crystal

What immediately is noticeable, is that the spectra of with CO_2 saturated electrolytes show a higher IR absorbance. Furthermore, these spectra are exactly the same for wavenumbers higher than 1200 cm^{-1}. For wavenumbers smaller than 1200 cm^{-1}, the spectra are similar, but the spectra obtained in 0.1 M K_2HPO_4 and 0.1 M $KClO_4$ show an absorption peak at 1100 and 1150 cm^{-1} respectively. By taking a closer look at the spectra of these electrolytes without CO_2, presented in Figure 22, it can be seen that these absorption bands are here present as well so that they correspond to the electrolyte and not to the dissolved CO_2 in the electrolyte. So, from the spectra of the with CO_2 saturated electrolytes no difference can be observed between the different electrolytes. Therefore, only the absorption spectra of the electrolytes against a water background are considered as reference spectra.

Figure 22 shows a close up of the absorption spectra of the electrolytes used in this study. As already mentioned, these spectra are taken against a water background. As can be seen, all spectra show a decrease in IR absorption at a wavenumber around 3300 cm^{-1}. This corresponds to the displacement of water at the surface of the germanium ATR crystal. The two dips around 3800 cm^{-1} can be contributed to organic contaminants present in the cell during the measurement or what is more likely, since the ATR accessory is only flushed with nitrogen for a short time, water vapour from air present in the ATR accessory.

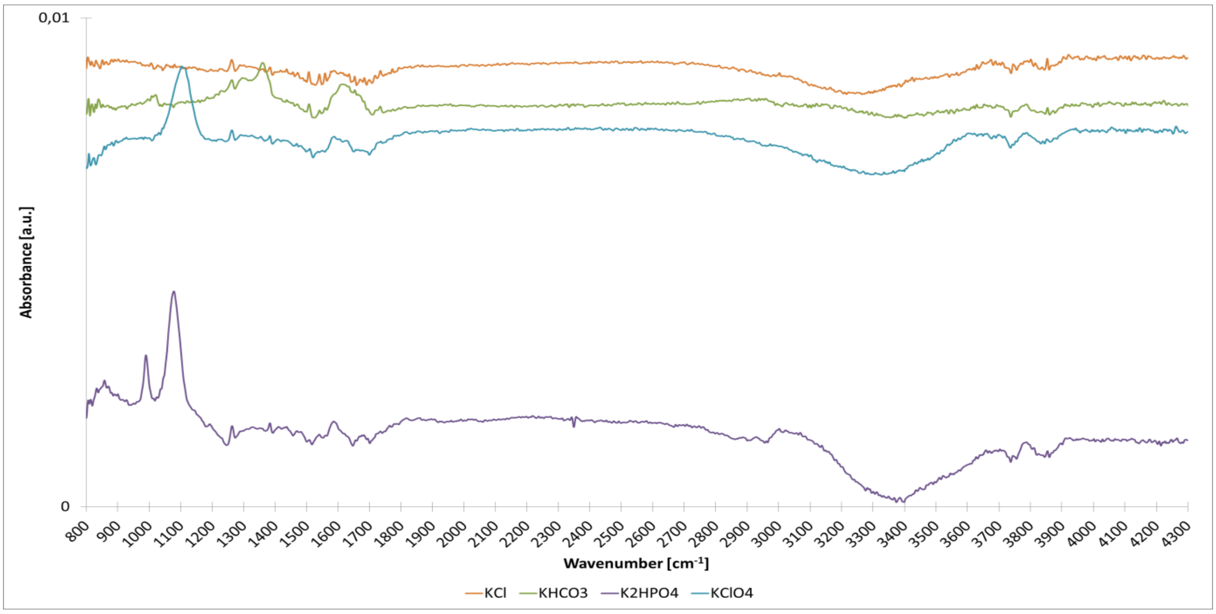

Figure 22: Reference ATR FTIR absorption spectra of the electrolytes without CO_2 with atmospheric compensation measured on the bare germanium ATR crystal

At the lower wavenumber regime, 900-1800 cm^{-1}, the spectra differ from each other. Whereas the spectrum of 0.1 M KCl does not show any absorption and or desorption bands, the spectra of the other electrolytes do. The spectrum of 0.1 M $KHCO_3$ shows two broad absorption peaks around 1360 and 1610 cm^{-1}. According to the literature review, presented in Table 3, these peaks correspond to surface bond bidendate carbonate [31]. However, since there is no charge present on the germanium ATR crystal during the measurements of the IR reference absorption spectra it is not likely that carbonate will bond to the germanium surface. Due to this, it is expected that the two absorption bonds correspond to the dissolved carbonate in the electrolyte. The spectra of both 0.1 M K_2HPO_4 and 0.1 M $KClO_4$ show an absorption peak at around 1100 cm^{-1}. The peak in 0.1 M $KClO_4$ is broader whereas the peak in 0.1 M K_2HPO_4 is sharp and larger. In addition to the sharp peak at around 1100 cm^{-1} the spectrum of 0.1 M K_2HPO_4 shows a second sharp but lower absorption peak at around 990 cm^{-1}. These absorption bands can be assigned to asymmetric and symmetric stretch vibrations of P-O in K_2HPO_4 [42]. The absorption peak at a wavenumber of 1100 cm^{-1} in 0.1 M $KClO_4$ corresponds to the asymmetric Cl-O stretching bands [43]. The IR absorption peaks corresponding to the electrolytes measured on the bare germanium ATR crystal are summarized in Table 5 below. A minus sign in front of a wavenumber in this table indicates a negative absorption band corresponding to a displacement of a molecule.

Table 5: Summary of the IR absorption bands present in the reference IR spectra corresponding to the electrolytes on the bare germanium ATR crystal and the germanium ATR crystal with a 20 nm layer of silver

Electrolyte	**Absorption band [cm^{-1}]**		**Assignment**
	Bare Ge	**Ge with 20 nm Ag**	
0.1 M $KHCO_3$	1363, 1619	1365, 1635	Dissolved carbonate
0.1 M K_2HPO_4	989, 1077	990, 1080	Sym, asym stretch of P-O
		-1680	Displacement of H_2O
0.1 M $KClO_4$	1104	1100	Asym stretch of Cl-O
		-1690	Displacement of H_2O

6.1.1.2. Influence of the thin electrode layer on the germanium ATR crystal

The CO_2 reduction reaction takes place at the working electrode inside the ATR spectroelectrochemical cell. In the ATR cell configuration, the working electrode is deposited directly on the germanium ATR crystal. To investigate the influence of the thin electrode layer on top of the germanium ATR crystal on the IR absorption spectra of the electrolytes in comparison to the IR absorption spectra on the bare germanium ATR crystal, reference IR absorption measurements are performed on the germanium ATR crystal with a thin layer of electrode as well. In this study, a thin layer of silver is used as working electrode. From previous research, it is known that silver does not stick on the germanium ATR crystal very well and when a potential is applied to the silver, the thin layer of silver breaks and releases from the germanium ATR crystal. For this reason, a thin layer of titanium is deposited first on the germanium ATR crystal. The titanium layer acts as an adhesive layer for the silver. In this study, a 5 nm titanium adhesive layer and a 10 nm layer of silver as working electrode is used. Figure 23 shows the absorption spectra of the electrolytes against a water background on the germanium ATR crystal with a 5 nm adhesive layer of titanium and a 10 nm layer of silver.

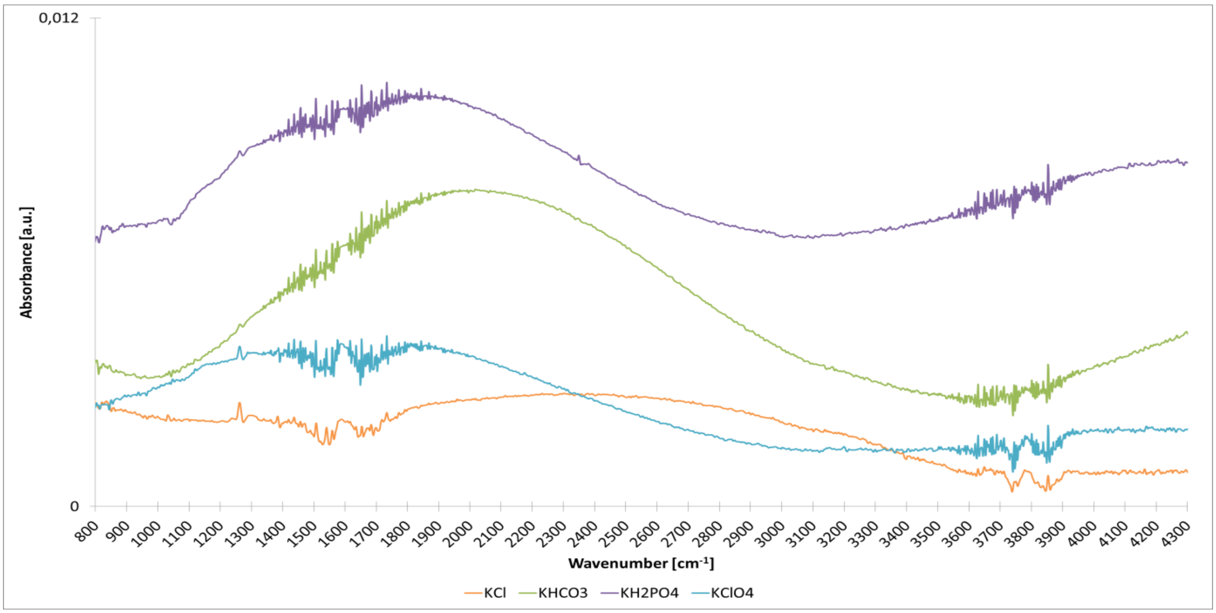

Figure 23: Reference ATR FTIR absorption spectra of the electrolytes without CO_2 with atmospheric compensation measured on the germanium ATR crystal with a 5 nm adhesive layer of titanium and a 10 nm layer of silver

What immediately can be seen from this figure is that, despite the application of atmospheric compensation on the spectra, all the spectra show disturbances in the two wavenumber regions, 1400-1900 cm^{-1} and 3600-3900 cm^{-1}, as in the spectra without atmospheric compensation. Furthermore, the base lines of the absorption spectra are curved instead of linear and in addition, no absorption peaks in the spectra of 0.1 M $KHCO_3$, 0.1 M K_2HPO_4 and 0.1 M $KClO_4$ are present below 1600 cm^{-1} in comparison to the spectra on the bare ATR germanium crystal. This is attributable to the fact that the titanium adhesive layer introduces a decrease in the IR absorption. As described in the section surface enhanced vibrational spectroscopy, silver in contrast shows enhancement of IR absorption. For this reason, the IR absorption spectra of the electrolytes are also measured on the germanium ATR crystal with only a 20 nm layer of silver to investigate the influence of the titanium adhesive layer.

Figure 24 shows the IR absorption spectra on the germanium ATR crystal with a 20 nm layer of silver with atmospheric compensation. Striking is, that now no disturbances are present in the 1400-1900 cm^{-1} and 3600-3900 cm^{-1} wavenumber regions and that they show almost a linear baseline in comparison to the spectra measured on the germanium ATR crystal with a 5 nm titanium adhesive and 10 nm silver layer.

The IR absorption spectrum of 0.1 M KCl matches the absorption spectrum on the bare germanium ATR crystal and shows no absorption and or desorption bands at wavenumbers below 1800 cm^{-1}. The IR absorption spectrum of 0.1 M $KHCO_3$ shows again the two absorption bands at 1360 and 1616 cm^{-1} corresponding to dissolved carbonate in the electrolyte as discussed in the previous section. Again, the IR absorption spectra of both 0.1 M KH_2PO_4 and 0.1 M $KClO_4$ show absorption bands at 990 cm^{-1} and 1100 cm^{-1}, and 1100 cm^{-1} respectively. In addition, a desorption band at a wavenumber around 1700 cm^{-1} is present. Comparing the broad absorption bands between 3300-3700 cm^{-1} with the bands on bare germanium it can be seen that the peak is shifted from around 3300 cm^{-1} on germanium to 3500 cm^{-1} on silver. From this observation, it can be concluded that water is stronger bonded to the silver than on germanium since a higher wavenumber corresponds to a higher binding energy. Together with the desorption band around 1700 cm^{-1} this shows that water is displaced from the silver surface in both electrolytes. The IR absorption peaks corresponding to the electrolytes measured on the germanium ATR crystal with a 20 nm silver layer are also summarized in Table 5.

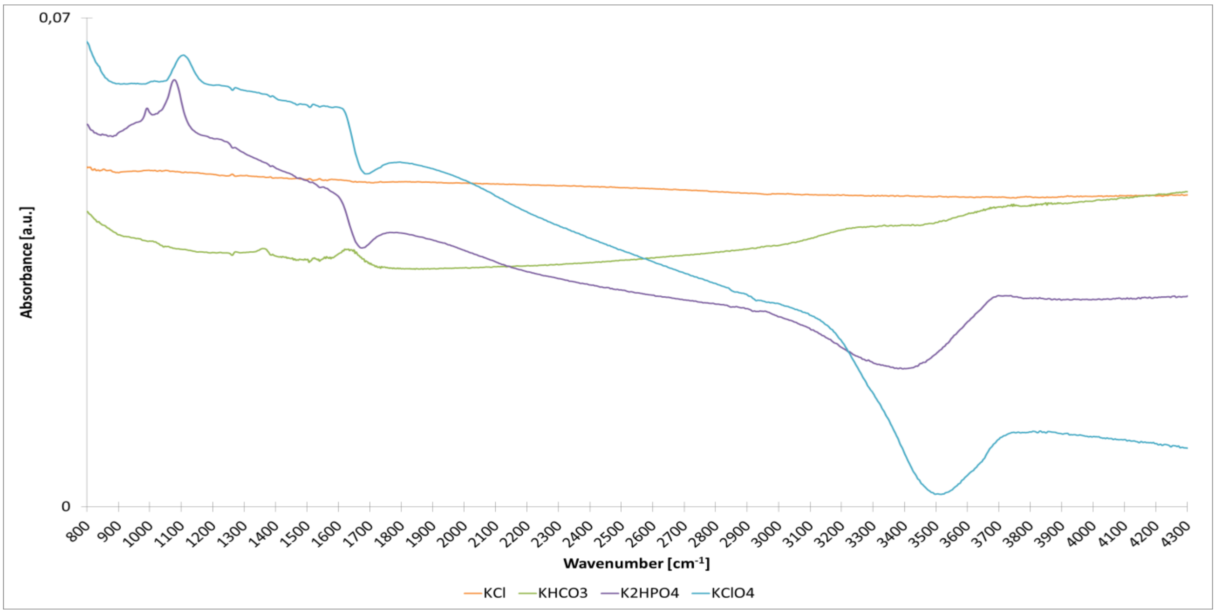

Figure 24: Reference ATR FTIR absorption spectra of the electrolytes without CO_2 with atmospheric compensation measured on the germanium ATR crystal with a 20 nm layer of silver

6.1.1.3. Summary

The ATR FTIR absorption spectra of air, water and the electrolytes without and saturated with CO_2 are measured on the bare germanium ATR crystal, the germanium ATR crystal with 5 nm titanium adhesive and 10 nm silver layer and the germanium ATR crystal with only a 20 nm layer of silver.

The spectra on the bare germanium ATR crystal showed large disturbances in the wavenumber regions between 1400-1900 cm^{-1} and 3600-3900 cm^{-1}. These disturbances are caused by traces of water and CO_2 from air inside the ATR accessory which can enter the ATR accessory when it is opened and insufficient flushing time of the ATR accessory with nitrogen. The atmospheric compensation tool in the software proved to be useful to remove these disturbances while maintaining the same shape of the absorption spectra.

The IR absorption spectra of the CO_2 saturated electrolytes are similar to each other and no useful information of these spectra could be obtained.

The thin adhesive layer of 5 nm titanium between the germanium ATR crystal and the 10 nm silver layer resulted in a decrease in IR absorption. The spectra showed despite the application of atmospheric compensation disturbances between 1400-1900 cm^{-1} and 3600-3900 cm^{-1} and a nonlinear baseline.

The IR absorption spectra of the electrolytes on the germanium ATR crystal with 20 nm of silver without the titanium adhesive layer do not show the disturbances in the regions between 1400-1900 cm^{-1} and 3600-3900 cm^{-1}. Furthermore, the baselines are linear, and the absorption and desorption peaks correspond to the peaks in the spectra measured on the bare germanium ATR crystal. The positions of the IR absorption and/or desorption peaks of the spectra of the different electrolytes and their assignments on the bare and with a 20 nm silver layer germanium ATR crystal are presented in Table 5.

6.1.2. CO_2 reduction reaction

The CO_2 reduction reaction measurements were performed at three different potentials, -1.4, -1.6 and -1.8 V vs Ag/AgCl, and in four different electrolytes, 0.1 M KCl, 0.1 M $KHCO_3$, 0.1 M K_2HPO_4 and 0.1 M $KClO_4$, in the spectroelectrochemical ATR-FTIR cell. All the ATR-FTIR spectra were taken at three-minute intervals for half an hour. First, the current density vs time characteristics of the different applied potentials in the different electrolytes are presented, followed by the measured pH values of the electrolytes after completing the reduction measurement. In order to compare the performed reduction measurements with literature, the potentials vs Ag/AgCl electrodes are converted for completeness to the potentials vs RHE electrode. Subsequently, the resulting ATR-FTIR absorption spectra during the CO_2 reduction experiments are presented and analysed. Finally, the influence of the face angle of the germanium ATR crystal on the IR absorption spectra is investigated.

6.1.2.1. Current density vs time characteristics

Previous research showed that below an applied voltage of -1.2 V vs Ag/AgCl no current flows through the spectroelectrochemical ATR cell and therefore the CO_2 reduction reaction does not occur [41]. To be sure that the CO_2 reduction reaction takes place, the minimum applied voltage to the cell in this study is -1.4 V vs Ag/AgCl. Figure 25 shows the current density vs time characteristics of the three applied voltages in the four different electrolytes. The blue, red and green line in the figure correspond to -1.4, -1.6 and -1. 8V vs Ag/AgCl respectively. As can be seen, it shows the same characteristics in all electrolytes. The more negative the applied potential, the more negative the current density. This is an indication that the CO_2 reduction reaction occurs and that reaction products are formed which is already proven by gas chromatography analysis in previous research.

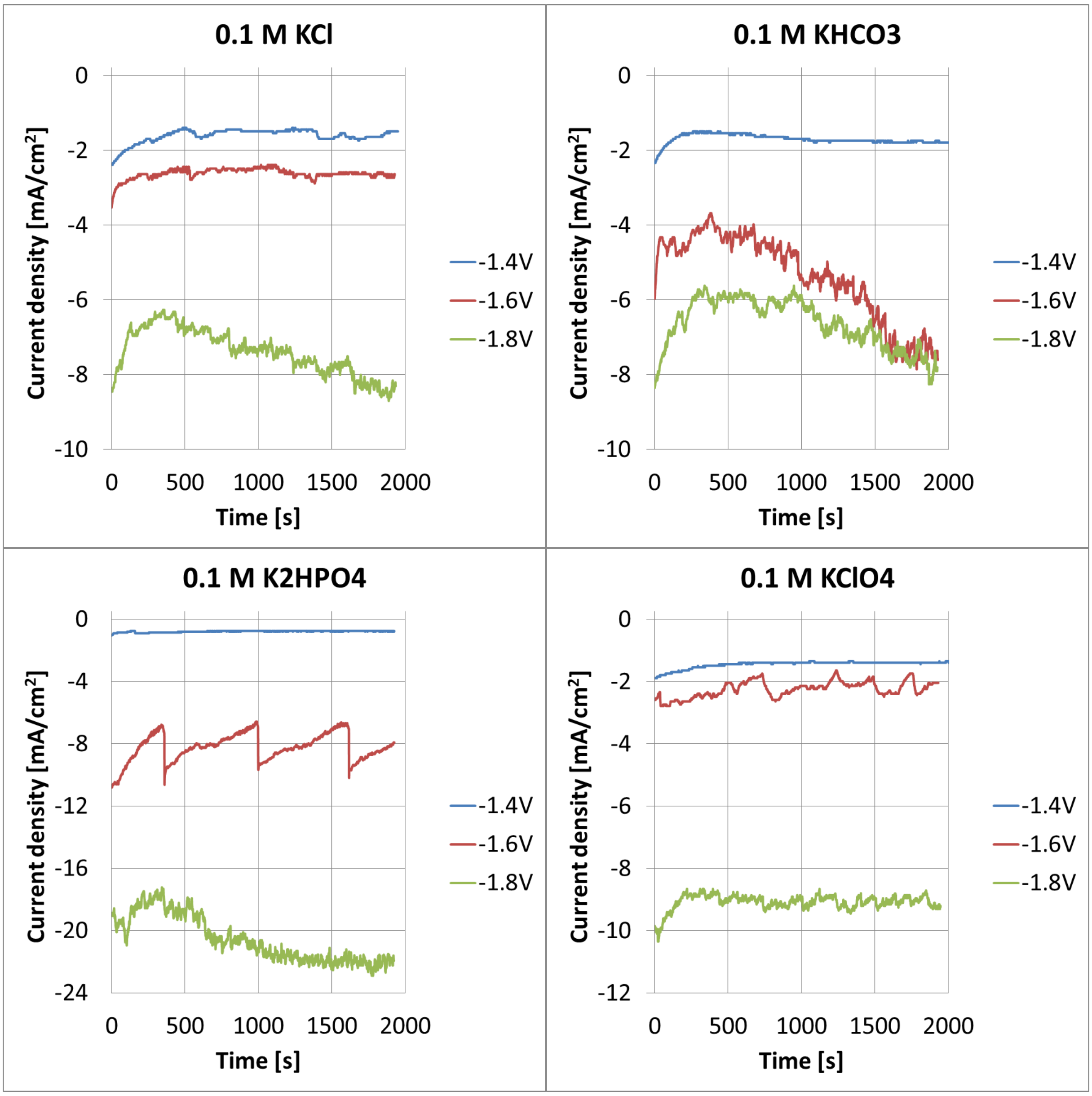

Figure 25: Current density vs time characteristics during the CO_2 reduction reaction in the different electrolytes at different applied potentials

6.1.2.2. pH values after the CO_2 reduction reaction

Since the CO_2 reduction reaction is dependent on the pH of the electrolyte, the pH is measured after the reduction experiments. The measured pH values after the reduction experiments at the different applied potentials in the four electrolytes are presented in Table 6.

Table 6: pH values of the different electrolytes measured after the CO_2 reduction reaction at different applied potentials

Potential vs Ag/AgCl	0.1 M KCl	0.1 M $KHCO_3$	0.1 M K_2HPO_4	0.1 M $KClO_4$
-1.4V	5.27	6.95	6.73	4.88
-1.6V	5.53	7.02	6.85	5.03
-1.8V	5.96	7.05	6.98	5.37

As can be seen from Table 6, a more negative applied potential results in an increase of the pH of the electrolytes. The increase in pH is greater in 0.1 M KCl and 0.1 M $KClO_4$ compared to 0.1 M $KHCO_3$ and 0.1 M K_2HPO_4. This is due to the fact that $KHCO_3$ and K_2HPO_4 are buffer electrolytes. The increase in pH is the result of that, at more negative potential, more protons are consumed in the reduction reaction and therefore the electrolytes get more basic.

In literature applied potentials in electrochemical reduction measurements are often given with respect to the reversible hydrogen electrode (RHE). For completeness, the applied potentials vs the Ag/AgCl electrode are converted to the potentials vs RHE. This is done by the Nernst equation given by Equation 2.

$$E_{RHE} = E_{Ag/AgCl} + 0{,}059 * pH + E^{\circ}_{Ag/AgCl} \qquad (2)$$

In this equation, $E_{Ag/AgCl}$ is the applied potential to the spectroelectrochemical cell, pH the pH of the electrolyte and $E^{\circ}_{Ag/AgCl}$ the standard potential at 25 °C in saturated KCl, which corresponds to 0.199 V respectively. Filling in pH values measured after the reduction experiments from Table 6 gives the potentials vs RHE. The resulting potentials vs RHE in the performed experiments are presented in Table 7.

Table 7: Conversion of the applied potentials vs Ag/AgCl reference electrode to the corresponding potentials vs RHE

Potential vs Ag/AgCl	0.1 M KCl	0.1 M $KHCO_3$	0.1 M K_2HPO_4	0.1 M $KClO_4$
-1.4V	-0.89V	-0.79V	-0.81V	-0.91V
-1.6V	-1.08V	-0.99V	-1.00V	-1.11V
-1.8V	-1.25V	-1.19V	-1.19V	-1.29V

It was not possible to measure the pH of the electrolytes during the experiments. The pH value of the electrolytes changes during the reduction reaction due to the consumption of protons. Since the potential of the RHE is dependent on the pH it also changes during the reaction. Therefore, it gives here only an indication of the potential vs RHE after the reaction and not the exact potential vs RHE. For this reason, potentials vs Ag/AgCl electrode are used in this study, since they are not dependent on the pH and are constant during the duration of the experiment.

6.1.2.3. ATR FT-IR absorption spectra

To determine the reaction intermediates and products formed during the CO_2 reduction reaction, ATR-FTIR absorption spectra were measured in different electrolytes, 0.1 M KCl, 0.1 M $KHCO_3$, 0.1 M K_2HPO_4 and 0.1 M $KClO_4$, at different applied potentials, -1.4, -1.6 and -1.8V, against a Ag/AgCl reference electrode. The measured ATR-FTIR absorption spectra are divided into low, 900-2400 cm^{-1}, and high, 3000-4000 cm^{-1} wavenumber regions in order to be able to determine the IR absorption bands more clearly. The resulting ATR-FTIR spectra measured after 31 minutes are presented in Figure 26 - Figure 29.

The in the ATR-FTIR spectra present IR absorption bands, corresponding to the CO_2 reduction reaction intermediates and products, are assigned using values found in literature on the CO_2 reduction reaction and reactions of other small organic molecules as introduced in section 2.5 and presented in Table 3 and Table 4. The in this study found IR absorption bands are summarized in Table 8.

When looking at the measured ATR-FTR spectra in the different electrolytes and applied potentials the following trends can be observed. The IR absorption bands related to the electrolytes measured on germanium are not present in the spectra taken during the CO_2 reduction reaction measurements. In addition, all the spectra measured during the CO_2 reduction experiments show a doublet absorption band at a wavenumber of 2350 cm^{-1}. This absorption band is not present in the ATR-FTIR spectra measured with the pure electrolytes without an applied potential. This absorption band is also present in the measured reference ATR-FTIR absorption spectra of the with CO_2 saturated electrolytes on the bare germanium ATR crystal without an applied potential as presented in Figure 21. Therefore, this band is assigned to dissolved CO_2 in the electrolyte. This corresponds with wavenumbers found in literature as summarized in Table 3 and Table 4.

Furthermore, it is observed that the broad absorption bands present at wavenumbers around 3300 cm^{-1} in the measured reference IR absorption spectra of the electrolytes on germanium shift to a higher wavenumber around 3450 cm^{-1} in the measurements of the reference IR absorption spectra of the electrolytes on silver and during the CO_2 reduction reaction measurements. An increase in wavenumber represents an increase in binding energy. At this wavenumber O-H bending vibrations of water occur. When water molecules are bound to a surface, the O-H bending energy is lower than in free water molecules and occurs at a lower wavenumber. The difference in the wavenumber of the O-H bending vibration measured on germanium (reference electrolyte spectra) and silver (CO_2 reduction reaction spectra) represents thus a different binding energy with the germanium and silver surface. Since the O-H bending vibration occurs at a lower wavenumber on germanium it follows that a water molecule is bounded more strongly on germanium than silver.

An increase in applied potential shows for the high wavenumber region in all electrolytes an increase in absorption bands. Striking is here, that a second IR absorption band comes up at a wavenumber of 3100 cm^{-1}. This IR absorption band is smaller and less broad than the one that occurs at 3450 cm^{-1}. As shown in Table 4, O-H bending vibrations occur in the 3000-3600 cm^{-1} range. Above it is discussed that surface bound water molecules occur at a lower wavenumber since the O-H bending energy is lower than in a free water molecule. Due to this, a distinction is made between free and surface bound water molecules during the CO_2 reduction reaction. The small IR absorption bands at a wavenumber around 3100 cm^{-1} and the large and broad IR absorption band at around 3450 cm^{-1} correspond to water molecules bonded to the silver surface and free water molecules respectively. From the reference IR absorption measurements, it is not clear if the observed bands on germanium, presented in Figure 22, and silver, presented in Figure 24, correspond to surface bound or free water molecules. In the lower wavenumber regions, only an increase in IR absorption bands can be found in the 0.1 M $KHCO_3$ electrolyte. In Figure 27 one can clearly see the increase of the IR absorption band at wavenumbers around 1411, 1640, and 2000 cm^{-1}. The assignments of the absorption bands are discussed in the next paragraph.

In the low wavenumber region, 900-2400 cm^{-1}, next to the doublet IR absorption band, at a wavenumber of 2350 cm^{-1} corresponding to dissolved CO_2 in the electrolytes, two other distinct IR absorption bands are present in all measured IR absorption spectra during the CO_2 reduction reaction in different electrolytes and applied potentials. The IR absorption band at a wavenumber around 1650 cm^{-1} and 2000 cm^{-1}. The first one is negative, whereas the latter one is positive. A negative band indicates that a vibration of a bond is not present anymore with respect to the background measurement. A positive band indicates a new vibration of a bond since this vibration was not present in the background measurement before. Based on the investigated studies found in literature, see section 2.5, these absorption bands correspond to O-H deformation of surface bound water and linear to the surface bonded CO respectively. Since the IR absorption band of water decreases and the IR absorption band of CO increases it indicates that water molecules at the surface are displaced by CO molecules.

In the spectra measured in 0.1 M KCl, 0.1 M $KHCO_3$ and 0.1 M K_2HPO_4 at an applied voltage of -1.4 V vs Ag/AgCl a second small IR absorption band is present at a slightly higher wavenumber, 2040 cm^{-1}, than the IR absorption band of linear bonded CO which is present at 2000 cm^{-1}. Based on values found in the literature this IR absorption band correspond to surface bound hydrogen. At more negative applied voltages, this IR absorption band disappears again. The size of the IR absorption band and the disappearance at more negative potentials indicate that adsorbed hydrogen is readily released from the surface.

The combination of the present IR absorption bands below a wavenumber of 1650 cm^{-1} in the measured IR absorption spectra during the CO_2 reduction reaction indicate the presence of carbonaceous species. As can be seen in Figure 26 - Figure 29, IR absorption bands are present at different wavenumbers in the measurements performed in the different electrolytes. The ATR-FTIR absorption spectra measured at an applied potential of -1.8 V vs Ag/AgCl in 0.1 M KCl and 0.1 M $KClO_4$ show three IR absorption bands at wavenumbers around 1290, 1410 and 1620 cm^{-1}. The combination of these three IR absorption bands can correspond to the OH deformation, symmetric and asymmetric CO_3^- stretch of surface bound bicarbonate respectively, however also to the symmetric and asymmetric O stretch of bidendate and dissolved carbonate as indicated in Table 4.

In the measured ATR-FTIR spectra in 0.1 M $KHCO_3$ the IR absorption band around 1620 cm^{-1} does not occur. Furthermore, the other two IR absorption bands are present at lower wavenumbers. Around 1280 and 1410 cm^{-1}. The combination of these two IR absorption bands can correspond in this case to the symmetric and asymmetric OCO stretch of monodendate carbonate but also only to symmetric O stretch of bidendate and dissolved carbonate respectively as can be seen in Table 8.

In contrast to the spectra measured in 0.1 M KCl, 0.1 M $KClO_4$ and 0.1 M $KHCO_3$, the spectra measured in 0.1 M K_2HPO_4 show only one IR absorption band around 1315 cm^{-1}. This absorption band is in literature assigned to the vibrational mode of bridge bonded formate. This means the formate is bonded via the oxygen atoms to the silver surface. This is an unlikely intermediate since it can only form formic acid as a reaction product and not CO which clearly present as can be seen due the positive absorption band around 2000 cm^{-1}. As the vibrational energy of the with the C to the silver surface bonded COOH is similar to the vibrational energy of formate it is expected that this molecule is present.

The analysis of the measured IR absorption spectra showed that the present IR absorption bands in the lower wavenumber region can be assigned to carbonate species present in the ATR cell during the CO_2 reduction reaction. Due to the overlap of dissolved and surface bound species it was not possible to determine the reaction intermediates with the performed experiments but only presence of spectator molecules. The exact locations of all the observed absorption peaks in the measured spectra are given in Table 8. Again, a minus sign in front of a wavenumber indicates a negative absorption band which corresponds to the displacement of a molecule during the performed experiment.

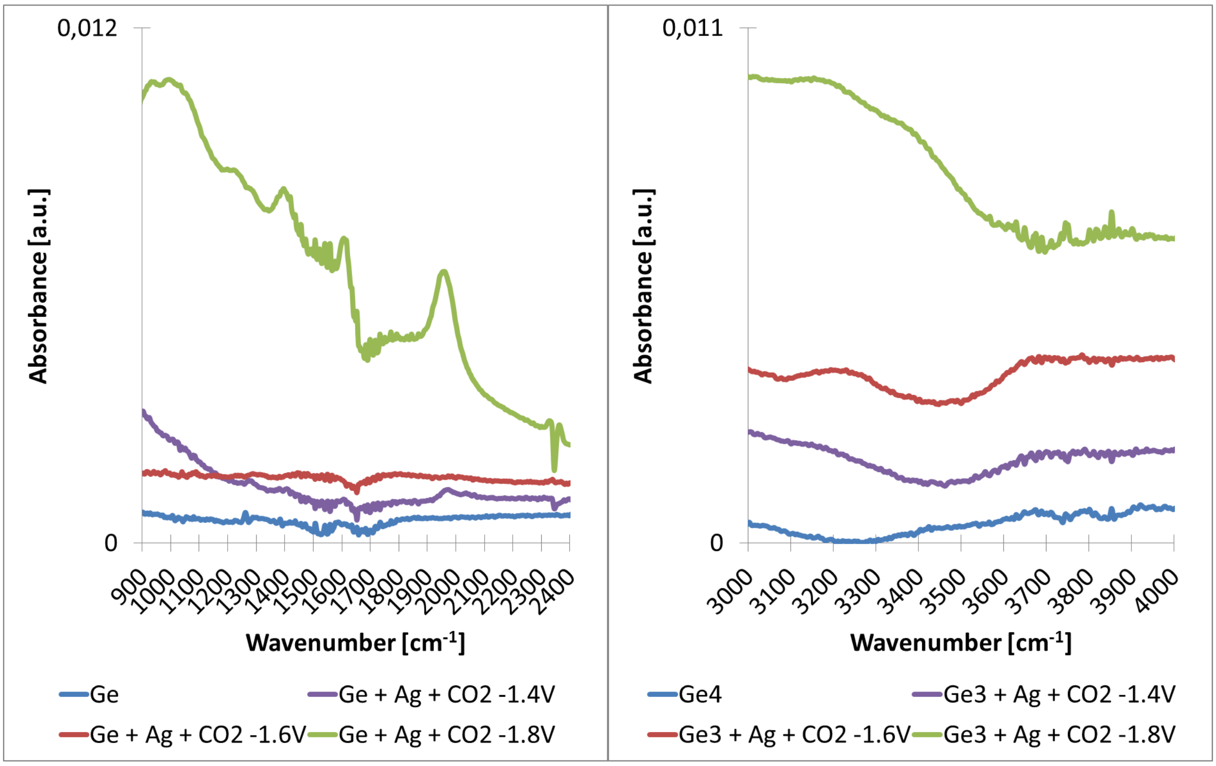

Figure 26: Measured ATR FTIR absorption spectra of the CO_2 reduction reaction in 0.1 M KCl at different applied potentials divided into the low and high wavenumber region

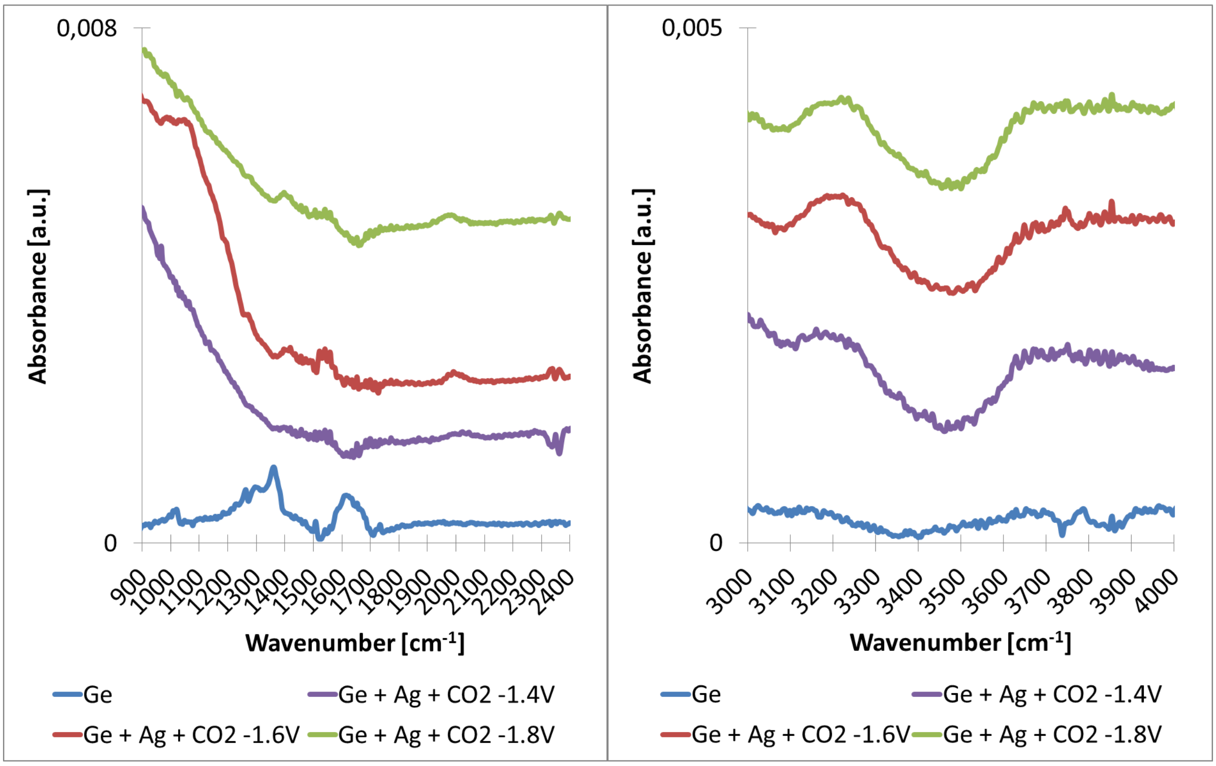

Figure 27: Measured ATR FTIR absorption spectra of the CO_2 reduction reaction in 0.1 M $KHCO_3$ at different applied potentials divided into the low and high wavenumber region

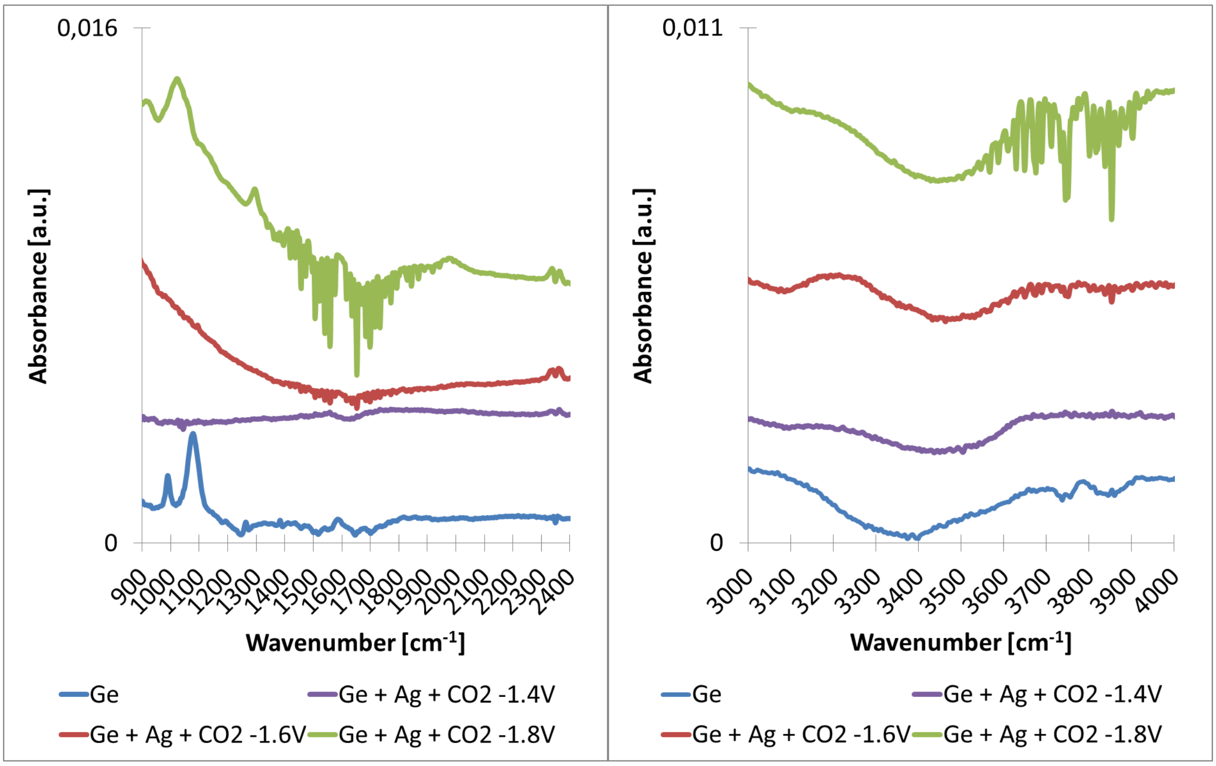

Figure 28: Measured ATR FTIR absorption spectra of the CO_2 reduction reaction in 0.1 M K_2HPO_4 at different applied potentials divided into the low and high wavenumber region

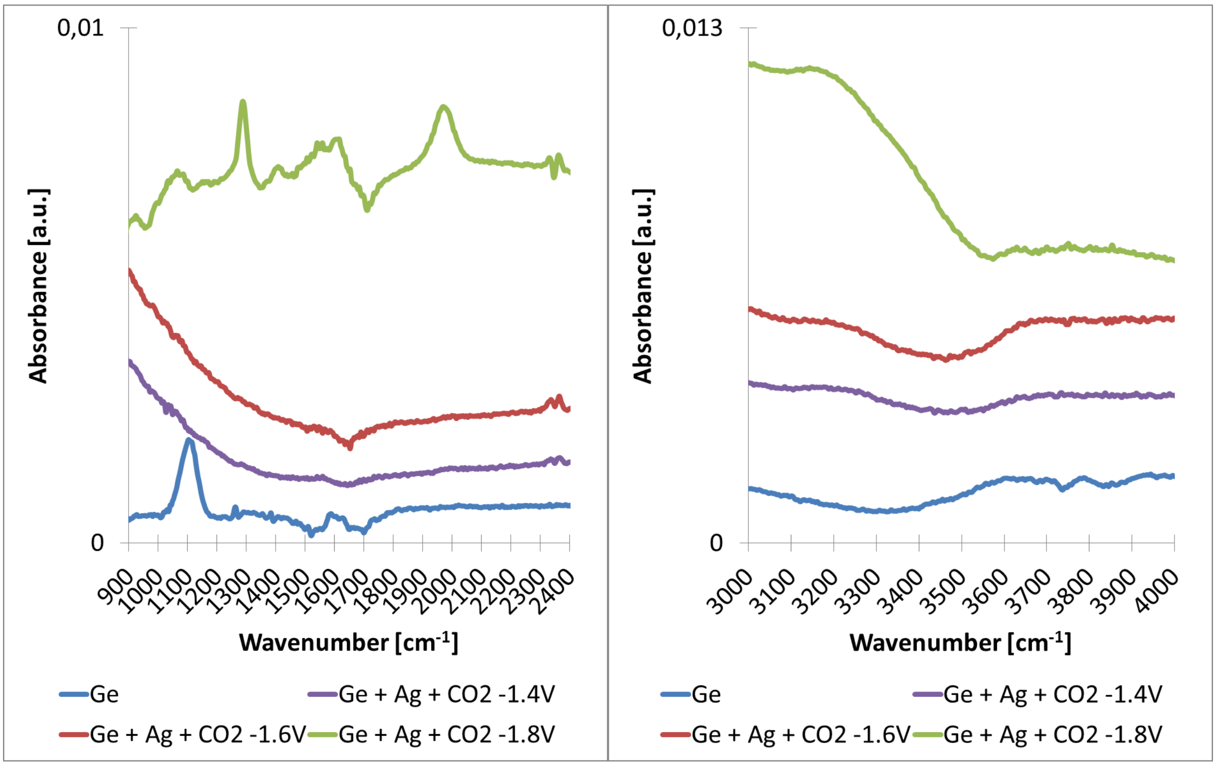

Figure 29: Measured ATR FTIR absorption spectra of the CO_2 reduction reaction in 0.1 M $KClO_4$ at different applied potentials divided into the low and high wavenumber region

Table 8: Assignments of the observed IR absorption bands present in the ATR-FTIR spectra measured after 31 minutes at different applied potentials against a Ag/AgCl reference electrode during the CO_2 reduction

Electrolyte	**Absorption bands [cm^{-1}]**			**Assignment**
	-1.4 V	**-1.6 V**	**-1.8 V**	
0.1 M KCl	1275	1293	1292	OH deformation or sym O stretch bidendate carbonate
	1413		1403	Sym $CO3^-$ stretch or dissolved carbonate
			1612	Asym $CO3^-$ stretch of bound bicarbonate or asym O stretch bidendate carbonate
		-1652	-1671	Displacement of interfacial H_2O
	1975	1988	1941	Linear bonded CO
	2040			Adsorbed H_2
	2345	2350	2343	Dissolved CO_2
		-3090		Displacement of interfacial H_2O
	-3460	-3440		Displacement of free H_2O
0.1 M $KHCO_3$		1280		Asym OCO stretch
		1411	1411	Sym OCO stretch of monodendate carbonate or dissolved carbonate
	-1620		-1660	Displacement of interfacial H_2O
		2000	1982	Linear bonded CO
	2030		2040	Adsorbed H_2
	2350	2348	2343	Dissolved CO_2
	-3100	-3081	-3087	Displacement of interfacial H_2O
	-3488	-3485	-3478	Displacement of free H_2O
0.1 M K_2HPO_4	1328		1300	COOH
	-1630		-1650	Displacement of interfacial H_2O
			1990	Linear bonded CO
	2026			Adsorbed H_2
	2348	2348	2348	Dissolved CO_2
	-3095	-3088	-3098	Displacement of interfacial H_2O
	-3460	-3475	-3448	Displacement of free H_2O
0.1 M $KClO_4$	1293		1286	OH deformation or sym O stretch bidendate carbonate
			1413	Sym $CO3^-$ stretch or dissolved carbonate
			1621	Asym $CO3^-$ stretch of bound bicarbonate or asym O stretch bidendate carbonate
	-1646	-1652	-1700	Displacement of interfacial H_2O
	1990		1980	Linear bonded CO
	2346	2348	2344	Dissolved CO_2
	-3088	-3097	-3091	Displacement of interfacial H_2O
	-3470	-3460		Displacement of free H_2O

6.1.2.4. Effect of the face angle of the germanium ATR crystal

In this section, the influence of the face angle of the germanium ATR crystal on the measured IR absorption spectra during the CO_2 reduction reaction is investigated. As introduced in the literature review, ATR-FTIR spectroscopy is based on the evanescent wave generated when the IR beam is reflected at the interface of the germanium ATR crystal with the sample. In this study, the sample is the 20 nm silver electrode. A schematic representation of an evanescent wave entering a sample is given in Figure 30. The penetration depth of the evanescent wave can be calculated with Equation 3:

$$d_p = \frac{\lambda}{2*\pi*\sqrt{n_1^2*sin^2(\theta_e)-n_2^2}} \qquad (3)$$

In this equation, λ is the wavelength of the IR beam, n_1 the refractive index of the ATR crystal, in this case germanium, n_2 the refractive index of the sample, in this case silver, and θ_e the effective angle of irradiance of the IR beam on the interface between the germanium ATR crystal and the sample. The effective angle is a function of the face angle, θ_f, and the refractive index, n_1, of the ATR crystal and the set angle of the ATR accessory, θ_s and is given by Equation 4.

$$\theta_e = \theta_f + sin^{-1}\left(\sin\left(\theta_s - \theta_f\right)/n_1\right) \qquad (4)$$

The set angle of the ATR accessory represents the angle of irradiance of the IR beam onto the ATR crystal. It can be adjusted between 30 and 80° by turning the wheel on the ATR accessory, as can be seen in Figure 17, which changes the position of the mirrors inside the ATR accessory and redirect the IR beam.

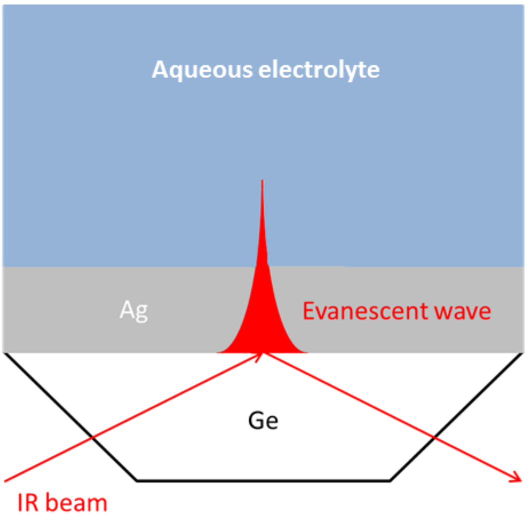

Figure 30: Schematic representation of the evanescent wave entering the sample

In this study two germanium ATR crystals with face angles of 45 and 60° are used. The refractive index of germanium is almost wavelength independent and has a value of 4 [44]. Using Equation 4, the effective angles of the IR beam on the germanium-silver interface at the two germanium ATR crystals with different face angle can be calculated. The calculated effective angles are presented in Table 9.

Table 9: Calculated effective angles for the germanium ATR crystals with different face angles corresponding to the set angle on the ATR accessory

Θ_s [°]	Θ_e ($\Theta_f = 45°$) [°]	Θ_e ($\Theta_f = 60°$) [°]
30	41.25	52.5
40	43.75	55.0
50	46.25	57.5
60	48.45	60.5
70	51.25	62.5
80	53.75	65.5

The refractive index of silver is in contrast to that of germanium dependent on the IR wavelength. Since in ATR-FTIR spectroscopy a broad wavenumber region 800-4300 cm^{-1}, which corresponds to wavelengths of 12400-2254 nm, is used, a single refractive index of silver at one specific wavelength is not sufficient enough to determine the penetration depth of the evanescent wave. In literature, experimental data for the refractive index of silver in this wavelength region was found. Barbar and Weaver investigated the refractive index of bulk single crystal silver [45]. The resulting refractive indexes of silver corresponding to the wavelength are presented in Table 10.

Table 10: Experimental determined wavelength depended refractive indexes of silver

Wavenumber [cm^{-1}]	Wavelength [nm]	Refractive index Ag [45]
4436,557	2254	0.272
4032,258	2480	0.326
3629,764	2755	0.397
3225,806	3100	0.496
2823,264	3542	0.639
2419,550	4133	0.857
2016,536	4959	1.228
1613,163	6199	1.851
1209,775	8266	3.227
806,452	12400	5.079

With the calculated effective angles, Θ_e, and the experimental determined refractive indexes of silver, (n_2), the penetration depth of the evanescent wave on the germanium ATR crystals with a face angle, Θ_f, of 45° and 60° are calculated using Equation 3. The penetration depth of the evanescent wave is plotted against the wavenumber for both germanium ATR crystals. Figure 31 a) and b) show the results for the germanium ATR crystal with a face angle of 45 and 60° respectively. It can be seen that for the germanium ATR crystal with a face angle of 45° for the whole range of the set angles, 30-80°, on the ATR accessory below a wavenumber of 1300 cm^{-1} the penetration depth of the evanescent wave is not positive, greater than 0 nm. At the germanium crystal with a face angle of 60° this is only the case when the set angle of the ATR accessory is set to 30°. This is caused by the fact that the term under the square root in Equation 3 has a negative value. Therefore, information given by the absorption spectrum below a wavenumber of 1300 cm^{-1} cannot be used to determine present bonds between atoms in molecules for these two cases.

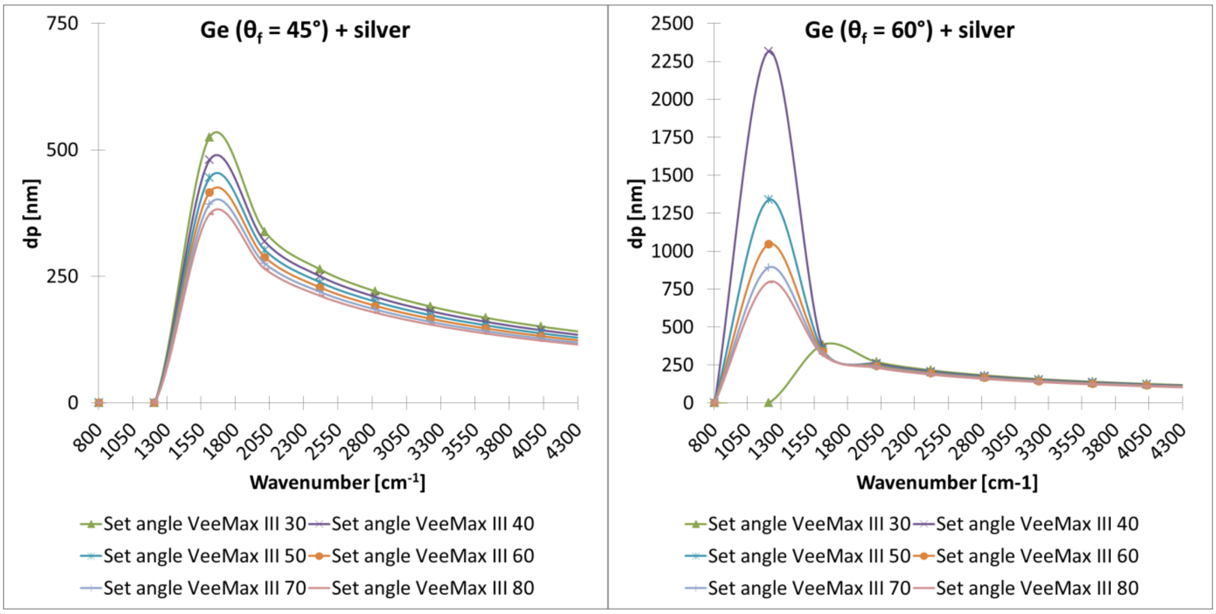

Figure 31: Calculated penetration depths of the evanescent wave on the germanium ATR crystal with a silver sample with a face angle of 45° a) and b) with a face angle of 60° b)

For the germanium ATR crystal with a face angle of 60° and a set angle on the ATR accessory from 40° upwards, the penetration depth of the evanescent wave is larger than 0 nm over the entire wavenumber range of 800-4300 cm^{-1}.

In the positive penetration depth region, the curves of the penetration depths show the same behaviour for the germanium ATR crystal with a face angle of 45 and 60° respectively. At lower wavenumbers, the penetration depth is larger than at higher wavenumbers. The maximum penetration depth of 525 nm on the germanium ATR crystal with a face angle of 45° is reached with a set angle of the ATR accessory of 30° at a wavenumber of 1613 cm^{-1}. In comparison, the maximum penetration depth is 2316 nm on the germanium ATR crystal with a face angle of 60° at a set angle of 40° on the ATR accessory at a wavenumber of 1209 cm^{-1}. In both cases the penetration depth decreases first strongly with an increase in wavenumber to 1900 cm^{-1}. From then on, decreasing only gradually with increasing wavenumber to 4300 cm^{-1}.

As described earlier, the IR absorption spectra during the CO_2 reduction reaction are measured on the germanium ATR crystal with a face angle of 60° and a 20 nm layer of silver. As can be seen in Figure 31 b), the calculated penetration depth over the whole wavenumber range, 800-4300 cm^{-1}, is by far larger than the 20 nm silver layer on top of the germanium ATR crystal so that it is ensured that the evanescent wave can probe molecules on the silver electrolyte surface.

In order to investigate the effect of the different face angles of the germanium ATR crystal on the ATR-FTIR absorption spectra during the CO_2 reduction experiment, the experiment with the 0.1 M $KHCO_3$ electrolyte and an applied potential of -1.6 V vs Ag/AgCl electrode is repeated with the germanium ATR crystal with a face angle of 45°. The conditions of the experiments are kept the same using a set angle on the ATR accessory of 60° and the procedure as described earlier.

As introduced above, the penetration depth of the evanescent wave is dependent on the effective angle, which again is dependent on the face angle of the ATR crystal. In Figure 32 a), the penetration depth of the evanescent wave is plotted against the wavenumber for the two face angles of 45° and 60° of the germanium ATR crystal at a fixed set angle on the ATR accessory of 60°. As already mentioned, the curves of the penetration depth on the germanium ATR crystals with different face angles differ from each other. Where the penetration depth of the evanescent wave on the germanium ATR crystal with a face angle of 60° is positive over the entire wavenumber range with a way larger depth at the lower wavenumbers, the penetration depth of the evanescent wave on the germanium ATR crystal with a face angle of 45° is only calculable from 1300 cm^{-1} onwards and is lower than on the germanium ATR crystal with a face angle of 60° until a wavenumber of 1600 cm^{-1}. From 1600 cm^{-1} on, the penetration depth at the germanium crystal with a face angle of 45° is larger than that on the germanium ATR crystal with a face angle of 60°.

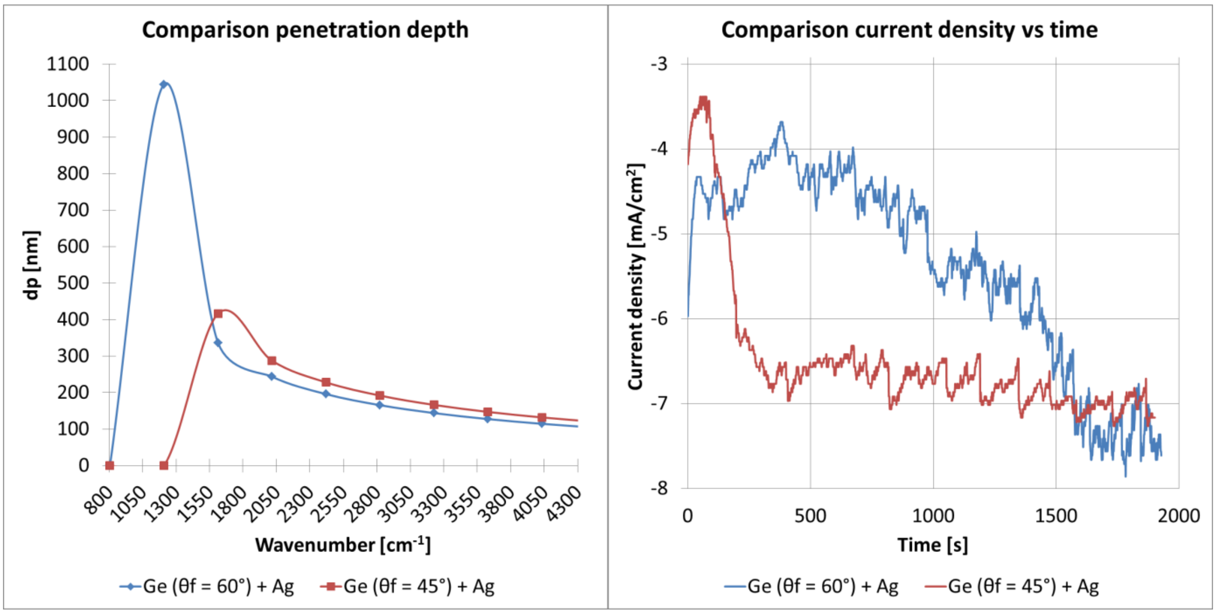

Figure 32: Comparison of the penetration depth of the evanescent wave a) and the current density vs time characteristics during the CO_2 reduction measurement b) on the germanium ATR crystal with a 20 nm silver layer with a face angle of 45° and 60°

Since only a thin layer, 20 nm, of silver on top of the germanium ATR crystal is used in this study, the difference of the penetration depth reaches into the electrolyte so that not only molecules on the silver surface are probed but also molecules present within the reach of the penetration depth in the electrolyte. It is expected that, the larger the penetration depth of the evanescent wave the more IR signal is absorbed. The IR absorption spectra during the CO_2 reduction reaction are always measured against the spectra of the with CO_2 saturated electrolyte at open circuit conditions. In comparison to molecules present in the bulk electrolyte, the amount of intermediate reaction products on the silver surface and reaction products in the electrolyte are very small resulting in only small absorption peaks.

So, regarding to the gained information on the different penetration depths of the evanescent wave on the two germanium crystals with face angles of 45 and 60° respectively, the part of the absorption spectrum on the germanium ATR crystal with a face angle of 45° below 1300 cm^{-1} gives false information on absorption bands and therefore, should not be taken into consideration during the analysis of the spectrum. Furthermore, it is expected that due to the lower penetration depth of the evanescent wave between 1300 and 1600 cm^{-1} the absorption bands in this region of the IR absorption spectrum are larger compared to the IR absorption spectrum on the germanium ATR crystal with a face angle of 60°. At higher wavenumbers, it expected to be the other way around since the penetration depth of the evanescent wave is larger.

To check if the electrical conditions in the experiments are the same, the current density vs time characteristics of the CO_2 reduction measurements on the germanium ATR crystal with a face angle of 45 and 60° are compared. Figure 32 b) shows the comparison of the current density vs time characteristics of the CO_2 reduction measurements on the different germanium ATR crystals. As can be seen, the curves differ from each other. However, they show the same characteristics. First, the current density decreases after reaching the applied potential, then increases again and finally reaching a steady level. The onset current density of the measurement on the germanium ATR crystal with a face angle of 45° is about 2 mA/cm^2 lower, -4.2 mA/cm^2 vs -6 mA/cm^2, than the onset current density during the measurement on the germanium ATR crystal with a face angle of 60°. The current density then decreases to -3.4 and -3.7 mA/cm^2 for 45° and 60° after 1 and 6 minutes respectively. The current density then increases fast to a value around -6.5 mA/cm^2 during the measurement the germanium ATR crystal with a face angle of 45° where it fluctuates over time between -6.4 and -7.2 mA/cm^2. During the measurement on the germanium ATR crystal with a face angle of 60° the current density increases only slowly over time until -7 mA/cm^2 and then fluctuates between -6.8 and -7.8 mA/cm^2. So only after about 29 minutes the current density vs time characteristics of both measurements are similar. For this reason, the IR absorption spectra taken after 31 minutes are used for the comparison of the experiments on the germanium ATR with different face angles.

Figure 33 shows the measured IR absorption spectra after 31 minutes of the experiments performed with the germanium ATR crystal with a face angle of 60° and 45° respectively. As can be seen, despite that the penetration depth of the evanescent wave could not be calculated for wavenumbers below 1300 cm^{-1}, infrared absorption occurs below 1300 cm^{-1} in the measurement on the germanium ATR crystal with a face angle of 45°. Since the penetration depth of the evanescent wave could not be calculated it is not clear if an evanescent wave below 1300 cm^{-1} is present and that the IR absorption is the due to the evanescent wave or due to another mechanism. For this reason, the IR absorption and desorption bands below 1300 cm^{-1} are not taken into consideration in the comparison with the spectrum of the measurement performed with the germanium ATR crystal with a face angle of 60°.

When looking at the IR absorption spectrum obtained from the experiment on the germanium ATR crystal with a face angle of 60°, an interesting thing can be observed regarding to the base line. As can be seen, the baseline is almost horizontal between 1300 to 4300 cm^{-1} whereas from 800 cm^{-1} to 1300 cm^{-1} it has a negative slope. Referring back at the penetration depth curve of the evanescent wave it can be seen that in this region the penetration depth is way larger than from 1300 cm^{-1} which results in stronger IR absorption and causes the baseline to shift to higher absorption levels.

Comparison of the two IR absorption spectra shows indeed the expected behaviour. At lower wavenumbers, 1300-1800 cm^{-1}, the IR absorption spectrum obtained from the experiment performed with the germanium ATR crystal with a face angle of 45° shows larger IR absorption and or desorption bands in comparison to the spectrum obtained from the experiment performed with the germanium ATR crystal with a face angle of 60°. At wavenumbers, higher than 2800 cm^{-1} it is the other way around as can be seen by the more distinct OH desorption band in the spectrum measured on the germanium ATR crystal with a face angle of 60°. Furthermore, the present IR absorption and desorption bands at 1417, 2000 and 2346 cm^{-1} are consistent in both spectra and therefore, the peaks in the spectrum obtained from the experiment with the germanium ATR crystal with a face angle of 45° are assigned to the same molecular vibrations. For the results of the assignments it is referred to Table 8 in the previous section. At a wavenumber of 1670 cm^{-1} a desorption band is observed. This desorption band is consistent with the results of the ATR-FTIR spectrum at higher applied potential of -1.8 V vs Ag/AgCl and in the spectra measures at -1.6 V vs Ag/AgCl in the other electrolytes. This desorption band corresponds to water that is replaced at the silver surface.

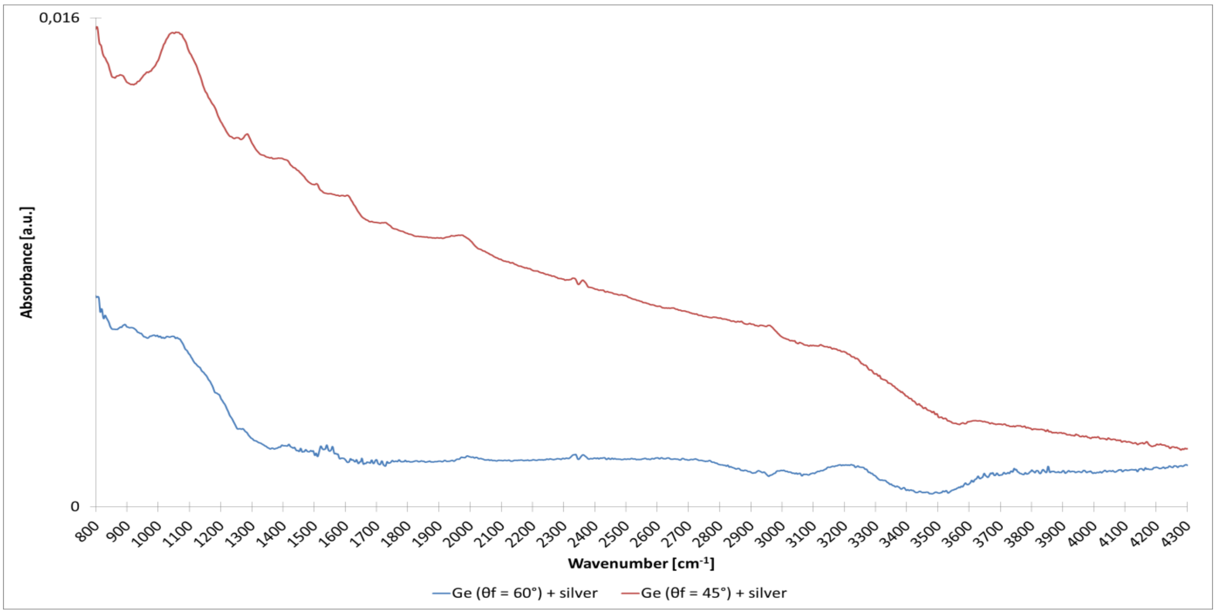

Figure 33: Comparison of the ATR FTIR absorption spectra of the CO_2 reduction reaction on the germanium ATR crystals with a face angle of 45° and 60° and a 20 nm silver layer

6.1.3. Summary

Reference ATR-FTIR absorption spectra in 0.1 M KCl, 0.1 M $KHCO_3$, 0.1 M K_2HPO_4 and 0.1 M $KClO_4$ are measured on a bare germanium ATR crystal to determine IR absorption bands related to the electrolytes. The reference ATR-FTIR absorption spectra are also measured on the germanium ATR crystal with a thin layer of silver to investigate the effect of the thin silver layer on the IR absorption spectra of the electrolytes. The addition of a titanium adhesive layer showed a decrease in IR absorption. Without the titanium adhesive layer, the measured IR absorption spectra correspond to each other indicating that the silver layer does not influence the IR absorption. In the measured IR absorption spectrum of 0.1 M KCl no IR absorption band is present. The spectra of 0.1 M $KHCO_3$ show two broad absorption peaks at around 1360 and 1620 cm^{-1}. These correspond to dissolved carbonate in the electrolyte. In the IR absorption spectra of 0.1 M K_2HPO_4 two IR absorption bands are present around 990 and 1100 cm^{-1}. These absorption bands can be assigned to asymmetric and symmetric stretch vibrations of P-O in K_2HPO_4. The absorption peaks present in the spectra measured in 0.1 M $KClO_4$ at a wavenumber of 1100 cm^{-1} correspond to the asymmetric Cl-O stretching bands.

The pH of the electrolytes is measured after the CO_2 reduction reaction experiments. A more negative applied potential results in an increase in pH of the electrolytes. The increase in pH is greater in 0.1 M KCl and 0.1 M $KClO_4$ compared to 0.1 M $KHCO_3$ and 0.1 M K_2HPO_4. This is due to the fact that $KHCO_3$ and K_2HPO_4 are buffer electrolytes. The increase in pH is the result of that at more negative potential more protons are consumed in the reduction reaction and therefore the electrolytes get more basic.

The current density vs time characteristics of the CO_2 reduction reaction showed the expected behaviour in all the electrolytes. The more negative the applied potential, the more negative the current density. This is an indication that the CO_2 reduction reaction occurs and that reaction products are formed.

The measured IR absorption spectra, with a 20 nm layer of silver, during the CO_2 reduction reaction, in all electrolytes and at different applied potentials, show a sharp, small and broad, strong negative IR absorption band around 1650 and 3450 cm^{-1} and a positive IR absorption band around 2000 cm^{-1} corresponding to the OH deformation of water and linear to the silver surface bonded CO respectively. This indicates that CO is produced during the CO_2 reduction reaction and that water is replaced by CO on the silver surface. Spectator molecules are identified by combination of IR absorption bands below 1650 cm^{-1}. In 0.1 M KCl and 0.1 M $KClO_4$ bicarbonate is identified as possible spectator molecule whereas in 0.1 M $KHCO_3$ carbonate and in 0.1 M K_2HPO_4 formate are identified as possible spectator molecules respectively.

The penetration depths of the evanescent waves generated at germanium ATR crystals with different face angles are calculated for different effective angles. The depth profiles differ mainly in the low wavenumber region. However, they are positive and larger than the 20 nm silver layer over the entire wavenumber region under the conditions in which the CO_2 reduction measurements are performed so that the observed IR absorption bands are detected correctly due to attenuation of the IR beam.

Comparative IR absorption measurements of the CO_2 reduction reaction with a different face angle of the germanium ATR crystal are performed. Due to the different depth profiles, the IR absorption spectrum obtained from the experiment performed with the germanium ATR crystal with a face angle of 45° shows larger absorption and or desorption bands in comparison to the spectrum obtained from the experiment performed with the germanium ATR crystal with a face angle of 60° at lower wavenumbers, 1300-1800 cm^{-1} since the penetration depth of the evanescent wave is smaller. At wavenumbers, higher than 2800 cm^{-1} it is the other way around.

6.2. Thin layer flow cell configuration

The results obtained from the experiments performed with the thin layer flow cell are presented in this section. First, the flowrate of the pump and then the electrochemical performance of the thin layer flow cell are determined. Before performing the IR absorption measurements, it is necessary that the set angle of the ATR accessory at which the IR signal is highest is investigated in order to obtain the best possible IR absorption spectra. As in the measurements performed with the ATR cell, first, the reference spectra of the used pure and with CO_2 saturated electrolytes are determined. Finally, the results of the CO_2 reduction reaction experiments are introduced and discussed.

6.2.1. Calibration of the pump

As described earlier in section 5.1.2, the electrolyte is pushed through the thin layer flow cell by a variable speed Cole-Parmer Masterflex L/S peristaltic pump. The flowrate of the electrolyte is defined by the rpm setting of the pump. The flowrate is determined by measuring the amount of water pumped within one minute at a certain adjusted rpm on the pump. This is done for three different rpm. The results are presented in Table 11.

Table 11: Measured volumes of water after 1 minute at a set rpm on the Cole-Parmer Masterflex L/S peristaltic pump

Set point [rpm]	Amount of water [mL] after 1 min
30	1.8
50	3.1
70	4.1

Averaging the measured volumes corresponding to the rpm results in that one rpm corresponds to 0.06 mL/min. As mentioned in in section 5.3.2.5 the influence of the flow rate of the electrolyte on the IR absorption spectrum during the CO_2 reduction reaction is investigated. This is done by performing the measurements at flow rates of 1, 3 and 5 mL/min. The corresponding rpm of the pump are presented in Table 12.

Table 12: Corresponding rpm to the desired electrolyte flow rates

Flow rate [mL/min]	RPM
1	17
3	50
5	84

6.2.2. Electrochemistry

The electrochemistry of the thin layer flow cell is tested using cyclic voltammetry. The with CO_2 saturated 0.1 M KCl electrolyte is pumped with 1 mL/min through the thin layer flow cell. Then the potential is cycled from 0 V to -1.4, -1.6 and -1.8 V vs Ag/AgCl reference electrode respectively and back to 0 V again. The resulting cyclic voltammograms are presented in Figure 34. As can be seen in this figure, the cyclic voltammograms do not reach the set applied potentials. This is due a malfunctioning Ag/AgCl reference electrode. The used Ag/AgCl reference electrode had an offset of -0.25 V. During the cyclic voltammetry measurements, this offset is taken into account so that the measured potentials correspond to the actual applied potentials of -1.4, -1.6 and -1.8 V vs Ag/AgCl respectively. During the CO_2 reduction reaction measurements, a proper working Ag/AgCl reference electrode is used.

By taking a closer look at Figure 34, one can see that the onset potentials are almost identical in the three measured voltammograms. Until a potential of -0.4 V, which corresponds to -0.65 V vs Ag/AgCl, the voltammograms of -1.4 and -1.6 V overlap whereas the voltammogram of -1.8 V shows a more negative slope. Until this potential, all voltammograms show a linear decrease of the current density with decreasing potential without fluctuations. From this potential onwards, the current density starts to decrease more strongly with decreasing potential until the desired applied potential is reached. This is an indication that the CO_2 reduction reaction takes place. Since the same 0.1 M KCl electrolyte is used during the measurements one would expect that the voltammograms overlap each other at the shared potential range however this is clearly not the case. This might be due to fact that the electrolyte is fed back to the reservoir from where it is pumped back into the cell, so that it is possible that small amounts of reaction products are present which have an influence on the current flowing through the cell. Furthermore, it is striking that periodic fluctuations start to occur from this potential on. The measured voltammograms show moreover the expected behaviour. The more negative the applied potential, the more negative the current density. This confirms that the CO_2 reduction reaction occurs and that reaction products are formed. When cycling back to 0 V all three voltammograms show the same behaviour. With increasing potential, the current densities get less negative however, are lower than on the forward cycle. It crosses the forward cycle at a potential of -0.2, -0.6 and -0.65 V in the voltammograms of -1.4, -1.6 and -1.8 V respectively. Thereafter, the fluctuations disappear again and the current increased linearly with increasing potential as in the forward cycle.

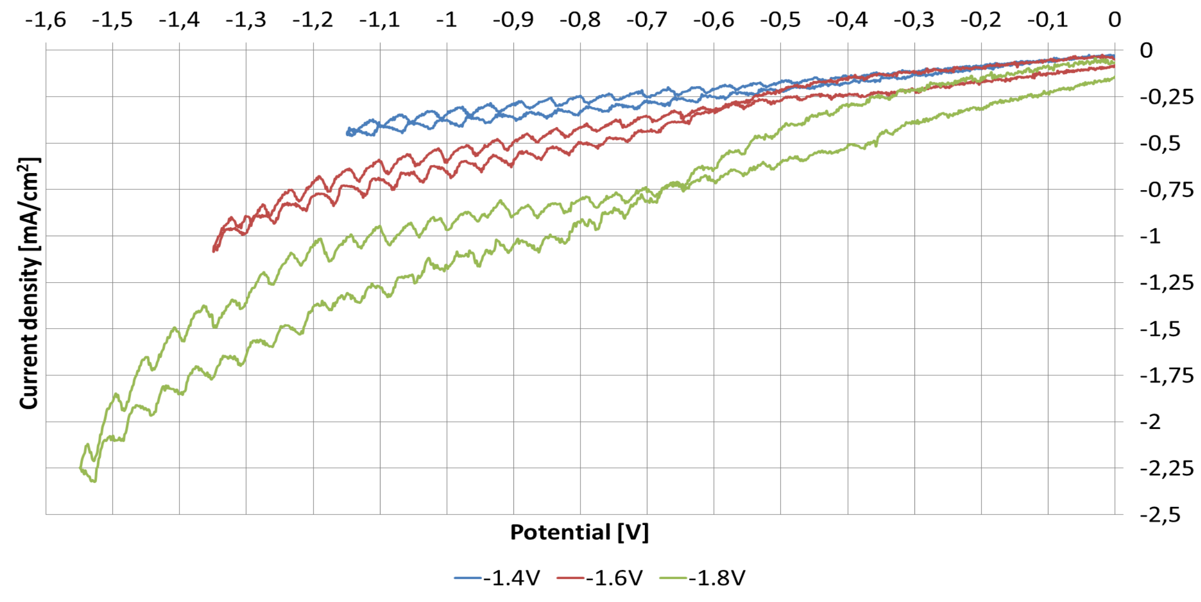

Figure 34: Influence of the applied potential on the cyclic voltammetry of with CO_2 saturated 0.1 M KCl at an electrolyte flowrate of 1 mL/min

Since the CO_2 reduction reaction measurements are also performed with different flowrates of the electrolyte, the influence of the flowrate of the electrolyte on the electrochemistry of the thin layer flow cell is also investigated. Again, this is done with cyclic voltammetry. The with CO_2 saturated 0.1 M KCl electrolyte is pumped with 1, 3 and 5 mL/min through the thin layer flow cell and the potential is cycled to -1.4 V vs Ag/AgCl and back to 0 V. The resulting cyclic voltammograms are presented in Figure 35. The same behaviour of the voltammograms is observed as in the voltammograms measured at different applied potentials. Again, the voltammograms show a linear decrease in current density with no fluctuations with a decrease in potential. However, now all three voltammograms overlap until a potential of -0.4 V which corresponds to -0.65 V vs Ag/AgCl. Between -0.4 and -0.6 V the current density decreases more strongly with decreasing potential. Furthermore, from this potential on the fluctuation in the current density starts to occur again. From -0.6 V which corresponds to -0.85 V vs Ag/AgCl until the final potential of -1.4 V vs Ag/AgCl the current density decreases linearly again with decreasing potential. When cycling back to 0 V all three voltammograms show the same shape. With increasing potential, the current densities get less negative and increase linearly until 0 V. The points where the current density crosses the forward cycle are shifted to a lower potential in comparison to the measurements taken at different potentials. The current densities cross at a potential of -0.1, -0.35 and -0.5 V in the voltammograms of 1, 3 and 5 mL/min respectively. Thereafter, the fluctuations disappear again, and the current density increased linearly with increasing potential as in the forward cycle.

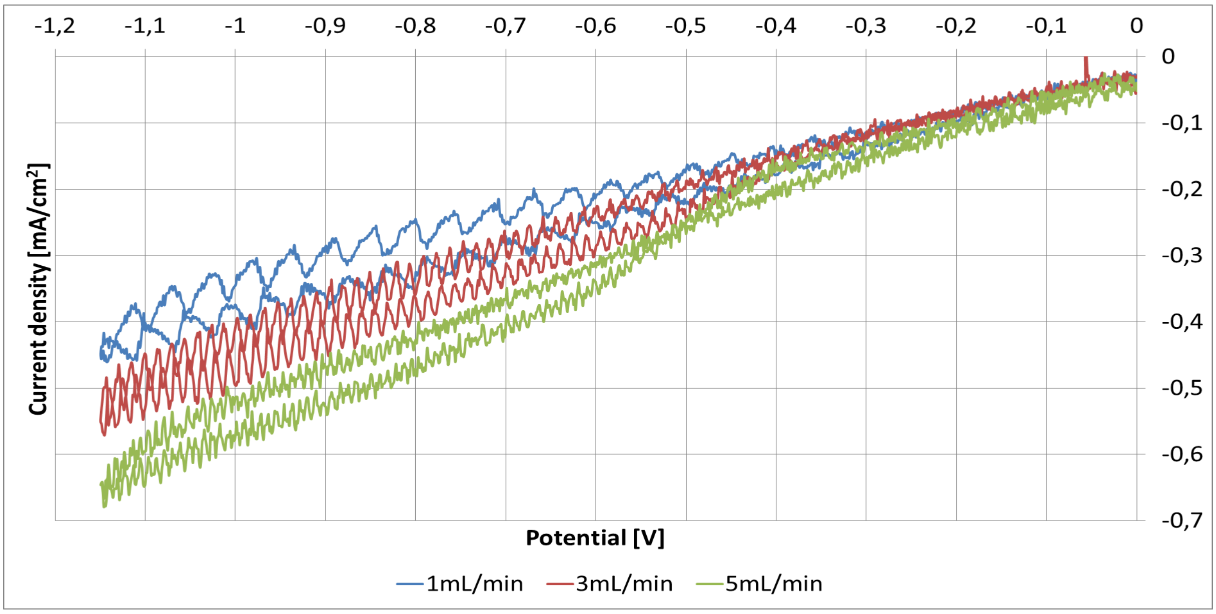

Figure 35: Influence of the flowrate on the cyclic voltammetry of with CO_2 saturated 0.1 M KCl at an applied potential of -1.4 V vs Ag/AgCl

Regarding the fluctuations in the measured current densities, one can clearly see that the higher the flowrate of the electrolyte the smaller and lower the fluctuations in the measured current densities. This is the consequence of the used variable speed Cole-Parmer Masterflex L/S peristaltic pump. As discussed in section 5.1.2 the flowrate of the electrolyte is defined by the adjusted rpm of the pump. In section 6.2.1 the calculated rpm corresponding to 1, 3 and 5 mL/min are presented in Table 12. Every rpm corresponds to a pulse. So, the more rpm the more pulses and the smaller the fluctuation in the measured current density. The intensity of the fluctuation is related to the residence time of the electrolyte. A low flowrate corresponds to a long residence time which allows more CO_2 to be reduced and thereby causing the neutralization of the electrolyte. A higher flowrate results in a shorter residence time and thus preventing the neutralization of the electrolyte resulting in lower current fluctuations. What further is noticeable, is that the higher the flowrate the more negative the measured current density.

The obtained results from the cyclic voltammetry measurements show that the electrochemistry of the thin layer flow cell matches the expectations and the performance of the ATR cell. Current is flowing and the more negative the applied potential the more negative the current density. Investigation of the flowrate on the measured current density shows that the higher the flowrate the more stable the current density. Therefore, the FTIR absorption spectra during the CO_2 reduction reaction are measured with an electrolyte flowrate of 5 mL/min.

6.2.3. Set angle ATR accessory

Unlike the germanium ATR crystal which has a face angle, the calcium fluoride IR window is flat. The IR beam of the IR spectrometer is directed by the ATR accessory, see Figure 17, to the calcium fluoride window. There it is refracted and transmitted through the calcium fluoride IR window. At the interface of the IR window with the electrolyte, the IR beam is refracted again and transmitted through the electrolyte to the silver working electrode where the IR beam is reflected. The schematic representation of the IR beam path inside the thin layer flow cell is presented in Figure 36.

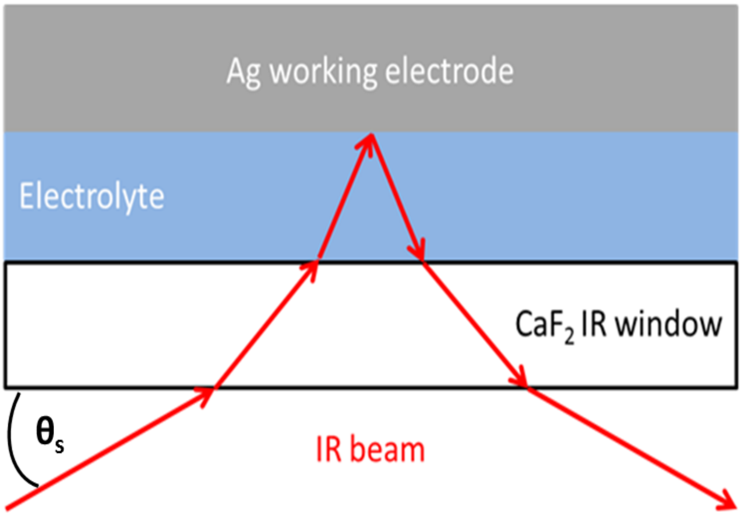

Figure 36: Schematic representation of the IR beam path inside the thin layer flow cell

The angle of incidence of the IR beam on the calcium fluoride window is set by the set angle, θ_s, of the ATR accessory. It can be adjusted between 30 and 80°. In order to obtain a good FTIR absorption spectrum, during the CO_2 reduction reaction measurement, it is key to measure the IR absorption at the highest possible IR signal strength. The intensity of the IR signal reaching the detector is measured inside the IR spectrometer and can be read out from the OPUS software. The intensity of the IR beam is determined over the entire set angle range of the ATR accessory in 5 degrees intervals for two cases. First, the IR signal is determined for an empty cell. In this case air is pumped through the cell. As introduced in section 2.4 aqueous electrolytes absorb large amounts of IR radiation. This is mainly because of the spectral interference of liquid water. Therefore, the IR signal is also determined when water is pumped through the cell. The ATR measurements are performed with an aperture setting of 1.5 mm. This aperture showed not sufficient large enough IR signals for the thin layer flow cell. The larger the aperture the larger the IR signal. The surface where the IR beam is reflected is circular with a diameter of 1 cm. The cell is designed in such a way that the IR beam is directed to the middle of this area. However, to be sure that the IR beam is located in this area an aperture setting of 6 mm is used to prevent that the IR beam is reflected by the platinum counter electrode which is deposited on the calcium fluoride IR window due to misalignment. The resulting IR intensities at different set angles of the ATR accessory for the cell filled with air and with water with an aperture of the IR beam of 6 mm are presented in Table 13.

It is striking, that the measured intensities of the IR signal only differ with set angles on the ATR accessory between 30° and 45° for the two cases. From 50° to 80°, the intensities of the IR signal are similar. For both cases, the maximum measured intensity of the IR beam is found at a set angle of the ATR accessory of 36°. The maximum intensity of the IR beam in the cell filled with air is 8282 whereas in the cell filled with water the intensity of the IR beam is only 3275. This is about a factor of 2.5 difference in IR signal intensity indicating that water indeed absorbs a large amount of water. Based on this result, the FTIR spectra in the thin layer flow cell are measured with an aperture of the IR beam of 6 mm and a set angle of incidence of 36° on the ATR accessory.

Table 13: Measured IR signal intensities at different set angles of the ATR accessory with air and water inside the thin layer flow cell

Set angle ATR accessory [°]	Intensity IR signal with air	Intensity IR signal with water
30	6115	2493
35	8551	3195
40	6584	2774
45	2212	1765
50	507	501
55	228	231
60	188	191
65	105	106
70	295	320
75	159	167
80	68	68

6.2.4. Reference FTIR absorption spectra

The reference IR absorption spectra of air, water and both, 0.1 M KCl and 0.1 M $KHCO_3$, electrolytes without and saturated with CO_2 are measured. As discussed in section 6.1.1.1 the reference IR absorption spectrum of water is measured against an air background spectrum. This results in strong IR absorption bands. In comparison, the reference IR absorption spectra of the electrolytes are measured against a water background spectrum resulting in small absorption bands. These absorption bands are overshadowed by the strong absorption bands of water. Since water and air are not used in the CO_2 reduction reaction measurements, these reference spectra are omitted here. The reference IR absorption spectra of the pure electrolytes measured against a water background and with CO_2 saturated electrolytes measured the pure electrolyte background are presented in Figure 37.

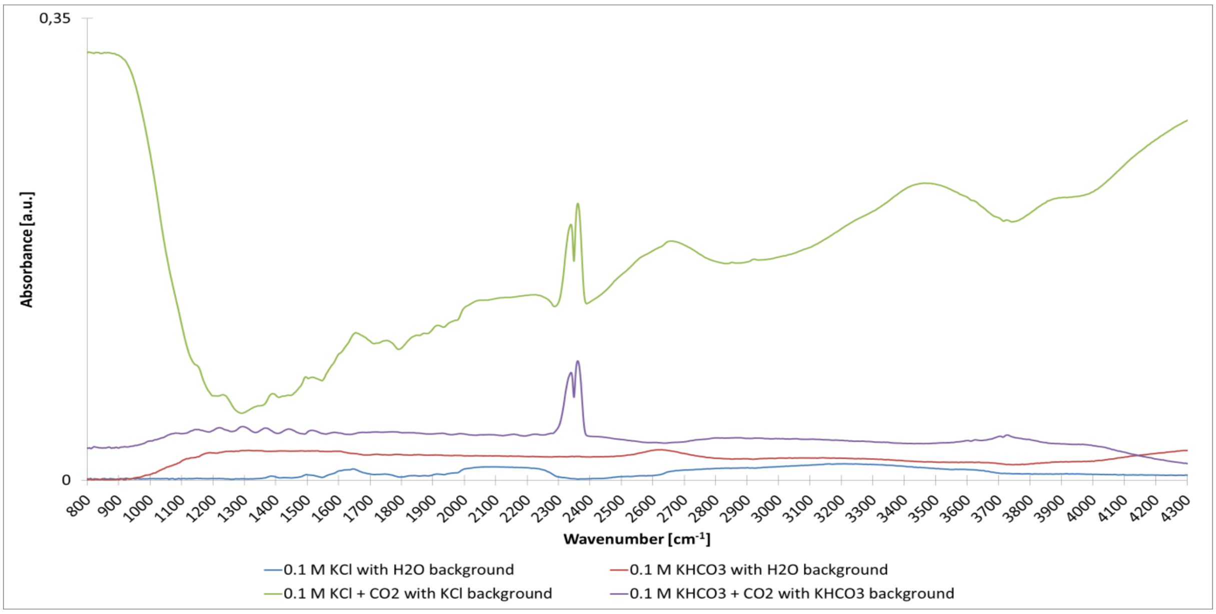

Figure 37: Reference FTIR absorption spectra of the electrolytes with and without CO_2

As can be seen, there are no distinctive IR absorption bands present in the measured FTIR spectra of both electrolytes. In both with CO_2 saturated electrolytes a strong doublet IR absorption band is present at a wavenumber of 2350 cm^{-1}. According to the values found in literature, see Table 3, these doublets correspond to CO_2. Since CO_2 is bubbled through the electrolyte and subsequently the electrolyte is pumped through the thin layer flow cell it is hard to distinguish whether the doublet corresponds to dissolved or gaseous CO_2 as both are present in the cell. During the experiment gas bubbles were present in the teflon tube through which the electrolyte is pumped to the cell. Therefore, it is likely that the doublet is a combination of both, dissolved and gaseous CO_2, present inside the cell.

Further, it is striking that the baseline of the reference IR absorption spectrum of with CO_2 saturated 0.1 M KCl deviates from the other reference IR absorption spectra. Whereas the baselines of the reference IR absorption spectra of 0.1 M KCl, 0.1 M $KHCO_3$ and with CO_2 saturated 0.1 M $KHCO_3$ consists of a flat line with no distinct IR absorption bands, the baseline of with CO_2 saturated 0.1 M KCl shows a strong decrease with increasing wavenumbers until 1300 cm^{-1} and from that point on a linear increase until the end of the wavenumber range at 4300 cm^{-1}. In the increasing part of the baseline small and broad IR absorption bands are present. Based on the reference spectrum of pure 0.1 M KCl and the spectrum of with CO_2 saturated 0.1 M KCl measured with the ATR cell no IR absorption bands other than CO_2 should be present.

A possible explanation for the different baseline in the with CO_2 saturated 0.1 M KCl reference IR absorption spectrum is that gaseous CO_2 was present during the measurement of the IR absorption spectrum. In comparison to the background measurement of the pure electrolyte, the gaseous CO_2 displaces the liquid electrolyte inside the cell, resulting that the amount of liquid in the cell changes and that there may no liquid present anymore between the calcium fluoride IR window and the silver working electrode where the IR beam is reflected. As discussed in section 6.2.3 the IR signal strength is much larger when no water is present between the calcium fluoride IR window and the silver working electrode. Since the reference IR spectrum is based on the difference between the background measurement of the pure electrolyte and the measurement of the with CO_2 saturated electrolyte the deviation of the base line is a result of a much stronger IR signal of the measurement compared to the background.

6.2.5. CO_2 reduction reaction

The CO_2 reduction reaction measurements were performed at three different potentials, -1.4, -1.6 and -1.8 V vs Ag/AgCl, in two different electrolytes, 0.1M KCl and 0.1 M $KHCO_3$, in the spectroelectrochemical thin layer flow cell. All the FTIR spectra were taken at three-minute intervals for ten minutes. First, the current density vs time characteristics of the different applied potential in the different electrolytes are presented. Subsequently, the resulting FT-IR absorption spectra during the CO_2 reduction experiments are presented and analysed. Finally, the influence of the flowrate of the electrolyte on the IR absorption spectra is investigated.

6.2.5.1. Current density vs time characteristics

The current density vs time characteristics of the three applied voltages in the two different electrolytes are presented in Figure 38. The blue, red and green line in the figure correspond to -1.4, -1.6 and -1. 8 V vs Ag/AgCl respectively. As can be seen in the top part of this figure, the current density vs time behaviour shows a fluctuating character. Especially in the case of the 0.1 M KCl electrolyte. 100 seconds after applying a potential of -1.4 V vs Ag/AgCl to the thin layer flow cell, the current density starts fluctuating between -0.6 and -106 mA/cm^2. The characteristics in the 0.1 M $KHCO_3$ electrolyte show a more stable behaviour than the one in 0.1 M KCl. The current density only starts fluctuating between +1 and -1 mA/cm^2 after the occurrence of the of the peak at 280 seconds of -9.5 mA/cm^2. At an applied potential of -1.6 V vs Ag/AgCl the fluctuation starts after 300 seconds in 0.1 M KCl whereas the current density remains steady in 0.1 M $KHCO_3$ despite some present dips. The same holds for an applied potential of -1.8 V vs Ag/AgCl. In the 0.1 M KCl electrolyte however strong fluctuation of the current density is present from the start on, reaching a low of -105 mA/cm^2 after 130 seconds and large positive peaks as the time increases.

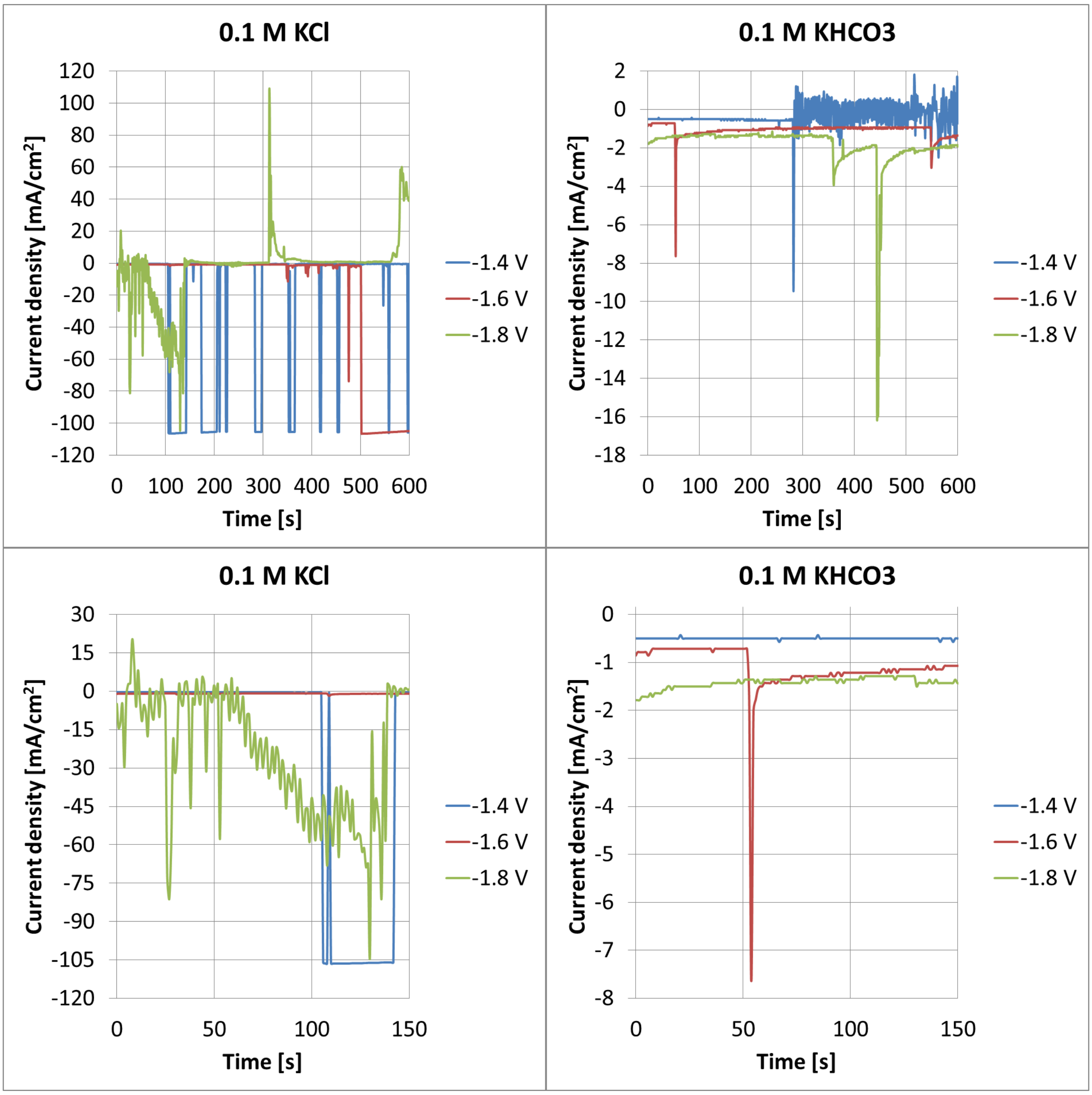

Figure 38: Current density vs time characteristics during the CO_2 reduction reaction in the different electrolytes at different applied potentials. Top: During the entire measurement. Bottom: Zoom in of the first 100 seconds of the measurement

The large negative current densities are an indication of a short circuit. Investigation of the electrodes after the measurement of the CO_2 reduction reaction showed that the platinum counter electrode which is sputtered directly on the calcium fluoride IR window has cracked and pieces are separated from the surface. Since only a 25 µm thin electrolyte layer separated the working and counter electrode from each other, it is likely that the loosened pieces of platinum caused a short circuit by touching the silver working electrode. Due to this, only the first 100 and 300 seconds after applying a potential to the thin layer flow cell are considered to give useable results in 0.1 M KCl and 0.1 M $KHCO_3$ respectively. In order to compare the results of the CO_2 reduction reaction measurements in both electrolytes, the FTIR absorption spectra taken after one minute are used.

Zooming in on the first 100 seconds, presented in the bottom part of Figure 38, it can be seen that in both electrolytes the same characteristics are present. The more negative the applied potential, the more negative the current density. This corresponds to the obtained results of the performed experiments with the ATR cell and indicating that the CO_2 reduction reaction occurs and that reaction products are formed.

6.2.5.2. FTIR absorption spectra at different applied potentials

The reaction intermediates and products formed during the CO_2 reduction reaction are determined by measuring the FTIR absorption spectra in two different electrolytes, 0.1 M KCl, 0.1 M $KHCO_3$ and at different applied potentials, -1.4, -1.6 and -1.8V against a Ag/AgCl reference electrode. The measured FTIR absorption spectra are divided into low, 900-2400 cm^{-1}, and high, 3000-4000 cm^{-1} wavenumber regions in order to be able to determine the IR absorption bands more clearly. As discussed in the previous section only the first 100 seconds after applying a potential show the desired current density vs time characteristics. Therefore, only the IR absorption spectra taken after one minute are used.

The resulting FTIR spectra measured in 0.1 M KCl and 0.1 M $KHCO_3$ after one minute are presented in Figure 39 and Figure 40 respectively. The present IR absorption bands in the FTIR spectra corresponding to the CO_2 reduction reaction intermediates and products are assigned using values found in literature on the CO_2 reduction reaction and reactions of other small organic molecules as introduced in section 2.5 and presented in Table 3 and Table 4. The found IR absorption bands in the performed experiments are summarized in Table 14.

By taking a look at the measured FTIR spectra in the two electrolytes and applied potentials the following trends can be observed. All the spectra measured during the CO_2 reduction reaction experiments show a doublet absorption band at a wavenumber of 2350 cm^{-1}. As already discussed in section 6.2.4, this absorption band is not present in the measured FTIR spectra of the pure electrolytes without an applied potential. This absorption band however, is present in the measured reference FTIR absorption spectra of the with CO_2 saturated electrolytes without an applied potential as presented in Figure 37. Again, both dissolved and gaseous CO_2 is present during the measurement. Therefore, it is difficult to assign the absorption bands either to dissolved or gaseous CO_2 since the wavenumbers at which the peaks of the absorption bands occur for both are in close vicinity of each other as can be seen in Table 3. So, it is likely that this IR absorption band is a combination of both. In any case it can be assigned to a CO_2 species present in the cell as the wavenumber of the absorption peak corresponds with the wavenumbers found in literature as summarized in Table 3 and Table 4.

Furthermore, next to the doublet IR absorption band at a wavenumber of 2350 cm^{-1} corresponding to dissolved or gaseous CO_2 in the electrolytes, two other distinct IR absorption bands are present in the low wavenumber region, 900-2400 cm^{-1}, in all the measured IR absorption spectra during the CO_2 reduction reaction. The IR absorption bands around wavenumbers of 1650 cm^{-1} and 1360 cm^{-1}. The IR absorption band at 1650 cm^{-1} is negative in most cases with the exception of the measurements performed in 0.1 M KCl with an applied potential of -1.4 V vs Ag/AgCl and in 0.1 M $KHCO_3$ with an applied potential of -1.8 V vs Ag/AgCl.

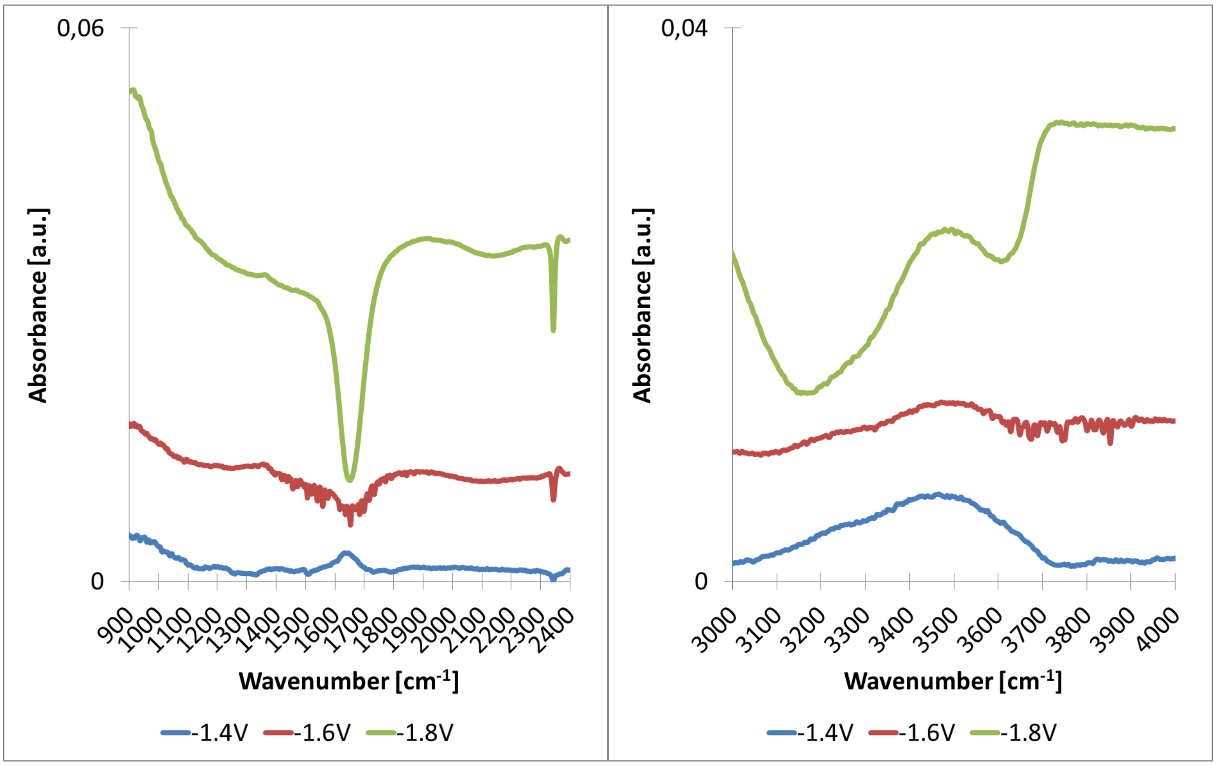

Figure 39: Measured FTIR absorption spectra of the CO_2 reduction reaction in 0.1 M KCl at different applied potentials after one minute divided into the low and high wavenumber region

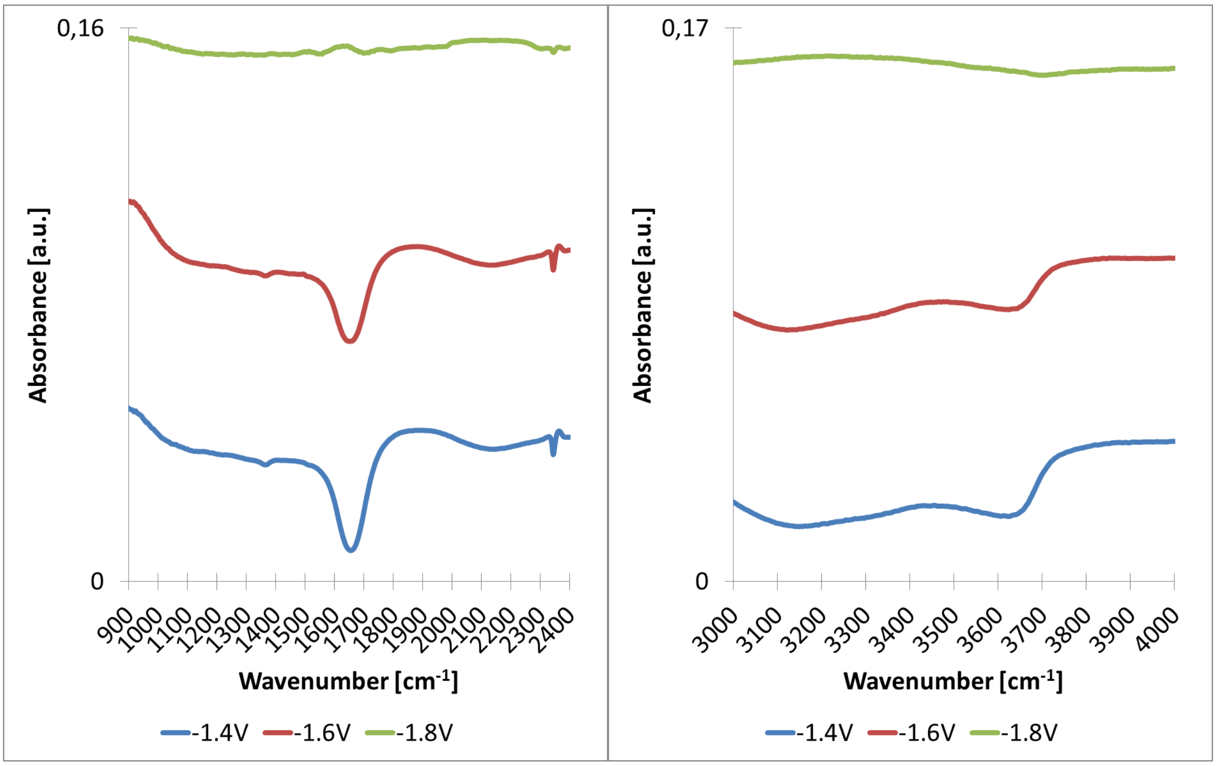

Figure 40: Measured FTIR absorption spectra of the CO_2 reduction reaction in 0.1 M $KHCO_3$ at different applied potentials after one minute divided into the low and high wavenumber region

Again, a negative band indicates that a vibration of a bond is not present anymore with respect to the background measurement. A positive band indicates a new vibration of a bond since this vibration was not present in the background measurement. Based on the investigated studies in literature, see section 2.5, this absorption band correspond to O-H deformation of surface bound water. The CO_2 reduction reaction takes place at the surface of the electrode. Therefore, it is expected that water is replaced by reaction intermediates and products at the electrode resulting in a negative IR absorption band.

The resulting positive bands in the above-mentioned cases contradict the expected behaviour. This is likely to be caused by the presence of gaseous CO_2 inside the cell during the background IR absorption measurement under open circuit conditions. The gaseous CO_2 bubbles replace the electrolyte inside the cell. The CO_2 bubbles are however carried away by the electrolyte flow so that it is possible that, during the IR absorption measurement, no CO_2 bubbles were present in the cell and that their occupied space is replaced by water resulting that more water is present in the cell as compared to the background measurement causing a positive IR absorption band. The exact peak locations of these IR absorption bands can be found in Table 14.

The second IR absorption band occurs at 1360 cm^{-1} and is positive in the IR absorption spectra obtained from the measurements performed in 0.1 M KCl whereas it is negative in the measured IR absorption spectra with 0.1 M $KHCO_3$. According to the investigated literature in section 2.5 this IR absorption band corresponds to a carbonate species. When looking at Table 3, where the peak assignments of the studied literature are summarized, it is striking that on the one hand surface bonded carbonate species always show a symmetric and asymmetric stretch vibration thus two IR absorption bands should be present between 1280-1380 cm^{-1} and 1400-1600 cm^{-1}. On the other hand, however, dissolved carbonate shows only one IR absorption band between 1300 and 1500 cm^{-1}. Furthermore, Garcia et al. [46] argue that when no asymmetric stretch vibration is present, the carbonate is bonded perpendicular to the surface of the electrode. Based on these insights it is difficult to assign the IR absorption band peak to either monodendate bound or dissolved carbonate. What can be said however, is that carbonate is formed during the CO_2 reduction reaction at all applied potentials in 0.1 M KCl and is reduced in 0.1 M $KHCO_3$ due to the present positive and negative IR absorption band in the IR absorption spectra measured at different potentials respectively.

At the high wavenumber region, 3000-4000 cm^{-1}, broad IR absorption bands are present in almost all measured FTIR absorption spectra with the exception of the measured IR absorption spectrum in 0.1 M $KHCO_3$ with an applied potential of -1.8 V vs AG/AgCl where no distinct IR absorption band can be found. A broad IR absorption band in this wavenumber region corresponds to O-H bending vibrations which occur in the 3000-3600 cm^{-1} range as is shown in Table 4. The spectra obtained from the IR absorption measurements in 0.1 M KCl with applied potential of -1.4 and -1.6 V vs Ag/AgCl show a single positive IR absorption band with a peak around 3500 cm^{-1}. The spectrum measured at -1.8 V vs Ag/AgCl shows a negative band with two peaks. This is also the case in the spectra measured in 0.1 M $KHCO_3$ with applied potential of -1.4 and -1.6 V vs Ag/AgCl. As discussed in section 6.1.2.3, an increase in wavenumber represents an increase in binding energy. When water molecules are bound to a surface the O-H bending energy is lower than in free water molecules and occurs at a lower wavenumber. Due to this, the peaks around 3100 cm^{-1} and 3600 cm^{-1} are assigned to surface bound and free water molecules respectively. Since the positive IR absorption bands in 0.1 M KCl occur around 3500 cm^{-1} which is way larger than 3100 cm^{-1} it is expected that these correspond to vibrations of free water molecules. The exact peak locations of the IR absorption bands can be found in Table 14.

The strong and broad positive IR absorption band in the measured spectrum in 0.1 M KCl and an applied potential of -1.4 V vs Ag/AgCl corresponds with the positive IR absorption peak at 1650 cm^{-1} indicating contrary to expectations that more water is present inside the cell as is discussed above. At an applied potential of -1.6 V vs Ag/AgCl the negative peak around 1650 cm^{-1} indicates that water molecules are displaced from the surface. This is not observed in the higher wavenumber region. Due to the slightly positive IR absorption band around 3500 cm^{-1} however more free water molecules are present inside the cell. This indicate that water is displaced from the electrode surface but not in the entire cell by other molecules. At an applied potential of -1.8 V vs Ag/AgCl in 0.1 M KCl and -1.4 and -1.6 V vs Ag/AgCl in 0.1 M $KHCO_3$, the two negative IR absorption bands correspond with the negative absorption band at a wavenumber of 1650 cm^{-1} and thereby with the expectation that water is replaced by reaction intermediates and products inside the cell.

Table 14: Assignments of the observed IR absorption bands present in the FTIR spectra measured after 1 minute at different applied potentials against a Ag/AgCl reference electrode during the CO_2 reduction

Electrolyte	**Absorption bands [cm^{-1}]**			**Assignment**
	-1.4 V	**-1.6 V**	**-1.8 V**	
0.1 M KCl		1361	1365	Monodendate or dissolved CO_3^{2-}
	1643	-1652	-1650	Displacement of interfacial H_2O
	2350	2350	2352	Dissolved or gaseous CO_2
			-3172	Displacement of interfacial H_2O
	3478	3502	-3615	Displacement of free H_2O
0.1 M $KHCO_3$	1361	1361	1386	Monodendate or dissolved CO_3^{2-}
	-1652	-1652	1627	Displacement of interfacial H_2O
	2350	2350	2350	Dissolved or gaseous CO_2
	-3137	-3125		Displacement of interfacial H_2O
	-3627	-3637	-3694	Displacement of free H_2O

6.2.5.3. Influence of the flowrate of the electrolyte on the FT-IR absorption spectrum

The influence of the electrolyte flowrate on the IR absorption spectra during the CO_2 reduction reaction is investigated by performing the CO_2 reduction measurement in the 0.1 M $KHCO_3$ electrolyte at an applied potential of -1.6 V vs Ag/AgCl with electrolyte flowrates of 1, 3 and 5 mL/min. The spectra are again taken after one minute to ensure proper the current density characteristics and to prevent that the IR absorption spectra are taken under short circuit conditions as discussed in section 6.2.5.1. The resulting FTIR absorption spectra taken after one minute are presented in Figure 41.

What immediately is noticeable, is that the IR spectra measured with an electrolyte flowrate of 1 and 5 mL/min have an equal shape. At the low wavenumber range, 800 – 1200 cm^{-1}, and from a wavenumber of 2000 cm^{-1} onwards, the IR spectrum measured at 3 mL/min corresponds to the spectra of 1 and 5 mL/min. In the wavenumber region between 1200 and 2000 cm^{-1} the IR spectrum is however different. Instead of the two-present distinct IR absorption bands in the IR spectra measured at 1 and 5 mL/min at wavenumber of 1360 and 1650 cm^{-1}, the IR spectrum measured at 3 mL/min shows multiple small IR absorption bands. In order to explain this difference, the current density vs time behaviour during the three performed experiments is studied. The current density vs time characteristics of the IR absorption measurements during the CO_2 reduction reaction in 0.1 M $KHCO_3$ at an applied potential of -1.6 V vs Ag/AgCl with different flowrates are presented in Figure 42.

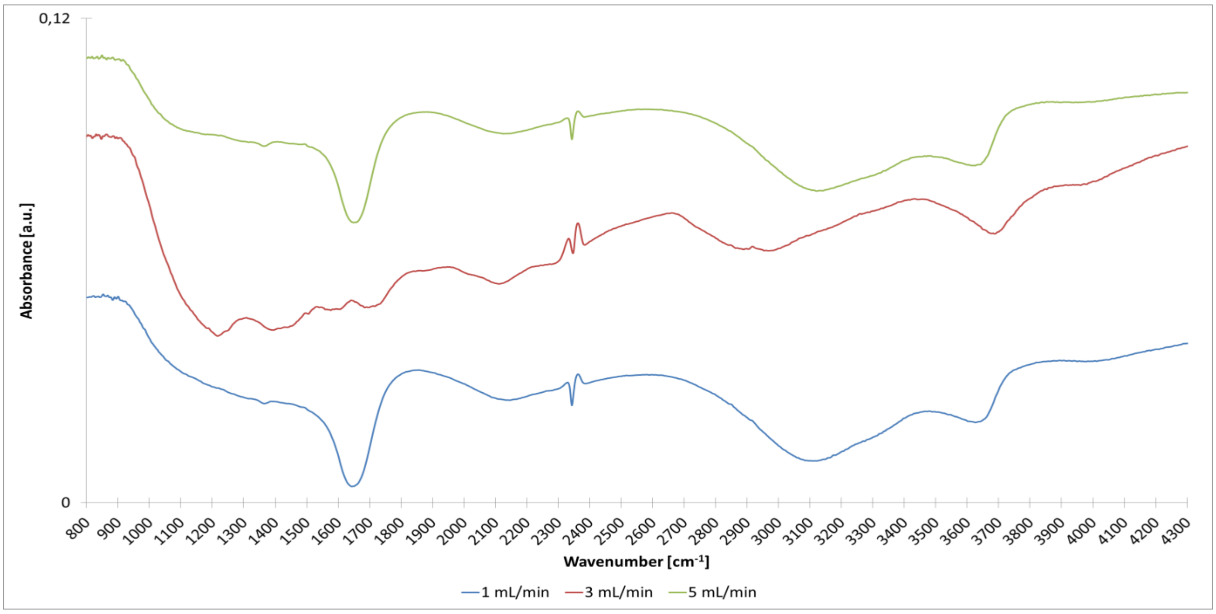

Figure 41: Comparison of the FTIR absorption spectra of the CO_2 reduction reaction in 0.1 M $KHCO_3$ measured at different flowrates after one minute at an applied potential of -1.6 V vs Ag/AgCl

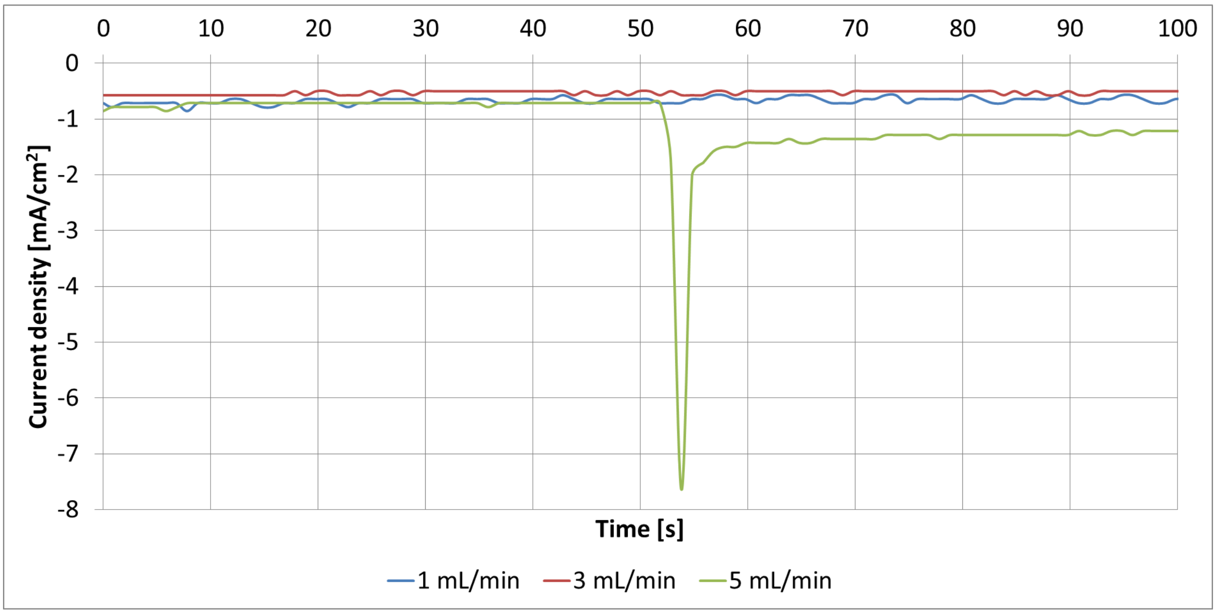

Figure 42: Comparison of the current density vs time characteristics of the CO_2 reduction reaction in 0.1 M $KHCO_3$ measured at different flowrates after one minute at an applied potential of -1.6 V vs Ag/AgCl

What can be seen in this figure, is that the current density during the CO_2 reduction reaction measurement with a flowrate of 3 mL/min is lower than in the measurements with a flowrate of 1 and 5 mL/min. The current density fluctuates between -0.5 and -0.6 mA/cm^2 during the first 100 seconds of the CO_2 reduction reaction, resulting in an average current density of -0.53 mA/cm^2. In contrast, the current density in the measurement performed with a flowrate of 1 mL/min fluctuates between -0.55 and -0.8 mA/cm^2, resulting in an average current density of -0.67 mA/cm^2, whereas, the current density obtained in the measurement with a flowrate of 5 mL/min fluctuates between -0.7 and -0.85 mA/cm^2 for the first 50 seconds and after the dip between -1.2 and -1.5 mA/cm^2 for the last 40 seconds, resulting in an average current density of -1.09 mA/cm^2.

The average current density of the measurement with a flowrate of 3 mL/min is 0.14 and 0.56 mA/cm^2 lower than in the measurements with a flowrate of 1 and 5 mL/min respectively. In comparison, the obtained results of the investigation of the electrochemical performance of the thin layer flow cell, see section 6.2.2, showed that the higher the flowrate the higher the current density. The performed experiments do not follow this trend. As the obtained IR absorption spectra with a flowrate of 1 and 5 mL/min are equal, it is likely that the current density was not high enough in the measurement with a flowrate of 3 mL/min to form the same reaction intermediates and or products. Based on the performance experiments, the current density of the measurement with a flowrate of 3 mL/min is expected to lie in between the measured current densities with a flowrate of 1 and 5 mL/min. Then the current density would be high enough to obtain an equal IR absorption spectrum. Because of this reason, it seems that the flowrate has no influence on the resulting IR absorption spectrum measured in the thin layer flow cell.

6.2.6. Summary

The flowrate of the variable speed Cole-Parmer Masterflex L/S peristaltic pump is determined by measuring the amount of water pumped within one minute at a certain adjusted rpm on the pump with the result, that one rpm corresponds to 0.06 mL/min. As the influence of the flowrate of the electrolyte on the IR absorption spectrum during the CO_2 reduction reaction is also investigated, the measurements are performed at flow rates of 1, 3 and 5 mL/min which correspond to 17, 50 and 84 rpm of the pump.

The electrochemistry of the thin layer flow cell is tested using cyclic voltammetry. The influence of the applied potential is investigated by pumping the with CO_2 saturated 0.1 M KCl electrolyte with 1 mL/min through the thin layer flow cell. The potential is then cycled from 0 V to -1.4, -1.6 and -1.8 V vs Ag/AgCl reference electrode respectively and back to 0 V again. As the same 0.1 M KCl electrolyte is used during the measurements one would expect that the voltammograms overlap each other at the shared potential range however, this was not observed. The measured voltammograms show however the expected behaviour. The more negative the applied potential, the more negative the current density. This confirms that the CO_2 reduction reaction occurs and that reaction products are formed.

The influence of the flowrate of the electrolyte on the electrochemistry of the thin layer flow cell is also investigated with cyclic voltammetry. The with CO_2 saturated 0.1 M KCl electrolyte is pumped with 1, 3 and 5 mL/min through the thin layer flow cell and the potential is cycled to -1.4 V vs Ag/AgCl and back to 0 V. The measured voltammograms show that the fluctuations in the measured current densities are smaller and lower with higher flowrate of the electrolyte.

In order to obtain a good FTIR absorption spectrum during the CO_2 reduction reaction measurement it is key to measure the IR absorption at the highest possible IR signal strength. Since the angle of incidence of the IR beam can be adjusted with the ATR accessory, the intensity of the IR beam reaching the detector is determined over the entire set angle range of the ATR accessory. Aqueous electrolytes absorb large amounts of IR radiation mainly due to the spectral interference of liquid water. Therefore, the set angles of the ATR accessory are determined where the IR intensity is largest for a with air and water filled cell. The found set angle of incidence with the largest IR intensity for a with air and water filled cell is 36° for both cases.

Reference IR absorption spectra of 0.1 M KCl and 0.1 M $KHCO_3$ electrolytes without and saturated with CO_2 are measured. No distinctive IR absorption bands are present in the measured FTIR spectra of both electrolytes. In both with CO_2 saturated electrolytes a strong doublet IR absorption band is present at a wavenumber of 2350 cm^{-1}. Since both dissolved and gaseous CO_2 are present inside the cell it is difficult to distinguish between these species. Therefore, it is likely that the doublet is a combination of both.

The current density vs time characteristics show large fluctuations with increasing reaction time. Especially in the case of the 0.1 M KCl electrolyte. The characteristics in the 0.1 M $KHCO_3$ electrolyte show a more stable behaviour. Only the first 100 and 300 seconds of the reaction in 0.1 M KCl and 0.1 M $KHCO_3$ respectively show stable behaviour. Due to this, only the first 100 seconds are taken into consideration for the comparison. Within the first 100 seconds the characteristics show the expected behaviour. The more negative the applied potential, the more negative the current density. This corresponds to the obtained results of the performed experiments with the ATR cell and indicating that the CO_2 reduction reaction occurs and that reaction products are formed.

The measured IR absorption spectra on silver during the CO_2 reduction reaction in the two electrolytes and at different applied potentials all show a doublet absorption band at a wavenumber of 2350 cm^{-1} and single absorption bands at 1650 cm^{-1} and 1360 cm^{-1} in the low wavenumber region. These correspond to a combination of dissolved and or gaseous CO_2, the O-H deformation of surface bound water and monodendate bound or dissolved carbonate. In the high wavenumber region, broad IR absorption bands are present which can be divided into two bands with peaks around 3100 and 3600 cm^{-1} corresponding to surface bound and free water molecules respectively.

The influence of the electrolyte flowrate on the IR absorption spectra during the CO_2 reduction reaction is investigated by performing the CO_2 reduction measurement in the 0.1 M $KHCO_3$ electrolyte at an applied potential of -1.6 V vs Ag/AgCl with electrolyte flowrates of 1, 3 and 5 mL/min. The spectra are again taken after one minute in order to be able to compare them. The IR absorption spectra measured with an electrolyte flowrate of 1 and 5 mL/min have an equal shape whereas the IR absorption spectra obtained with a flowrate of 3 mL/min shows different behaviour. Investigation of the current density vs time characteristics show that the average current density of the measurement with a flowrate of 3 mL/min of -0.53 mA/cm^2 is 0.14 and 0.56 mA/cm^2 lower than the measurements with a flowrate of 1 and 5 mL/min respectively. This is in contrast with the obtained result from the electrochemical performance test where it was found that the higher the flowrate the higher the current density. Based on this it is expected that the flowrate has no influence on the IR absorption spectra.

6.3. Comparison ATR and thin layer flow cell configuration

The silver working electrode is deposited on different substrates for the ATR and thin layer flow cell configuration. As described earlier, the silver is sputtered by magnetron sputtering on a <1,1,1> single crystal germanium ATR crystal for the ATR configuration, whereas, on titanium foil in the thin layer flow cell configuration. In surface catalysis, the crystal and surface structure of the catalyst plays a key role in the catalytic activity. In order to be able to compare the measured IR absorption spectra measured with the ATR and thin layer flow cell, it has to be ensured that the silver electrode layer on both substrates is the same. To determine this, first, the bulk crystalline structure of the thin silver electrode is determined with X-Ray Diffraction (XRD). The surface is subsequently studied with Atomic Force Microscopy (AFM). Afterwards the measured current density vs time characteristics and IR absorption spectra during the CO_2 reduction reaction in the two different electrolytes at the three applied potentials are compared.

6.3.1. Bulk crystallinity of the silver working electrodes

XRD is a fast-analytical technique that gives accurate information on the bulk crystal structure and crystallinity of a catalyst. X-rays consist of high-energy photons. Due to the high energy, these photons are able to penetrate deeply into the solid catalyst, which makes XRD a bulk technique. The penetrating X-rays are elastically scattered by the crystal planes of the catalyst. From the resulting diffraction pattern, the atoms in the catalyst can be reconstructed. Solids that possess sufficient long-range periodic order are crystalline materials and give rise to XRD patterns. The lattice spacing determines at which angles Bragg diffraction occurs. These angles can be considered as fingerprints of the ordered solid. Therefore, XRD patterns give unambiguous information on the crystal structure.

In order to determine the crystal structure of silver on the germanium ATR crystal and titanium foil first, the XRD patterns of the substrates are determined. The resulting XRD patterns for the germanium ATR crystal and titanium foil are presented in the left-hand side in Figure 43 and Figure 44 respectively. As can be seen the XRD pattern of germanium ATR crystal shows only one sharp large peak at 32°. This indicates a single large perfectly crystalline particle structure. This is expected since it is known that the germanium ATR crystal has a perfect single <1,1,1> crystal structure. Therefore, it is clear that this peak corresponds to the <1,1,1> crystal structure of germanium.

In the XRD pattern of the titanium foil multiple peaks are present. Two are large and sharp, 44 and 47°, whereas the others are smaller and a bit broader, 41, 62, 74, 84, 91, 93 and 99°. This indicates that the titanium foil has a poly crystalline structure with two larger crystalline particle structures and multiple smaller crystalline particle structures, since the smaller the crystalline particle, the broader and lower the peak. The peak at 44° corresponds to the <1,1,1> crystal structure of titanium.

The crystal structure of silver is determined by measuring the XRD pattern of a thin layer of silver deposited on the germanium ATR crystal and titanium foil substrate. The thickness of the sputtered silver layer on the germanium ATR crystal is 50 nm whereas it is 600 nm on the titanium foil. The resulting XRD patterns for a thin layer of silver on the germanium ATR crystal and titanium foil are presented in the right-hand side in Figure 43 and Figure 44 respectively. In contrast to XRD pattern obtained from the germanium ATR crystal, the XRD pattern of the germanium ATR crystal with a thin layer of silver shows three peaks at 32, 44 and 52°. The peak at 32° is a reflection of the germanium ATR crystal substrate. This peak has still the highest intensity indicating that the X-Rays easily penetrate through the thin silver layer into the germanium ATR crystal causing the large perfectly crystalline particle structure of the germanium ATR crystal to be detected. The smaller peaks present at 44 and 52° were not present in the XRD pattern obtained on the germanium ATR crystal. Therefore, these peaks correspond to the present crystalline particle structures of silver. Based on values found in literature [47], these peaks correspond to the <1,1,1> and <2,0,0> crystal structures of silver. As the peak at 44° is way larger than the peak at 52° the majority of the thin silver layer consists of larger particle <1,1,1> crystal structure of silver.

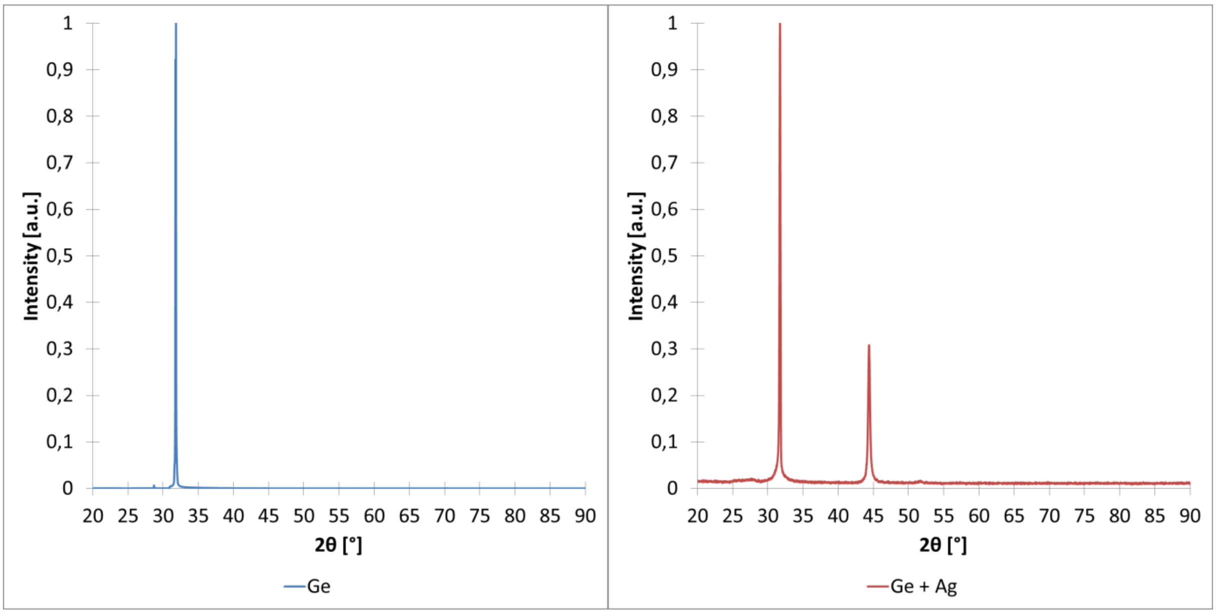

Figure 43: XRD spectra of the bare germanium ATR crystal (left) and the germanium ATR crystal with a thin layer of sputtered silver (right)

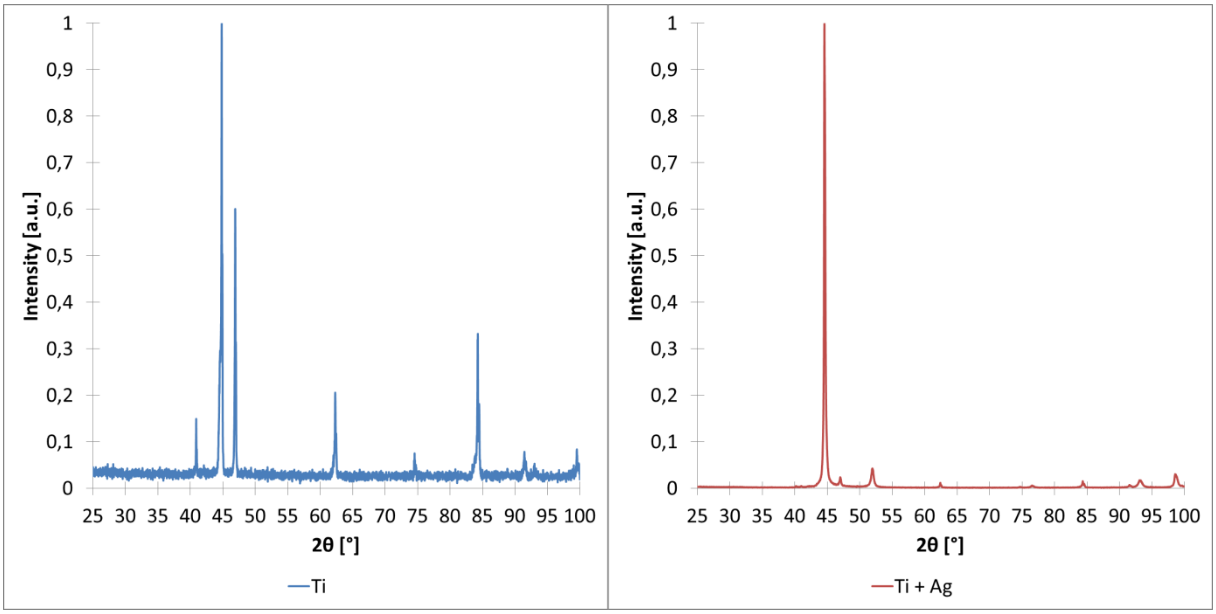

Figure 44: XRD spectra of the bare titanium foil (left) and titanium foil with a thin layer of sputtered silver (right)

Comparing the XRD patterns of the titanium foil with the titanium foil with a thin layer of silver, one can clearly see the similarities. Both show a sharp large peak at 44°. Furthermore, all peaks present in the XRD pattern of the titanium foil with the exception of the peak at 41° are present in the XRD pattern of titanium foil with a thin layer of silver. However, these peaks are smaller in the latter case. This indicates that the silver layer is sufficient thick enough that the X-Rays only penetrate just a little into the titanium foil. As these peaks are present in both patterns these are reflections of the titanium foil substrate. In addition to the reflection, a new peak occurs at 52°. As introduced in the previous paragraph, the peaks at 44 and 52° correspond to the <1,1,1> and <2,0,0> crystal structures of silver. Thus, the peak at 44° correspond to both <1,1,1> crystal structures of titanium and silver. Therefore, the peak at 44° is a combination of the reflection of the <1,1,1> crystal structure of the titanium foil substrate and the <1,1,1> crystal structure of the silver layer on top of the titanium foil substrate. As in the XRD pattern of the germanium ATR crystal with a thin layer of silver, the peak at 44° is way larger than the peak at 52°. This results in that the majority of the thin silver layer consists of larger particle <1,1,1> crystal structure of silver.

Based on the XRD patterns obtained from both substrates, the germanium ATR crystal and the titanium foil, with a thin layer of silver, the bulk crystallinity of the thin silver layer is the same on both substrates. The thin silver layer mainly consists of larger particles with a <1,1,1> crystal structure. However, a small number of smaller particles with a <2,0,0> crystal structure is present as well. The surface of the thin layer of silver is investigated in the next.

6.3.2. Surface structure of the silver working electrodes

The bulk crystallinity of the thin silver layer is the same on both the germanium ATR crystal and titanium foil substrate as concluded in the previous section. The catalytic CO_2 reduction reaction however does not take place in the bulk but on the surface of the silver layer. In order to compare the surfaces of the sputtered thin silver layer on the germanium ATR crystal and titanium foil substrate, the surfaces are studied with AFM.

AFM is a type of scanning probe microscopy which is particularly suitable for the study of surface due to its high resolution. The resolution has the order of nanometres which is more than 1000 times better than the optical diffraction limit. The surface of the sample is scanned with a mechanical probe. The tip of the probe is brought in contact with the sample and the surface is scanned along a x-y grid. The reaction of the probe to the forces that the sample imposes on it can be used to construct a three-dimensional image of the sample surface. This is achieved by raster scanning the position of the sample with respect to the tip and recording the height of the probe that corresponds to a constant probe sample interaction. The surface topography is commonly displayed as a pseudo colour plot, in which each pixel represents an x-y position on the sample and the colour represents the recorded signal. The AFM images of the sputtered silver on the germanium ATR crystal and on the titanium foil substrate are presented in the left and right-hand side of Figure 45 respectively.

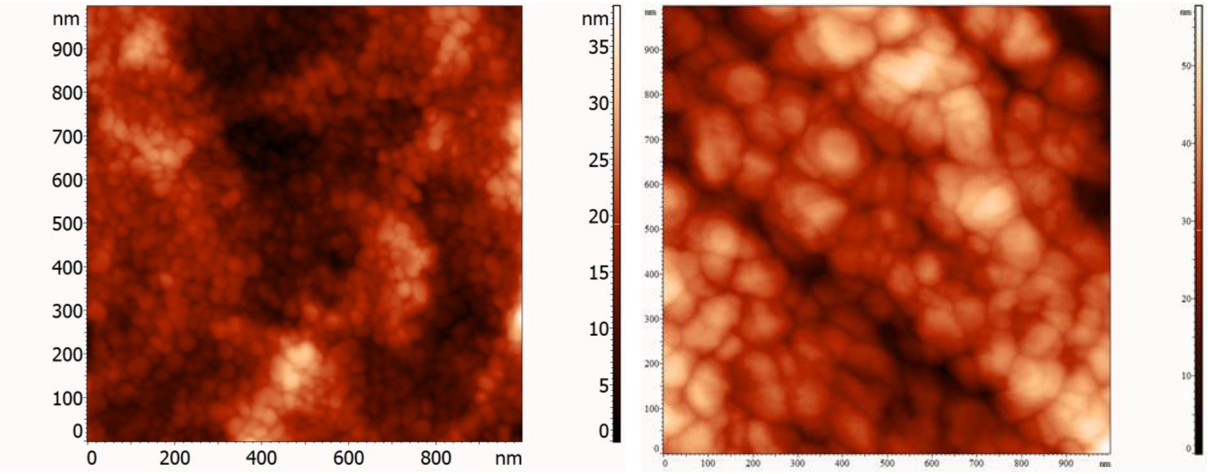

Figure 45: AFM images of sputtered silver on the germanium ATR crystal (left) and on the titanium foil (right)

Both samples were scanned in a 1 by 1 µm grid. By taking a closer look at this figure, one can clearly see that the surfaces of the silver layer on the germanium ATR crystal and titanium foil are both polycrystalline, indicated by the presence of grains, which corresponds to the results obtained from the XRD patterns. However, the grain sizes of the silver crystallites are different on the germanium ATR crystal in comparison to the titanium foil. It can be seen that the grain sizes of the silver crystallites on the germanium ATR crystal have a size around 20-40 nm by 20-40 nm whereas the grain size on the titanium foil is more than twice as big with grain sizes of 60-100 nm by 60-100 nm. Furthermore, the height of the silver surface differs on both substrates. Where the maximum height difference of the silver surface on the germanium ATR crystal is 38 nm, the maximum height difference on the titanium foil is 58 nm. Besides, it can be seen that the AFM image of the silver layer on the germanium ATR crystal has a lot more of dark area in comparison to the AFM image of the silver layer on the titanium foil where the majority of the image is lighter. This indicates that the surface of the silver layer on the germanium ATR crystal is smooth whereas the silver surface on the titanium foil is rougher. As mentioned in the previous section, the thickness of the silver layer is different on the two substrates. The thickness of the silver layer on the germanium ATR crystal is only 50 nm whereas it is 600 nm on the titanium foil. Therefore, it is likely that the rougher surface is attributable to the thicker layer of silver. Based on the two observations it can be concluded that the surfaces of the silver layer resemble each other. Due to this, it is possible to compare the IR absorption spectra measured with the ATR and thin layer flow cell configuration.

6.3.3. Current density vs time characteristics

The two previous sections showed that crystal structure and the surfaces of the thin silver layer on top of the germanium ATR crystal and titanium foil are equal and similar respectively. Since the CO_2 reduction reaction is performed in two different electrochemical cell configurations, ATR and thin layer flow cell, the current density vs time characteristics measured during the CO_2 reduction reaction in both configurations are compared in order to determine the differences. The current density vs time characteristics for the ATR and thin layer flow cell are already introduced in section 6.1.2.1 and 6.2.5.1 respectively. The CO_2 reduction reaction is performed for 30 minutes with the ATR configuration whereas only for 10 minutes with the thin layer flow cell configuration. Furthermore, only for the first 100 and 300 seconds in 0.1 M KCl and 0.1 M $KHCO_3$ electrolytes, the current density vs time characteristics show a stable behaviour in the thin layer flow cell configuration. In the ATR configuration, the current density vs time behaviour is stable during the whole experiment. Due to this, only the first 100 seconds of the performed experiments are taken into consideration for the comparison.

In order to compare the current vs time characteristics, the current density of the silver electrodes have to be determined. The surface areas of the silver electrodes differ in the two cell configurations. In the ATR cell configuration, the silver electrode has a circular surface with a radius of 0.8 cm resulting in a surface area of 2.01 cm^2. In the thin layer flow cell configuration, the surface area of the silver electrode is defined by the teflon spacer, which is a parallelogram with a base of 1.4 cm and a height of 1 cm. This results in a surface area of 1.4 cm^2. To obtain the current densities, the measured currents are divided by the surface areas of the silver electrodes. Figure 46 and Figure 47 show the comparison of the current densities vs time measured in the ATR and thin layer flow cell at the different applied potentials in the 0.1 M KCl and 0.1 M $KHCO_3$ electrolytes respectively.

By taking a closer look at both figures, two things immediately become apparent with the exception of the comparison in 0.1 M KCl with an applied potential of -1.8 V vs Ag/AgCl. First, the current densities in the thin layer flow cell are lower than in the ATR cell. However, these current densities follow the trends of the ATR cell. With increasing applied potential, the current densities get more negative. Furthermore, the current densities are a bit more negative in 0.1 M $KHCO_3$ than in 0.1 M KCl. Second, the current densities in the thin layer flow cell are almost constant over the first 100 seconds after reaching the applied potential. This is not the case in the ATR cell. In the ATR cell the current densities decrease in the first 100 seconds. The currents and thus the current densities decrease even until 400 seconds of the CO_2 reduction reaction, after which they increase again before reaching a steady level after about 25 minutes as can be seen in Figure 25.

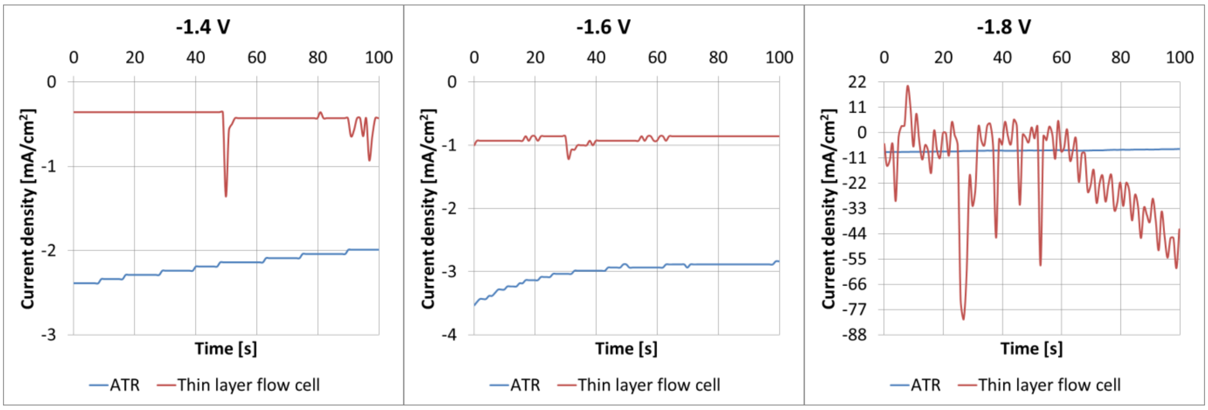

Figure 46: Comparison of the current density vs time in the 0.1 M KCl electrolyte at different applied potentials

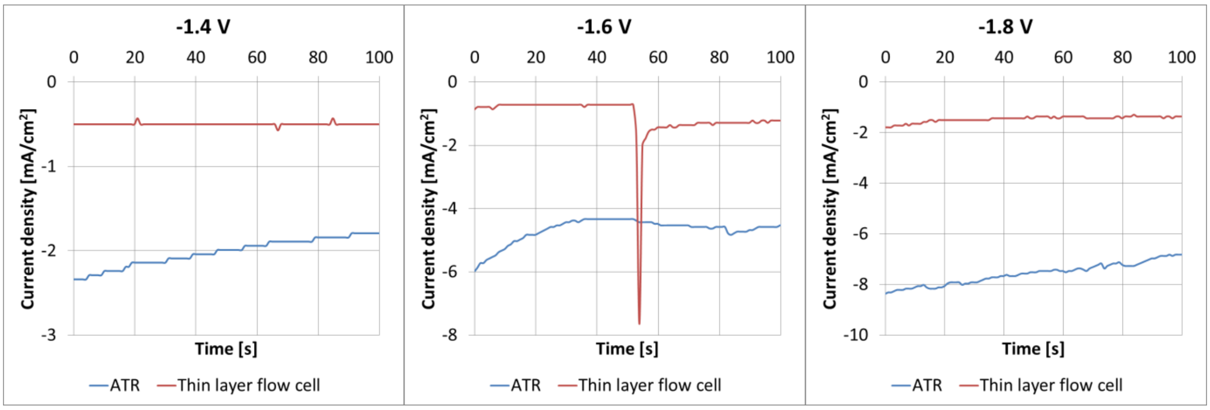

Figure 47: Comparison of the current density vs time in the 0.1 M $KHCO_3$ electrolyte at different applied potentials

6.3.4. IR absorption spectra

In section 6.1.2.3 and 6.2.5.2 the measured FTIR absorption spectra with the ATR and thin layer flow cell are presented and analysed. The CO_2 reduction reaction is measured for 10 and 30 minutes in the thin layer flow and ATR cell respectively. For both cell configurations, the FTIR absorption spectra are measured when the current is constant. As discussed earlier, this is after 25 minutes in the ATR cell whereas only until 100 seconds in the thin layer flow cell. In order to determine the differences in FTIR absorption spectra measured with the ATR and thin layer flow cell, the FTIR absorption spectra taken at the same reaction time of the CO_2 reduction reaction are compared. Since the current is only stable in the first 100 seconds of the CO_2 reduction reaction in the thin layer flow cell, the FTIR absorption spectra taken after one minute are used for the comparison. The comparison of the measured FTIR absorption spectra taken after one minute in the ATR and thin layer flow cell at different potentials in the 0.1 M KCl and 0.1 M $KHCO_3$ electrolytes are presented in Figure 48 and Figure 49 respectively. In the comparison only the low wavenumber region, 900-2400 cm^{-1} is taken into consideration. This is due to the fact that only vibrations corresponding to water molecules occur at the high wavenumber region, 3000-4000 cm^{-1}, and that the FTIR absorption spectra measured in both cell types overlap as previously shown.

Before to be able to compare the measured FTIR absorption spectra, the IR absorption spectra measured with the thin layer flow cell have to be manipulated. The IR absorption bands measured in the thin layer flow cell are way larger than measured in the ATR cell. This is due to the difference in method how the IR absorption is measured. A schematic overview of this difference is presented in Figure 50. In the ATR cell the IR absorption is measured from the back of the working electrode, whereas in the thin layer flow cell from the front. The IR beam has to pass two times the electrolyte. As already mentioned before, the aqueous electrolyte itself absorbs a large part of the IR radiation. In the ATR cell the evanescent wave reaches just a few nm into the electrolyte resulting in less IR absorption by the aqueous electrolyte and thus smaller IR absorption bands. When plotting them together, it was not possible to see the IR absorption bands in the spectra measured in the ATR cell anymore. Therefore, the absorption values of the IR absorption spectra measured in the thin layer flow cell are divided by a factor of 2 for the measurements performed in 0.1 M KCl with applied potentials of -1.4 and -1.6 V vs Ag/AgCl and in 0.1 M $KHCO_3$ with an applied potential of -1.8 V vs Ag/AgCl. The IR spectra measured in the thin layer flow cell of the experiments in 0.1 M KCl with an applied potential of -1.8 V vs Ag/AgCl and in 0.1 M $KHCO_3$ with applied potentials of -1.4 and -1.6 V vs Ag/AgCl are divided by a factor of 10.

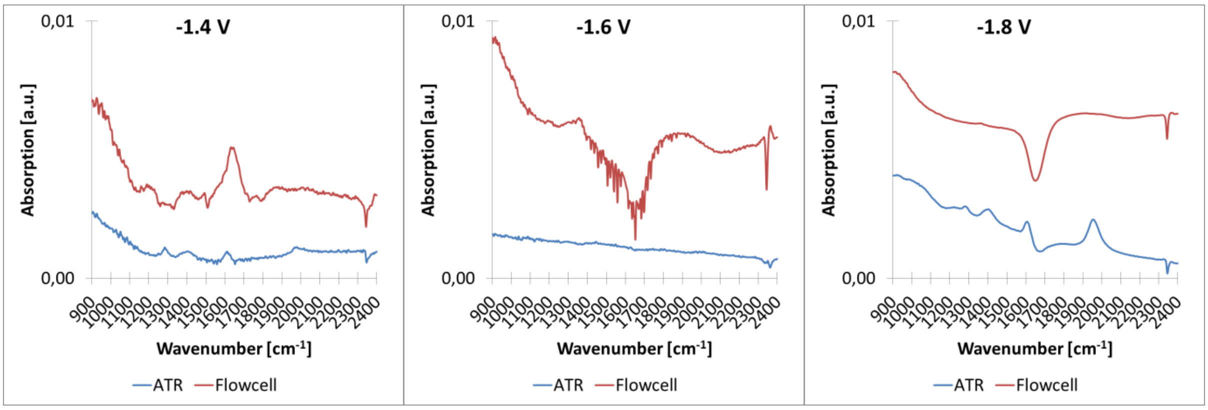

Figure 48: Comparison of the measured FTIR absorption spectra taken after 1 min in the 0.1 M KCl electrolyte at different applied potentials

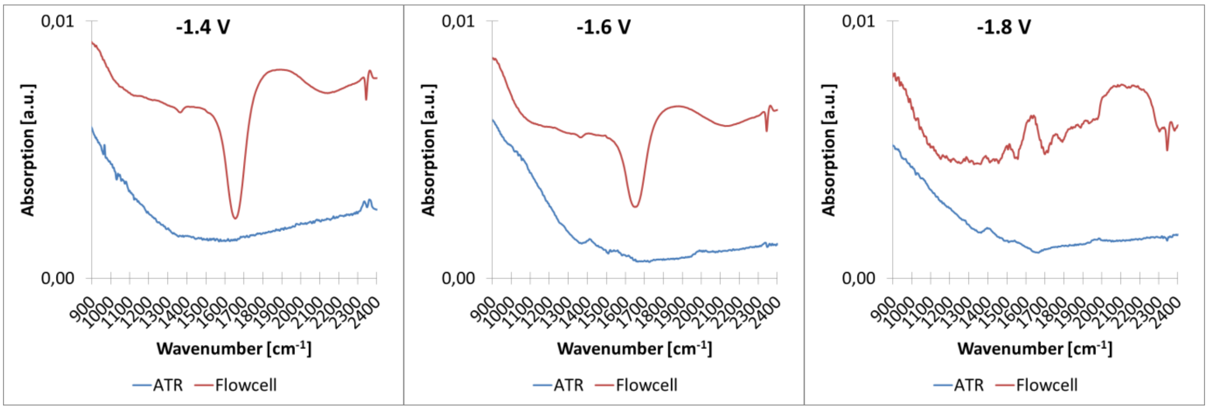

Figure 49: Comparison of the measured FTIR absorption spectra taken after 1 min in the 0.1 M $KHCO_3$ electrolyte at different applied potential

To start with the comparison, first the overall shapes of the FTIR absorption spectra are compared. As can be seen, the FTIR absorption spectra measured with the ATR and thin layer flow cell show the same overall shape. The baseline of the spectra decreases at the lower wavenumber part of the spectra and levels out towards the end of the wavenumber range. The baseline decreases until a wavenumber of 1100 cm^{-1} in the spectra measured in the thin layer flow cell whereas to 1300 cm^{-1} in the spectra taken in the ATR cell. Furthermore, the measured FTIR absorption spectra in the ATR cell have all a comparable shape. Only one major difference can be observed. The absorption band at 1650 cm^{-1} is positive in the measured IR absorption spectrum in 0.1 M KCl with an applied potential of -1.4 V vs Ag/AgCl. In all other cases this band is negative. On the other hand, two distinct shapes can be observed in the spectra measured with the thin layer flow cell. The spectra of the performed experiments in 0.1 M KCl with an applied potential of -1.4 V vs Ag/AgCl and in 0.1 M $KHCO_3$ with an applied potential of -1.8 V vs Ag/AgCl show a positive absorption band at 1650 cm^{-1} whereas this band is negative in the other spectra. The measured FTIR absorption spectra in the ATR and thin layer flow cell correspond to each other in only one case. This is in 0.1 M KCl with an applied potential of -1.4 V vs Ag/AgCl. In all other performed experiments, the spectra differ from each other. However, the IR absorption spectra measured in the thin layer flow cell show similarities with the IR absorption spectra obtained in the ATR cell.

As can be seen in Figure 48 and Figure 49, two IR absorption bands are present in the spectra measured in the thin layer flow cell which also occur in the spectra measured in the ATR cell. These are the bands that occur at wavenumbers of 1650 and 2350 cm^{-1} and correspond as already described before to the O-H deformation of surface bound water and dissolved CO_2 vibrations respectively. The absorption band of CO_2, doublet at the wavenumber of 2350 cm^{-1}, is present in every measured spectrum indicating the presence of CO_2 in both cells. The O-H deformation band of surface bound water is lacking in both spectra measured with the ATR and thin layer flow cell in 0.1 M KCl with an applied potential of -1.4 V vs Ag/AgCl and in the spectrum measured with the thin layer flow cell in 0.1 M $KHCO_3$ with an applied potential of -1.8 V vs Ag/AgCl. In all other measured spectra, this absorption band is negative. This shows that water is replaced from the surface of the electrode.

Three differences in the spectra can be observed when comparing the measured spectra of the ATR with the thin layer flow cell. The main difference between the spectra measured in the ATR and thin layer flow cell is the positive absorption band around 1970 cm^{-1} which is present in the ATR spectra but is lacking in the spectra measured in the thin layer flow cell. According to the studied literature, an absorption band at this wavenumber corresponds to linear bonded CO. CO molecules are thus detected at the surface of the electrode in the ATR cell but not in the thin layer flow cell. The strong negative absorption band at 1650 cm^{-1} suggest that water molecules are displaced from the surface. This corresponds with the results in the studied literature. According to Heinen et al. [29] the water is replaced by CO. The spectra measured in the ATR cell support this. It is likely that because of the strong absorption of the aqueous electrolyte the absorption band of CO in the spectra measured in the thin layer flow cell is overshadowed.

Next, one can see a third absorption band in the spectra measured in the thin layer flow cell. This band occurs at a wavenumber of 1350 cm^{-1}. In the ATR spectra, this band is shifted 50 cm^{-1} to the right. Based on the values found in literature this band corresponds to dissolved carbonate. It is striking that the absorption band at a wavenumber of 1350 and 1400 cm^{-1} is positive for both spectra measured in the thin layer flow and ATR cell in 0.1 M KCl whereas in 0.1 M $KHCO_3$ this band is positive and negative in the spectra measured in the ATR and thin layer flow cell respectively. This indicates that carbonate is produced during the CO_2 reduction reaction in both types of cells in the 0.1 M KCl electrolyte and is released into the electrolyte. In the 0.1 M $KHCO_3$ electrolyte this is also observed in the ATR spectra. In the spectra measured in the thin layer flow cell however, this band is negative indicating that the amount of dissolved carbonate is reduced. This difference can be related to the fact that in the ATR measurements a fixed amount of electrolyte is used, and the dissolved carbonate is accumulated in the vicinity of the electrode surface whereas the electrolyte is replaced in the thin layer flow cell continuously and thereby transporting the carbonate away from the cell. Furthermore, in the thin layer flow cell the whole electrolyte layer is investigated instead of just the layer near the electrode surface as in the ATR cell.

In addition to this absorption band, one and two further absorption bands are present in the ATR spectra measured in 0.1 M $KHCO_3$ and 0.1 M KCl respectively which do not occur in the spectra of the thin layer flow cell. As can be seen, these bands are present at 1280 and 1600 cm^{-1} in the spectra measured in 0.1 M KCl and at 1580 cm^{-1} in the spectra measured in 0.1 M $KHCO_3$. Based on the values found in literature the band at 1280 cm^{-1} corresponds to the symmetric O stretch whereas the band around 1600 cm^{-1} corresponds to the asymmetric O stretch of bidendate carbonate. So, where the spectra measured in the thin layer flow cell only showed an absorption band of dissolved carbonate, the spectra obtained in the ATR cell show clearly that carbonate is also bonded to the surface of the working electrode.

The difference in the IR spectra obtained in the ATR and thin layer flow cell can be explained by how the surface of the electrocatalyst is studied with the IR beam. This is illustrated in the schematic representations of the IR beam path and the locations of the detected molecules in the ATR and thin layer flow cell in the left- and right-hand side of Figure 50 respectively. As already introduced, the way of how the surface of the electrocatalyst is studied differs in both cell types. On the one hand, the surface is probed with an evanescent wave which is generated by the total reflection of the IR beam at the surface of the germanium ATR crystal and the electrocatalyst in the ATR cell. The penetration depth of this evanescent wave is calculated in section 6.1.2.4 and is way larger than the used 20 nm layer of silver electrode in this study. Since the evanescent wave decays exponentially, mainly the surface of the electrocatalyst at the interface with the electrolyte is probed. However, it reaches in the electrolyte and thereby probing also dissolved molecules in close vicinity of the electrocatalyst. Therefore, surface bound, and dissolved molecules can be observed as can be seen in the left-hand side of Figure 50.

On the other hand, the surface of the electrocatalyst is probed by the reflection of the IR beam. The IR beam is refracted at the CaF_2 IR transparent window and reflected at the silver sample. The IR beam passes two times through the aqueous electrolyte. As already discussed, the aqueous electrolyte itself absorbs a large part of the IR beam. In comparison with the ATR cell, the IR beam sees much more water molecules than surface bound and dissolved species as their concentration is only low inside the cell. Due to this reason, the absorption band of surface bound water molecules is much larger than in the ATR cell. As the aqueous electrolyte is saturated with CO_2 before it enters the cell, the CO_2 concentration is relatively high inside the cell and therefore the dissolved CO_2 is detected. Furthermore, the Pt counter electrode is deposited on the CaF_2 IR transparent window. In an electrochemical cell a potential is applied to the cell and therefore the counter electrode is positively charged. The positively charged counter electrode attracts negatively charged ions. As the Pt counter electrode is situated at the bottom of the thin layer flow cell where the IR beam enters and leaves the cell, negative charged ions agglomerate at the bottom of the cell as can be seen in the right-hand side of Figure 50. The IR beam thus sees and detects the dissolve carbonate when entering and leaving the cell.

The comparison of the IR absorption spectra obtained from the ATR and thin layer flow cell showed that the absorption values are larger in the spectra measured in the thin layer flow cell than in the spectra obtained from the ATR cell. This due to the strong IR absorption of the aqueous electrolytes itself. The three present absorption bands in the measured IR spectra in the thin layer flow cell are also present in the obtained IR spectra of the ATR cell. These bands are assigned to dissolved carbonate, the O-H deformation of surface bound water and dissolved CO_2. In the ATR spectra however, three further IR absorption bands can be observed corresponding to bidendate carbonate and linear bonded CO. It is likely that these bands are overshadowed in the IR spectra obtained in the thin layer flow cell due to the large absorption bands of the used aqueous electrolytes. Therefore, based on this observation it can be concluded that from the measured IR spectrum during the CO_2 reduction reaction in the thin layer flow cell no new insights in the reaction mechanism can be gained.

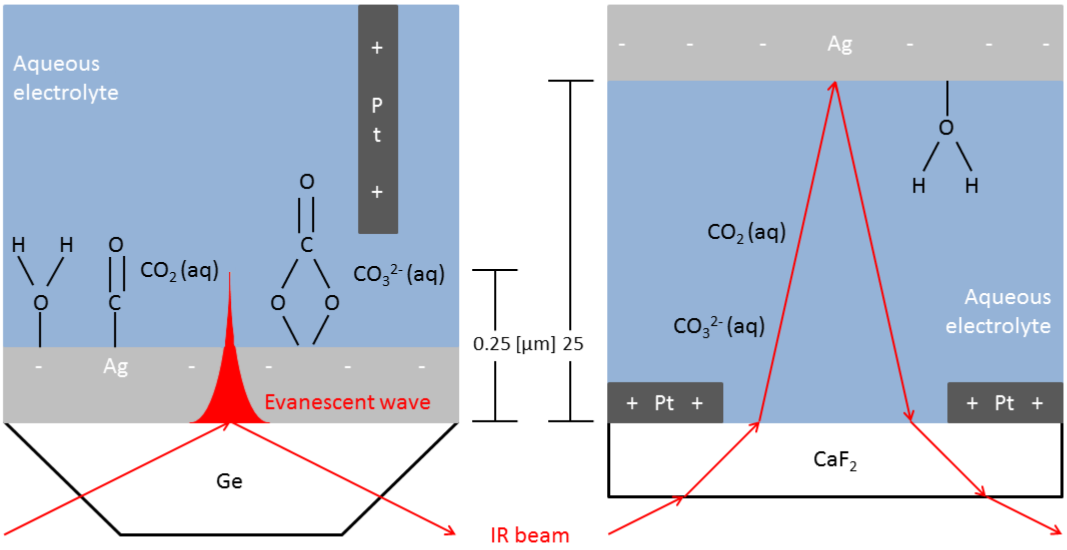

Figure 50: Schematic representation of the cell types and the location of the detected molecules. Left: ATR cell. Right: Thin layer flow cell

6.3.5. Summary

The bulk crystal structures of the thin sputtered silver layers on the germanium ATR crystal and titanium foil substrate are determined with XRD. First, the XRD patterns of the substrates are determined to assign the lines of the substrates. Based on the XRD patterns obtained from both substrates, with a thin sputtered layer of silver, the bulk crystallinity of the thin silver layer is investigated. The results show that the bulk crystal structure is the same on both substrates. The thin silver layer mainly consists of larger particles with a <1,1,1> crystal structure. However, a small number of smaller particles with a <2,0,0> crystal structure is present as well.

The surface of the thin sputtered silver layer is studied with AFM. The analysis of the AFM images of the silver surface on the germanium ATR crystal and titanium foil showed that the surfaces have similar properties. Both surfaces are polycrystalline with clear grain boundaries however differ in grain sizes. The grains on the titanium foil are more than twice as big as on the germanium ATR. The rougher surface of the silver layer on the on the titanium foil is attributed to the thicker layer of silver, 600 nm compared to 50 nm on the germanium ATR crystal. Therefore, it can be concluded that the surfaces of the silver layer resemble each other.

The current density vs time characteristics in the ATR and thin layer flow cell configuration are compared for the first 100 seconds of the CO_2 reduction reaction. Two observations become apparent. The current densities in the thin layer flow cell are lower than in the ATR cell however follow the trends of the current densities in the ATR cell and the current densities in the thin layer flow cell are almost constant over the first 100 seconds after reaching the applied potential. This is not the case in the ATR cell.

The IR absorption spectra measured in the ATR and thin layer flow cell one minute after the start of the CO_2 reduction reaction in 0.1 M KCl and 0.1 M $KHCO_3$ at different applied potentials are compared. The comparison of the IR absorption spectra obtained from the ATR and thin layer flow cell showed that the absorption values are larger in the spectra measured in the thin layer flow cell than in the spectra obtained from the ATR cell. The three present absorption bands in the measured IR spectra in the thin layer flow cell are also present in the obtained IR spectra of the ATR cell. These bands are assigned to dissolved carbonate, the O-H deformation of surface bound water and dissolved CO_2. In the ATR spectra however, three further IR absorption bands can be observed. These bands correspond to bidendate carbonate and linear to the silver surface bonded CO. Therefore, it can be concluded that from the measured IR spectra during the CO_2 reduction reaction in the thin layer flow cell no new insights on the reaction mechanism of the CO_2 reduction reaction can be gained.

7. Conclusion

The design of the new In-Situ IR electrochemical cell is based on the results of the performed literature study and the requirements that came up from the limitations of the current used In-Situ IR ATR cell. Since the main requirement of the new cell is the ability to easily change the electrocatalyst in the cell, it is to use an external reflection cell configuration. Mainly, because the electrocatalyst can be deposited on a cheap conductive substrate that after a measurement can be disposed. To overcome mass transport limitations from the bulk electrolyte to and from the thin layer, electrolyte flow through the cell is chosen. In order to obtain a parallel alignment of the electrocatalyst with respect to the calcium fluoride IR window, a teflon spacer is used in this design. Since the electrolyte is flowing between the calcium fluoride IR window and the silver electrocatalyst, the teflon spacer is also responsible for sealing the cell. The thickness of the teflon spacer determines the thickness of the electrolyte layer. As aqueous electrolytes absorb IR radiation strongly, it is essential to keep the layer of electrolyte as this as possible. For this reason, a teflon spacer with a thickness of 25 µm is used.

Previous research performed with the ATR cell configuration showed that it was possible to determine a reaction mechanism for the CO_2 reduction reaction. Therefore, the experimental results obtained with the ATR cell in this study are used as a reference case. In-Situ ATR-FTIR spectra were measured in 0.1 M KCl, 0.1 M $KHCO_3$, 0.1 M $KClO_4$ and 0.1 M K_2HPO_4 at applied potentials of -1.4, -1.6 and -1.8 V vs Ag/AgCl reference electrode. The obtained ATR-FTIR absorption spectra in 0.1 M K_2HPO_4 and 0.1M $KClO_4$ at the three different applied potentials did not give additional information on species present at the surface of the working electrode. Due to this, the experiments with the thin layer flow cell are only performed with 0.1 M KCl and 0.1 M $KHCO_3$ at the three different applied potentials.

The silver working electrode is deposited by magnetron sputtering on different substrates for the ATR and thin layer flow cell configuration. In surface catalysis, the crystal and surface structure of the catalyst plays a key role in the catalytic activity. The XRD patterns of the sputtered layer of silver on the germanium ATR crystal and titanium foil show that the bulk crystal structure of the sputtered silver layer is the same on both substrates. The thin silver layer mainly consists of larger particles with a <1,1,1> crystal structure. However, a small number of smaller particles with a <2,0,0> crystal structure is present as well. The analysis of the AFM images of the silver surface on the germanium ATR crystal and titanium foil showed that the surfaces have similar properties. Both surfaces are polycrystalline with clear grain boundaries.

The current density vs time characteristics in the thin layer flow cell configuration show only stable behaviour for the first 100 seconds of the CO_2 reduction reaction. Due to this, only the spectra taken after one minute can be used for the comparison. From the comparison of the current density vs time characteristics, two observations became apparent. First, the current densities in the thin layer flow cell are lower than in the ATR cell but they follow the trends of the current densities in the ATR cell. Second, the current densities in the thin layer flow cell are almost constant over the first 100 seconds after reaching the applied potential. This is not the case in the ATR cell.

Investigation of the IR signal strength showed high IR signals at set angles on the ATR accessory between 30° and 45°. The maximum IR signal is found at a set angle of the ATR accessory of 36° with an aperture of the IR beam of 6 mm. The maximum intensity of the IR beam in the cell filled with air is about a factor 2.5 higher than in the cell filled with water, indicating that water indeed absorbs a large amount of IR radiation.

The FTIR absorption spectra measured in the ATR and thin layer flow cell one minute after the start of the CO_2 reduction reaction in 0.1 M KCl and 0.1 M $KHCO_3$ at the three different applied potentials are compared. The comparison of the IR absorption spectra obtained from the ATR and thin layer flow cell showed that the absorption values are larger in the IR absorption spectra measured in the thin layer flow cell than in the IR absorption spectra obtained from the ATR cell. The assignment of the IR absorption bands present in the measured IR absorption spectra are based on values found in literature. However, no In-Situ IR studies of the CO_2 reduction reaction on silver were found. Based on the proposed reaction mechanism from literature, it is expected that CO_2, CO and formate are present during the CO_2 reduction reaction. Furthermore, due to the competition of the HER, hydrogen is expected to be present as well. Since the CO_2 reduction reaction takes place in an aqueous electrolyte, water and carbonate species are also present. These molecules are common molecules in reactions of small organic molecules. Especially the oxidation of CO, methanol and formic acid. Several In-Situ IR studies of small organic molecules exist in which not silver but a different monometallic catalyst is used. The values found in literature are used to assign the IR absorption bands in this study.

There are three absorption bands present in the measured IR absorption spectra in the thin layer flow cell which are also present in the obtained IR absorption spectra of the ATR cell. These bands are assigned to dissolved carbonate, the O-H deformation of surface bound water and dissolved CO_2. In the ATR spectra however, three further IR absorption bands can be observed. These bands correspond to bidendate carbonate and linear to the silver surface bonded CO.

Due to the lower number of IR absorption bands present in the FTIR absorption spectra measured in the new designed thin layer flow cell, it can be concluded that despite the high IR signal no new insights on the reaction mechanism of the CO_2 reduction reaction can be acquired.

8. Recommendations

Based on the performed research in this study, three recommendations for future research can be given. During the performed experiments with the new designed thin layer flow cell the same problem occurred as in the ATR cell. When applying the desired potential, the sputtered electrode on the IR optical material cracked. In the ATR cell this the working electrode whereas in the thin layer flow cell it is the counter electrode sputtered on the germanium ATR crystal and calcium fluoride IR transparent window respectively. Despite the achievement of an easy exchangeable electrocatalyst, the IR transparent window still has to be removed from the cell, then cleaned by polishing the surface and subsequently a new counter electrode layer has to be deposited before a new experiment can be performed. As platinum is more expensive than silver, renewing the counter electrode before each experiment is economically unfavourable. Furthermore, due to the electrolyte flow through the cell, delamination of the cracked counter electrode layer takes place. Since the thickness of the electrolyte layer between the counter and working electrode is very small, 25 µm, loosened pieces of the counter electrode are able to get in contact with the working electrode causing a short circuit. This was the case in many experiments and is observed in the current density vs time characteristics presented in Figure 38. To prevent this problem in future experiments, the sputtered platinum counter electrode can be replaced by platinum wire. Therefore, the positions of the electrodes have to be relocated in the cell. The platinum wire counter electrode has to be placed in the electrolyte inlet and the Ag/AgCl reference electrode to the electrolyte outlet of the thin layer flow cell. To achieve this, the electrolyte in- and outlet of the cell can be changed easily by switching the teflon tubes.

From the measured FTIR absorption spectra during the CO_2 reduction reaction in the thin layer flow cell no new information on the reaction mechanism could be acquired. The ATR-IR absorption spectra show more IR absorption bands giving a more detailed view on the present species during the CO_2 reduction reaction. As discussed, this is due to how the surface of the electrocatalyst is probed with the IR beam. In ATR spectroscopy, solid samples are generally probed by pressing the sample onto the ATR crystal. In section 6.1.2.4 the penetration depth of the evanescent wave, generated at the interface of the germanium ATR crystal and silver, is calculated. In the wavenumber region of interest, 900-2400 cm^{-1}, the penetration depth of the evanescent wave is 250 nm and higher as can be seen in Figure 31. Therefore, it should be possible to probe the surface of a film with a thickness smaller than 250 nm theoretically. By pressing a film with a thickness smaller than 250 nm on the ATR crystal, the direct deposition of the film onto the ATR crystal is eliminated and thereby easy exchange of the electrocatalyst is ensured. A technique to produce self-sustaining films with a thickness of 200 nm has to be developed. When successful, the ATR experiments should then be repeated with the thin films pressed instead of sputtered onto the germanium ATR crystal under the same conditions. To validate if this hypothesis works, the obtained ATR-IR absorption spectra have to be compared with the obtained ATR-IR absorption spectra with a sputtered silver electrode.

In this study, only aqueous electrolytes are used. CO_2 however dissolves only poorly in water leading to only a low concentration of CO_2 in the aqueous electrolyte. Furthermore, water absorbs a lot of IR radiation and promotes the HER which reduces the faradic efficiency of the CO_2 reduction. To overcome these problems, electrolytes with increasing CO_2 solubility and lower proton availability could be used. Aprotic and ionic electrolytes possess these properties respectively. Research has to be performed on these types electrolytes to find appropriate electrolytes which IR absorption spectra do not interfere with the IR absorption bands of the reactants and possible intermediates and products of the CO_2 reduction reaction. In-Situ FTIR experiments of the CO_2 reduction reaction in the thin layer flow cell should be repeated with the appropriate electrolytes at same conditions as in this study to be able to investigate the differences in the IR absorption spectra. Differences in the obtained IR spectra may then provide new insights into the reaction mechanism of the CO_2 reduction reaction.

Bibliography

1. Kumar, B., et al., *New trends in the development of heterogeneous catalysts for electrochemical CO2 reduction.* Catalysis Today, 2016. **270**: p. 19-30.
2. Lu, Q. and F. Jiao, *Electrochemical CO2 reduction: Electrocatalyst, reaction mechanism, and process engineering.* Nano Energy, 2016. **29**: p. 439-456.
3. Kauffman, D.R., et al., *Efficient Electrochemical CO2 Conversion Powered by Renewable Energy.* ACS Applied Materials & Interfaces, 2015. **7**(28): p. 15626-15632.
4. Bevilacqua, M., et al., *Recent Technological Progress in CO2 Electroreduction to Fuels and Energy Carriers in Aqueous Environments.* Energy Technology, 2015. **3**(3): p. 197-210.
5. Jhong, H.-R.M., S. Ma, and P.J.A. Kenis, *Electrochemical conversion of CO2 to useful chemicals: current status, remaining challenges, and future opportunities.* Current Opinion in Chemical Engineering, 2013. **2**(2): p. 191-199.
6. Kortlever, R., et al., *Catalysts and Reaction Pathways for the Electrochemical Reduction of Carbon Dioxide.* The Journal of Physical Chemistry Letters, 2015. **6**(20): p. 4073-4082.
7. Murata, A. and Y. Hori, *Product selectivity affected by cationic species in electrochemical reduction of CO2 and CO at a Cu electrode.* Bulletin of the Chemical Society of Japan, 1991. **64**(1): p. 123-127.
8. Hori, Y., et al., *Electrocatalytic process of CO selectivity in electrochemical reduction of CO2 at metal electrodes in aqueous media.* Electrochimica Acta, 1994. **39**(11): p. 1833-1839.
9. Hatsukade, T., et al., *Insights into the electrocatalytic reduction of CO2 on metallic silver surfaces.* Physical Chemistry Chemical Physics, 2014. **16**(27): p. 13814-13819.
10. Bruice, P.Y., *Organic chemistry*. 2010: Prentice Hall.
11. Reichenbächer, M. and J. Popp, *Vibrational Spectroscopy*, in *Challenges in Molecular Structure Determination*. 2012, Springer Berlin Heidelberg: Berlin, Heidelberg. p. 63-143.
12. Weckhuysen, B.M., *In-situ Spectroscopy of Catalysts*. 2004: American Scientific Publishers.
13. Aroca, R., *Surface-Enhanced Vibrational Spectroscopy*. 2006: Wiley.
14. Ye, J.-Y., et al., *In-situ FTIR spectroscopic studies of electrocatalytic reactions and processes.* Nano Energy, 2016. **29**: p. 414-427.
15. Zhou, Z.-Y., et al., *In situ rapid-scan time-resolved microscope FTIR spectroelectrochemistry: study of the dynamic processes of methanol oxidation on a nanostructured Pt electrode.* Journal of Electroanalytical Chemistry, 2004. **573**(1): p. 111-119.
16. Shi, H., J.A. Lercher, and X.-Y. Yu, *Sailing into uncharted waters: recent advances in the in situ monitoring of catalytic processes in aqueous environments.* Catalysis Science & Technology, 2015. **5**(6): p. 3035-3060.
17. Zaera, F., *New advances in the use of infrared absorption spectroscopy for the characterization of heterogeneous catalytic reactions.* Chemical Society Reviews, 2014. **43**(22): p. 7624-7663.
18. Chen, Y.X., et al., *Kinetics and Mechanism of the Electrooxidation of Formic Acid—Spectroelectrochemical Studies in a Flow Cell.* Angewandte Chemie International Edition, 2006. **45**(6): p. 981-985.
19. Matsui, T., et al., *In Situ Attenuated Total Reflection Infrared Spectroscopy on Electrochemical Ammonia Oxidation over Pt Electrode in Alkaline Aqueous Solutions.* Langmuir, 2015. **31**(42): p. 11717-11723.
20. Ataka, K.-i., T. Yotsuyanagi, and M. Osawa, *Potential-Dependent Reorientation of Water Molecules at an Electrode/Electrolyte Interface Studied by Surface-Enhanced Infrared Absorption Spectroscopy.* The Journal of Physical Chemistry, 1996. **100**(25): p. 10664-10672.
21. Kanamura, K., et al., *Oxidation of propylene carbonate containing LiBF4 or LiPF6 on LiCoO2 thin film electrode for lithium batteries.* Electrochimica Acta, 2001. **47**(3): p. 433-439.

22. Machan, C.W., et al., *Developing a Mechanistic Understanding of Molecular Electrocatalysts for CO2 Reduction using Infrared Spectroelectrochemistry.* Organometallics, 2014. **33**(18): p. 4550-4559.
23. You, L.-X., et al., *Mechanism of electro-catalytic oxidation of shikimic acid on Cu electrode based on in situ FTIRS and theoretical calculations.* Electrochimica Acta, 2011. **58**: p. 165-171.
24. Zhou, Z.-Y., et al., *In situ step-scan time-resolved microscope FTIR spectroscopy working with a thin-layer cell.* Electrochemistry Communications, 2005. **7**(5): p. 490-495.
25. Zandi, O. and T.W. Hamann, *Determination of photoelectrochemical water oxidation intermediates on haematite electrode surfaces using operando infrared spectroscopy.* Nat Chem, 2016. **8**(8): p. 778-783.
26. Zhou, Z.-Y., et al., *In situ FTIR spectroscopic studies of electrooxidation of ethanol on Pd electrode in alkaline media.* Electrochimica Acta, 2010. **55**(27): p. 7995-7999.
27. Smolinka, T., et al., *CO2 reduction on Pt electrocatalysts and its impact on H2 oxidation in CO2 containing fuel cell feed gas – A combined in situ infrared spectroscopy, mass spectrometry and fuel cell performance study.* Electrochimica Acta, 2005. **50**(25): p. 5189-5199.
28. Busó-Rogero, C., et al., *Ethanol oxidation on shape-controlled platinum nanoparticles at different pHs: A combined in situ IR spectroscopy and online mass spectrometry study.* Journal of Electroanalytical Chemistry, 2016. **763**: p. 116-124.
29. Heinen, M., et al., *In situ ATR-FTIRS coupled with on-line DEMS under controlled mass transport conditions—A novel tool for electrocatalytic reaction studies.* Electrochimica Acta, 2007. **52**(18): p. 5634-5643.
30. Hori, Y., et al., *Infrared spectroscopy of adsorbed CO and intermediate species in electrochemical reduction of CO2 to hydrocarbons on a Cu electrode.* Electrochimica Acta, 1995. **40**(16): p. 2617-2622.
31. Collins, S.E., M.A. Baltanás, and A.L. Bonivardi, *An infrared study of the intermediates of methanol synthesis from carbon dioxide over Pd/β-Ga2O3.* Journal of Catalysis, 2004. **226**(2): p. 410-421.
32. Baruch, M.F., et al., *Mechanistic Insights into the Reduction of CO2 on Tin Electrodes using in Situ ATR-IR Spectroscopy.* ACS Catalysis, 2015. **5**(5): p. 3148-3156.
33. Pander, J.E., M.F. Baruch, and A.B. Bocarsly, *Probing the Mechanism of Aqueous CO2 Reduction on Post-Transition-Metal Electrodes using ATR-IR Spectroelectrochemistry.* ACS Catalysis, 2016. **6**(11): p. 7824-7833.
34. Heyes, J., M. Dunwell, and B. Xu, *CO2 Reduction on Cu at Low Overpotentials with Surface-Enhanced in Situ Spectroscopy.* The Journal of Physical Chemistry C, 2016. **120**(31): p. 17334-17341.
35. Gao, D., et al., *Switchable CO2 electroreduction via engineering active phases of Pd nanoparticles.* Nano Research, 2017. **10**(6): p. 2181-2191.
36. Kumar, R., et al., *Application of the ATR-IR Spectroscopic Technique to the Characterization of Hydrates Formed by CO2, CO2/H2 and CO2/H2/C3H8.* The Journal of Physical Chemistry A, 2009. **113**(22): p. 6308-6313.
37. Gravejat, P., et al., *Heats of Adsorption of Linear and Bridged CO Species Adsorbed on a 3% Ag/Al2O3 Catalyst Using in situ FTIR Spectroscopy under Adsorption Equilibrium.* The Journal of Physical Chemistry C, 2007. **111**(26): p. 9496-9503.
38. Yang, Y.-Y., et al., *Infrared Spectroelectrochemical Study of Dissociation and Oxidation of Methanol at a Palladium Electrode in Alkaline Solution.* Langmuir, 2013. **29**(5): p. 1709-1716.
39. Chen, Y.X., et al., *Application of In-situ Attenuated Total Reflection-Fourier Transform Infrared Spectroscopy for the Understanding of Complex Reaction Mechanism and Kinetics: Formic Acid Oxidation on a Pt Film Electrode at Elevated Temperatures.* The Journal of Physical Chemistry B, 2006. **110**(19): p. 9534-9544.

40. Vigier, F., et al., *On the mechanism of ethanol electro-oxidation on Pt and PtSn catalysts: electrochemical and in situ IR reflectance spectroscopy studies.* Journal of Electroanalytical Chemistry, 2004. **563**(1): p. 81-89.
41. Firet, N.J. and W.A. Smith, *Probing the Reaction Mechanism of CO2 Electroreduction over Ag Films via Operando Infrared Spectroscopy.* ACS Catalysis, 2017. **7**(1): p. 606-612.
42. Klähn, M., et al., *IR Spectra of Phosphate Ions in Aqueous Solution: Predictions of a DFT/MM Approach Compared with Observations.* The Journal of Physical Chemistry A, 2004. **108**(29): p. 6186-6194.
43. Chen, Y., Y.-H. Zhang, and L.-J. Zhao, *ATR-FTIR spectroscopic studies on aqueous LiClO4, NaClO4, and Mg(ClO4)2 solutions.* Physical Chemistry Chemical Physics, 2004. **6**(3): p. 537-542.
44. Li, H., *Refractive index of silicon and germanium and its wavelength and temperature derivatives.* Journal of Physical and Chemical Reference Data, 1980. **9**(3): p. 561-658.
45. Babar, S. and J.H. Weaver, *Optical constants of Cu, Ag, and Au revisited.* Applied Optics, 2015. **54**(3): p. 477-481.
46. García, G., et al., *Fourier Transform Infrared Spectroscopy Study of CO Electro-oxidation on Pt(111) in Alkaline Media.* Langmuir, 2009. **25**(23): p. 13661-13666.
47. Khosravani, S., et al., *The effect of various oxidation temperatures on structure of Ag-TiO2 thin film.* Microelectronic Engineering, 2016. **163**: p. 67-77.

Appendix

I. FTIR absorption spectra measured in the ATR cell

0.1 M KCl

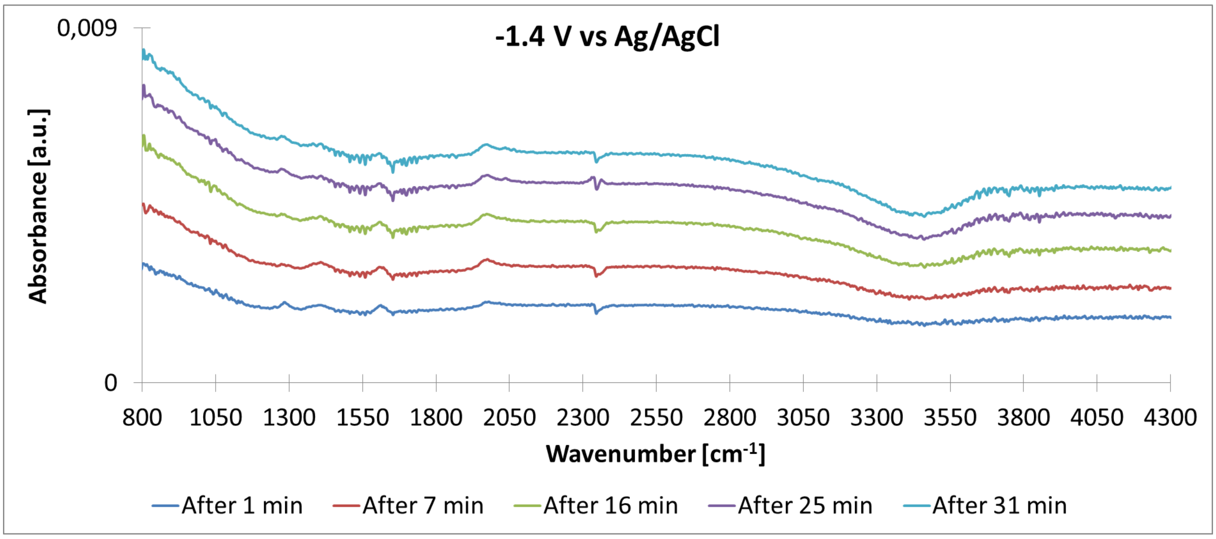

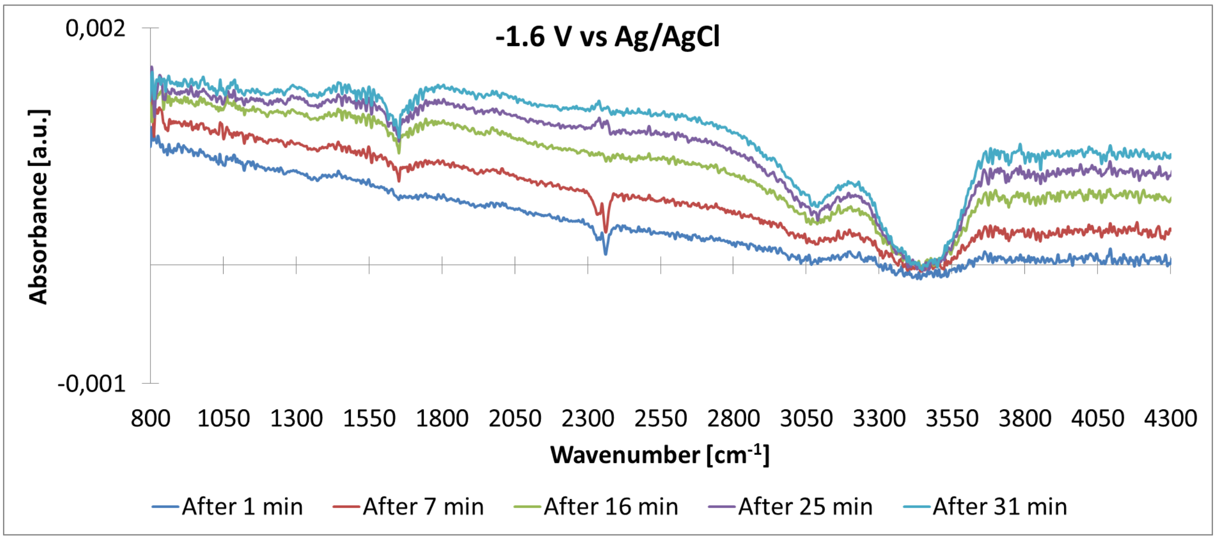

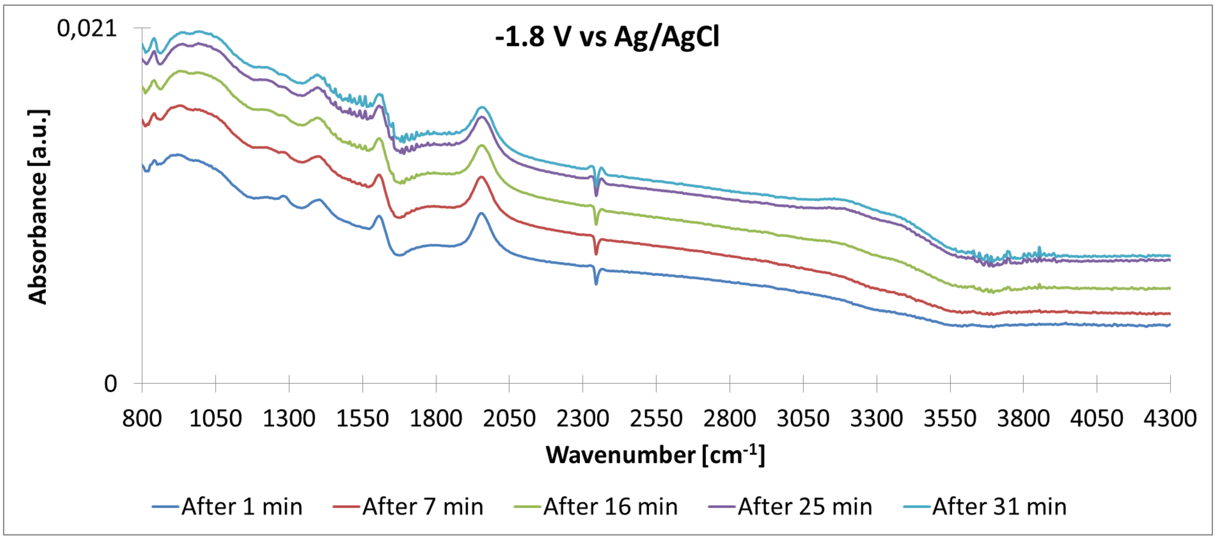

0.1 M $KHCO_3$

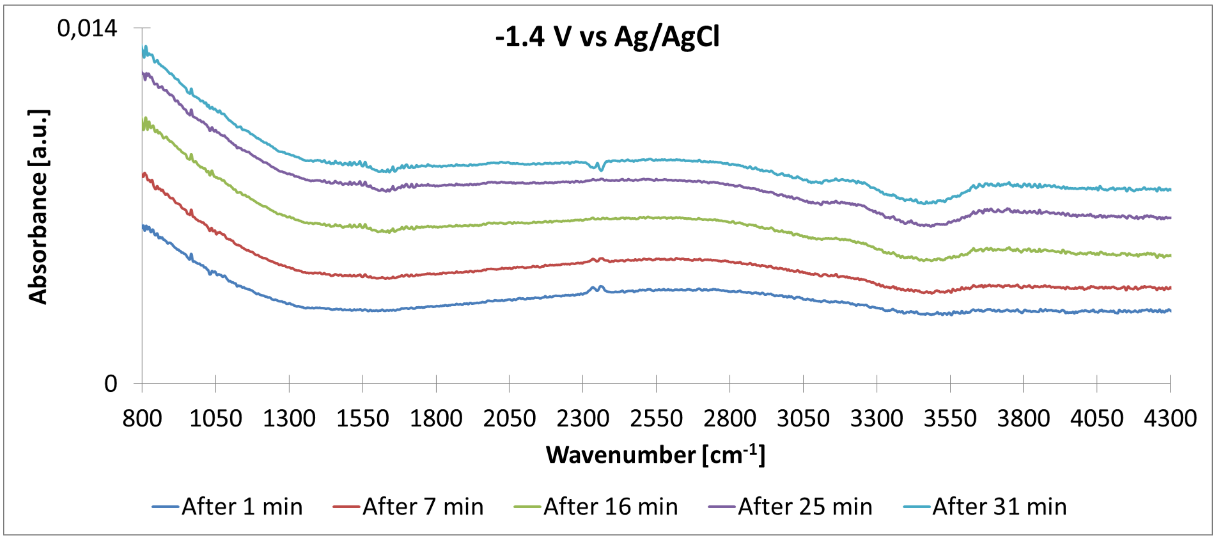
-1.4 V vs Ag/AgCl
0,014
0
Absorbance [a.u.]
800
1050
1300
1550
1800
2050
2300
2550
2800
3050
3300
3550
3800
4050
4300
Wavenumber [cm-1]
After 1 min
After 7 min
After 16 min
After 25 min
After 31 min

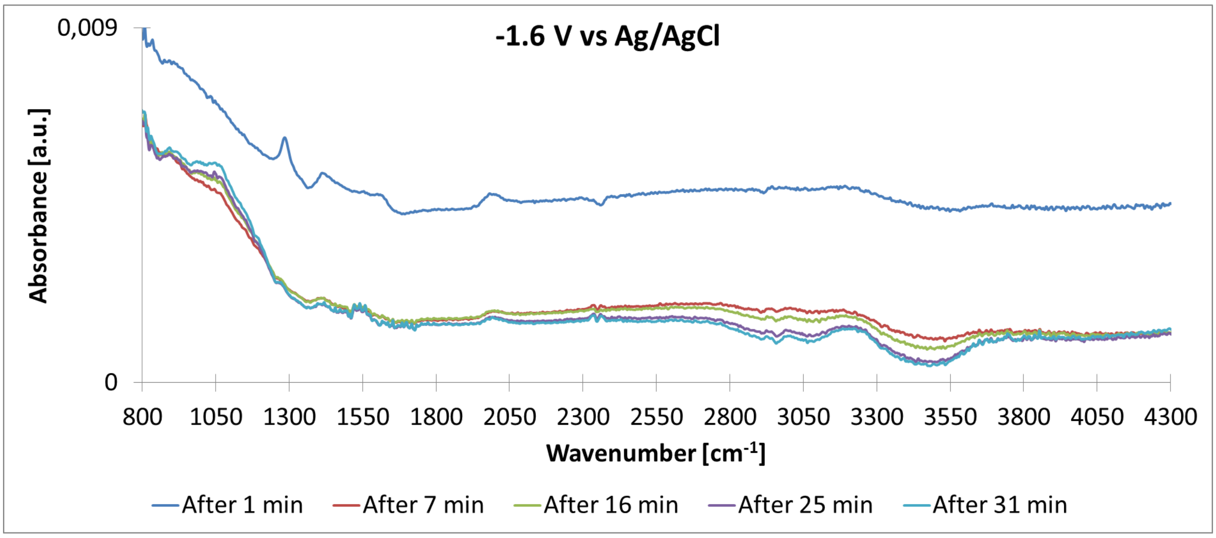
-1.6 V vs Ag/AgCl
0,009
0
Absorbance [a.u.]
800
1050
1300
1550
1800
2050
2300
2550
2800
3050
3300
3550
3800
4050
4300
Wavenumber [cm-1]
After 1 min
After 7 min
After 16 min
After 25 min
After 31 min

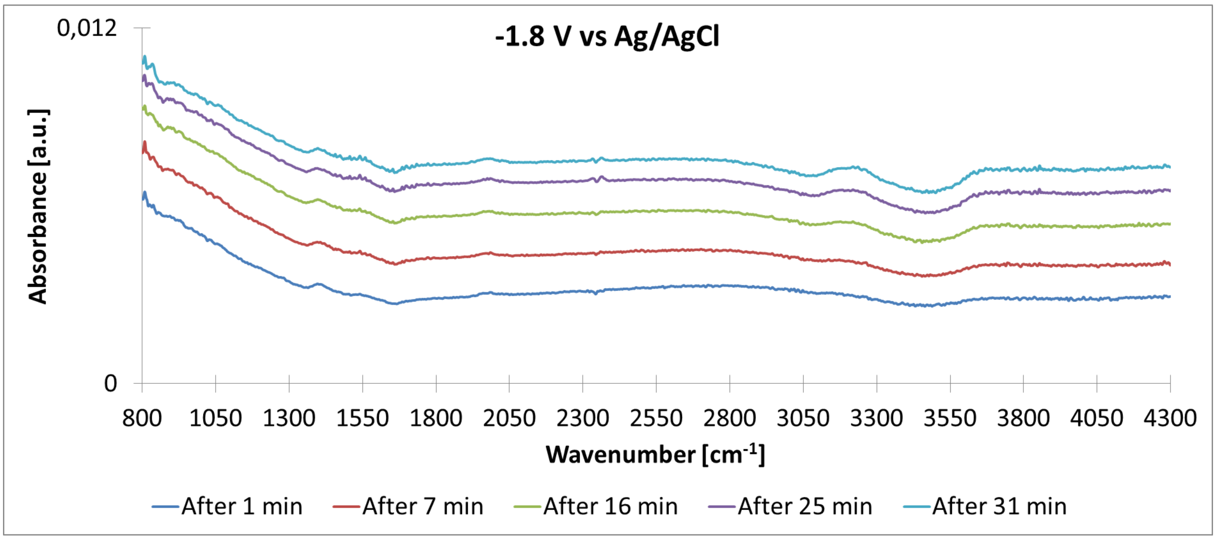
-1.8 V vs Ag/AgCl
0,012
0
Absorbance [a.u.]
800
1050
1300
1550
1800
2050
2300
2550
2800
3050
3300
3550
3800
4050
4300
Wavenumber [cm-1]
After 1 min
After 7 min
After 16 min
After 25 min
After 31 min

0.1 M K_2HPO_4

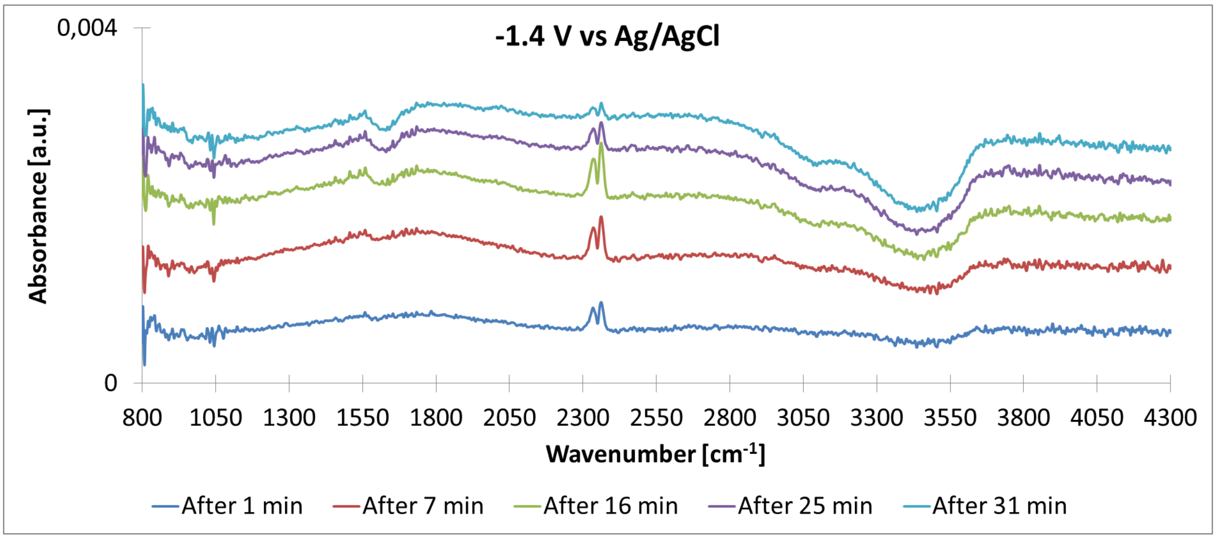
-1.4 V vs Ag/AgCl
0,004
0
Absorbance [a.u.]
800 1050 1300 1550 1800 2050 2300 2550 2800 3050 3300 3550 3800 4050 4300
Wavenumber [cm-1]
After 1 min
After 7 min
After 16 min
After 25 min
After 31 min

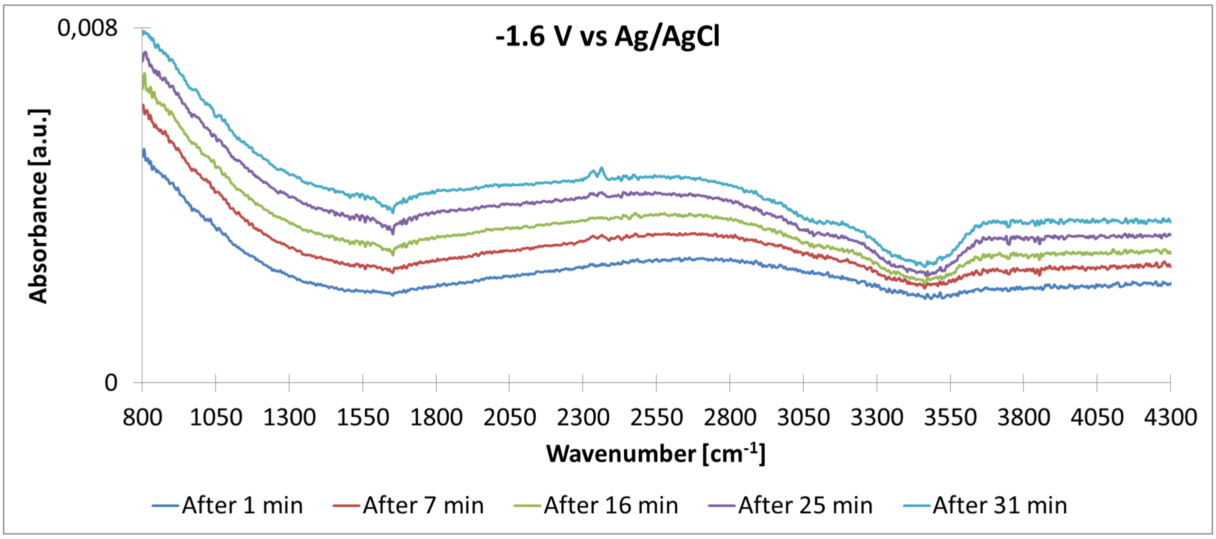
-1.6 V vs Ag/AgCl
0,008
0
Absorbance [a.u.]
800 1050 1300 1550 1800 2050 2300 2550 2800 3050 3300 3550 3800 4050 4300
Wavenumber [cm-1]
After 1 min
After 7 min
After 16 min
After 25 min
After 31 min

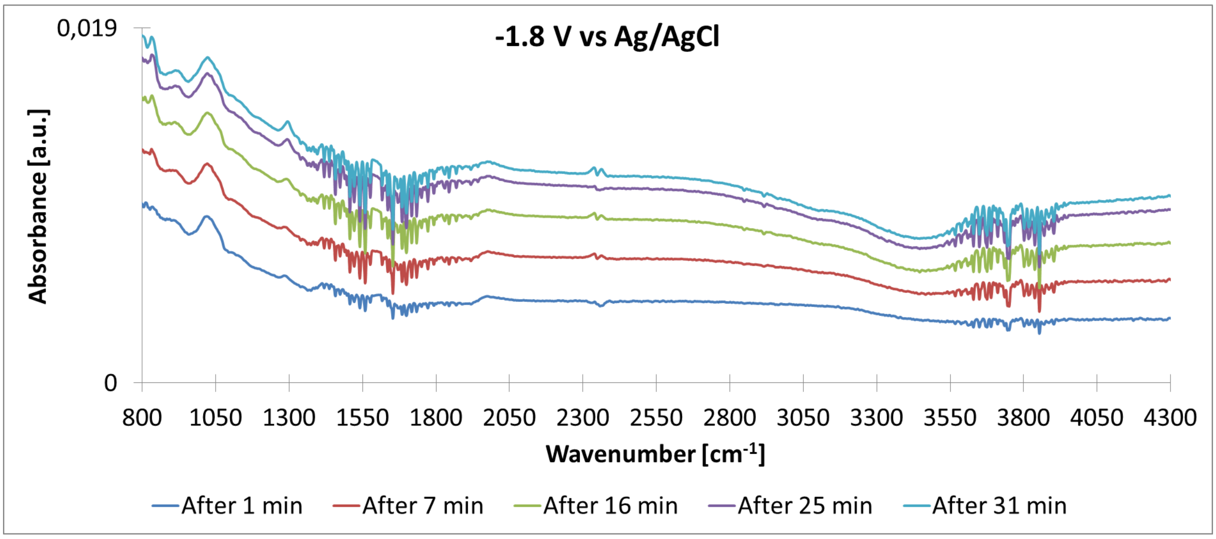
-1.8 V vs Ag/AgCl
0,019
0
Absorbance [a.u.]
800 1050 1300 1550 1800 2050 2300 2550 2800 3050 3300 3550 3800 4050 4300
Wavenumber [cm-1]
After 1 min
After 7 min
After 16 min
After 25 min
After 31 min

0.1 M $KClO_4$

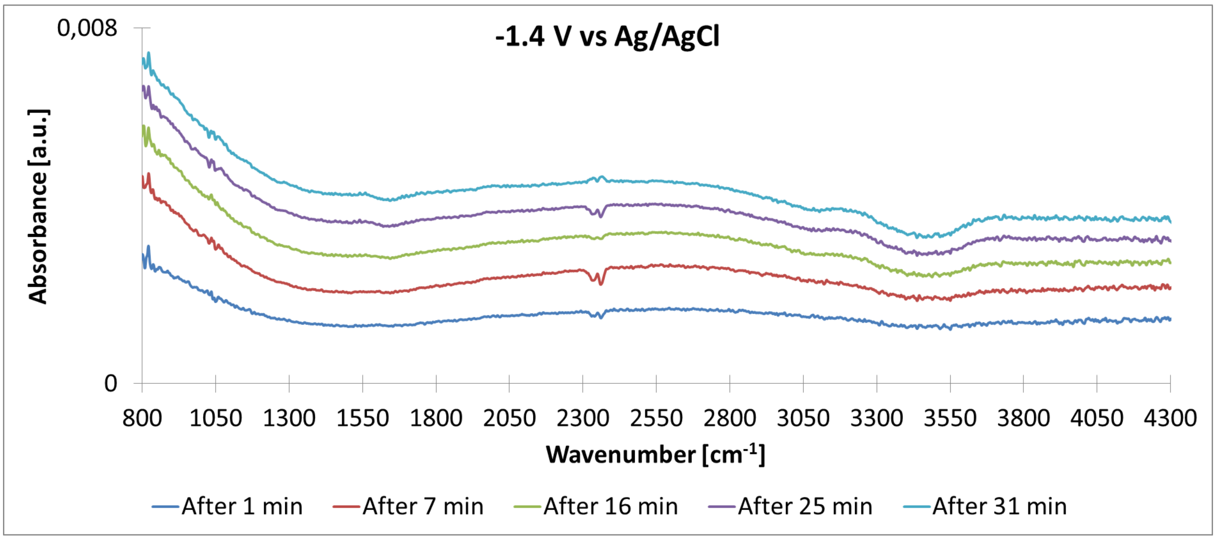
-1.4 V vs Ag/AgCl
0,008
0
Absorbance [a.u.]
800
1050
1300
1550
1800
2050
2300
2550
2800
3050
3300
3550
3800
4050
4300
Wavenumber [cm-1]
After 1 min
After 7 min
After 16 min
After 25 min
After 31 min

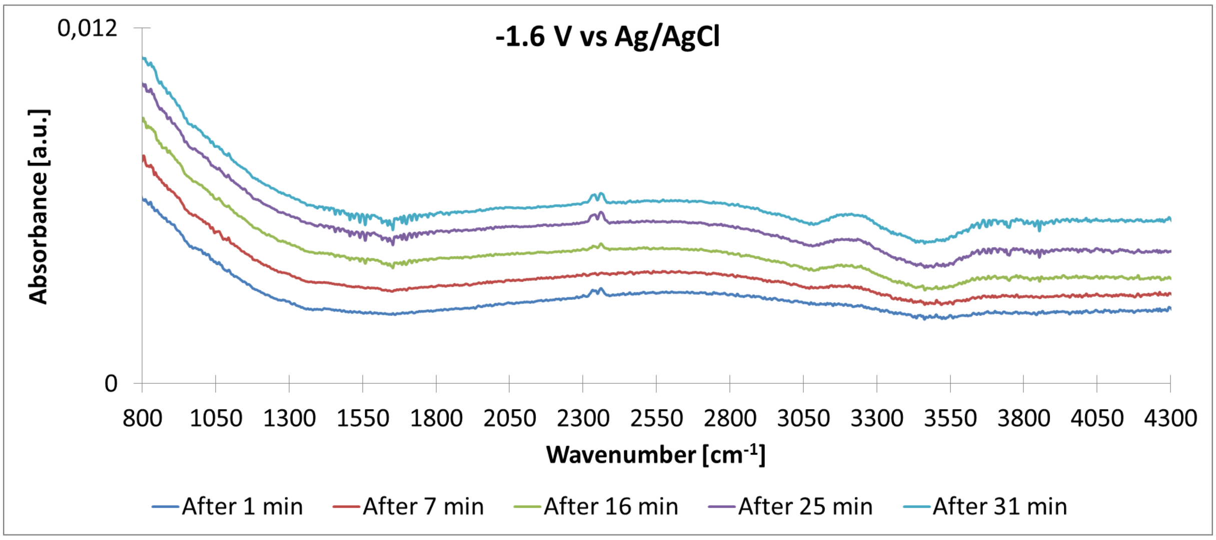
-1.6 V vs Ag/AgCl
0,012
0
Absorbance [a.u.]
800
1050
1300
1550
1800
2050
2300
2550
2800
3050
3300
3550
3800
4050
4300
Wavenumber [cm-1]
After 1 min
After 7 min
After 16 min
After 25 min
After 31 min

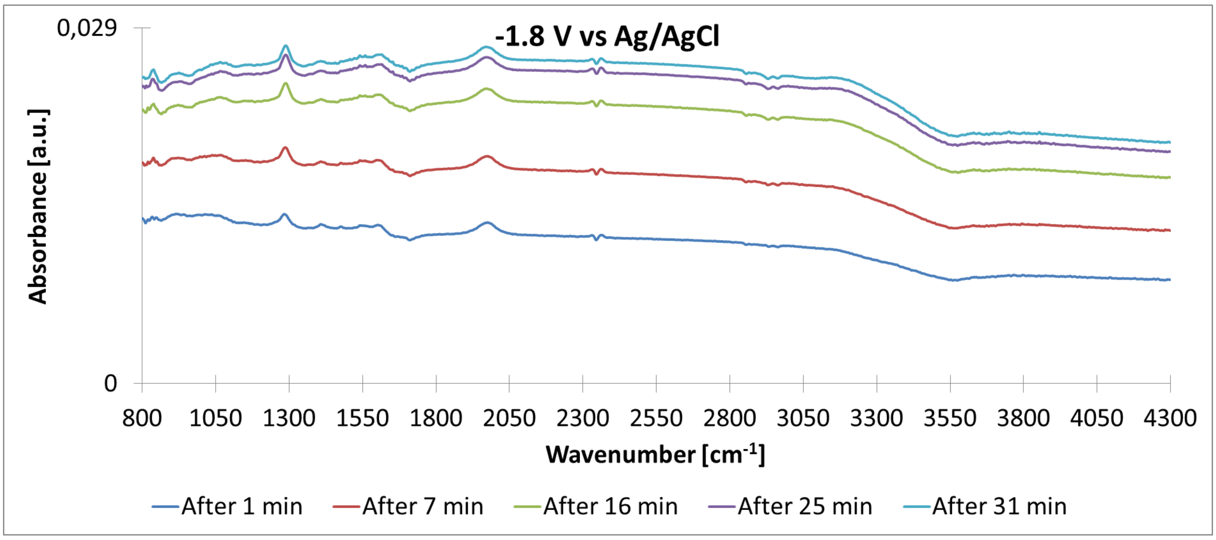
-1.8 V vs Ag/AgCl
0,029
0
Absorbance [a.u.]
800
1050
1300
1550
1800
2050
2300
2550
2800
3050
3300
3550
3800
4050
4300
Wavenumber [cm-1]
After 1 min
After 7 min
After 16 min
After 25 min
After 31 min

II. FTIR absorption spectra measured in the thin layer flow cell

0.1 M KCl

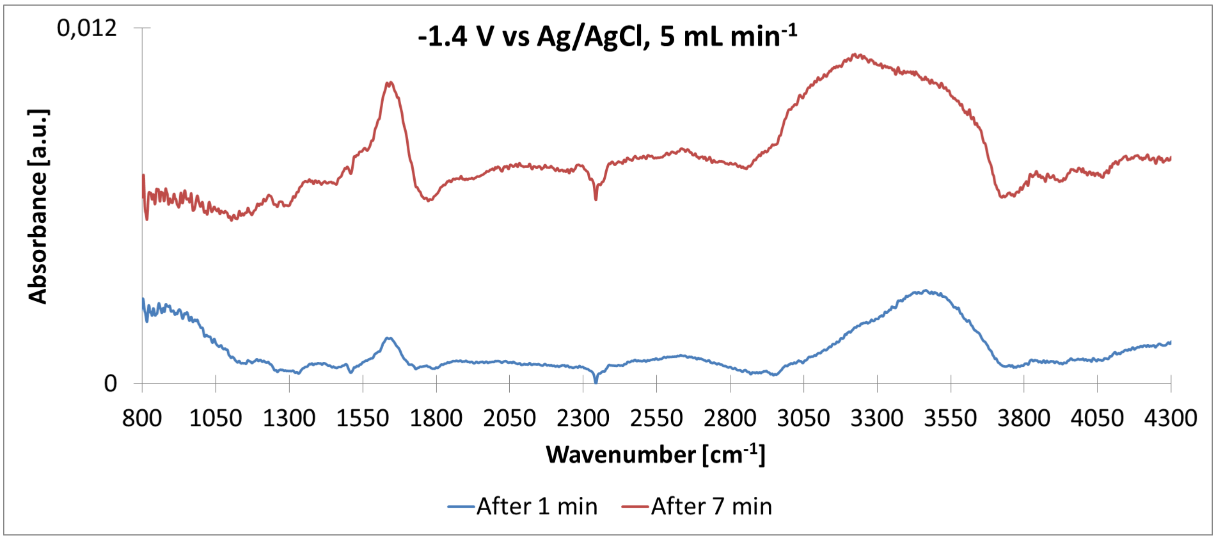

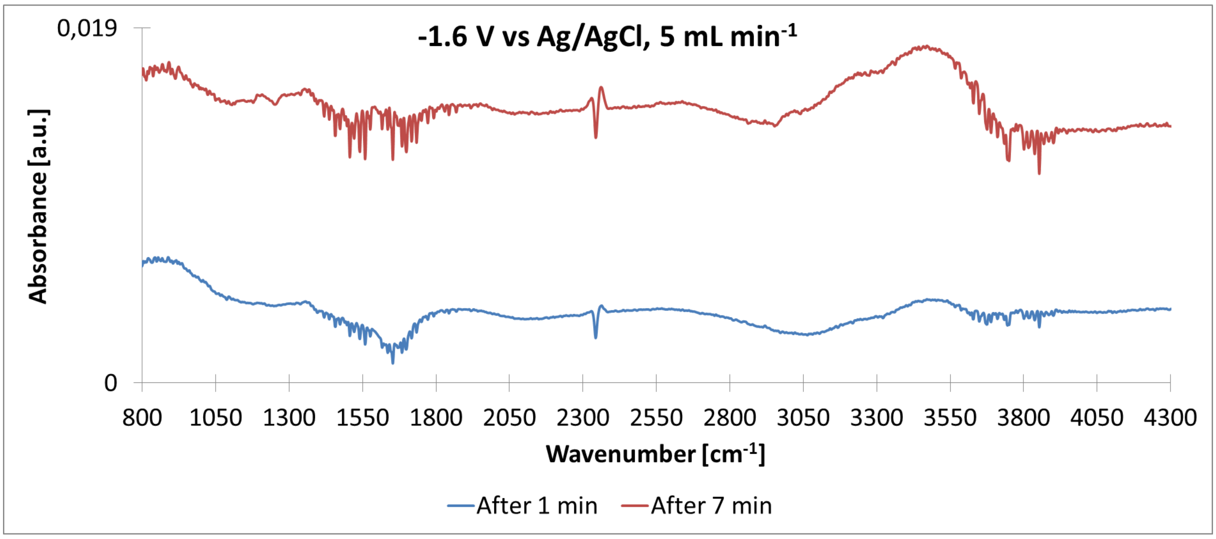

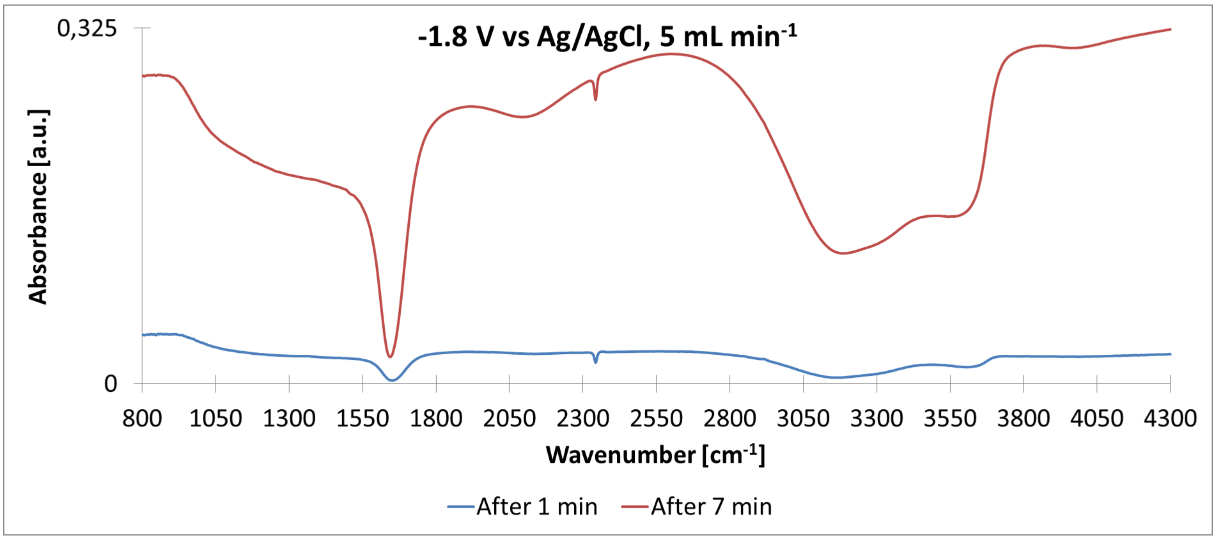

0.1 M $KHCO_3$

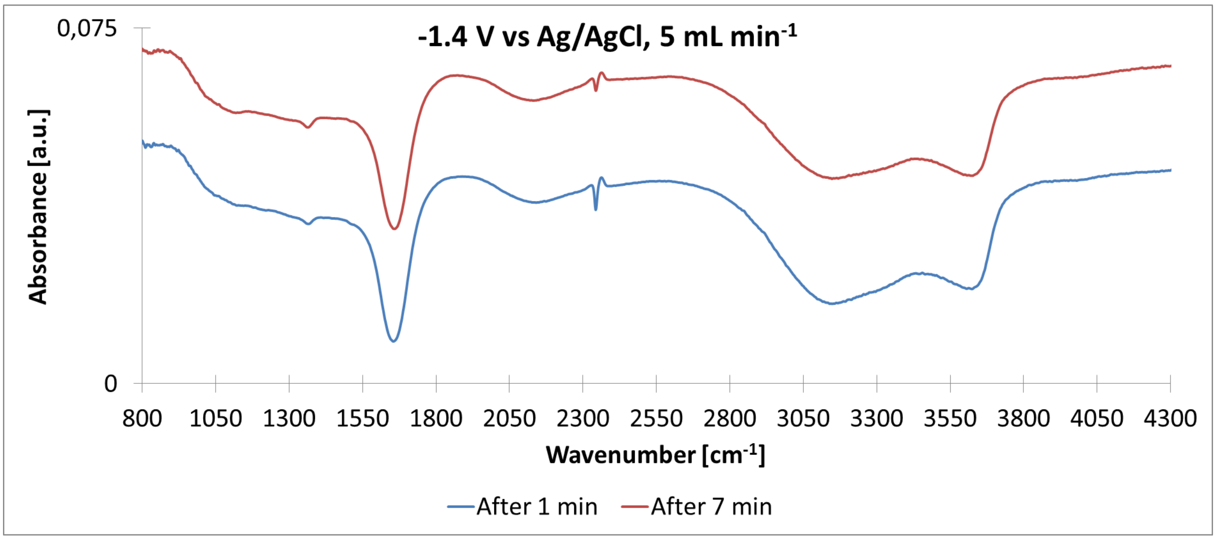
-1.4 V vs Ag/AgCl, 5 mL min-1
Absorbance [a.u.]
0,075
0
800
1050
1300
1550
1800
2050
2300
2550
2800
3050
3300
3550
3800
4050
4300
Wavenumber [cm-1]
After 1 min
After 7 min

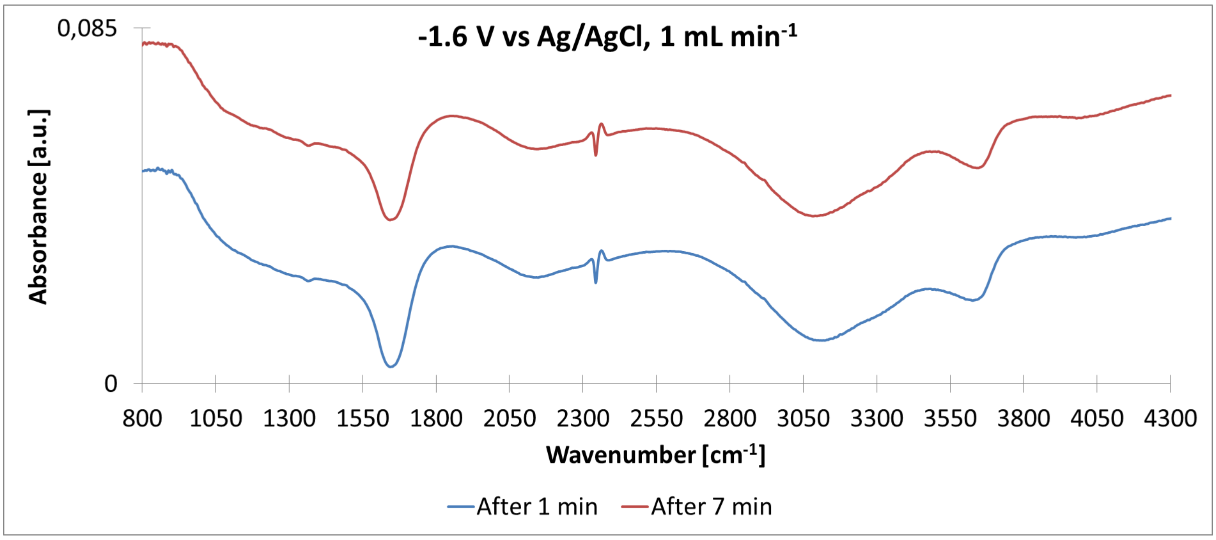
-1.6 V vs Ag/AgCl, 1 mL min-1
Absorbance [a.u.]
0,085
0
800
1050
1300
1550
1800
2050
2300
2550
2800
3050
3300
3550
3800
4050
4300
Wavenumber [cm-1]
After 1 min
After 7 min

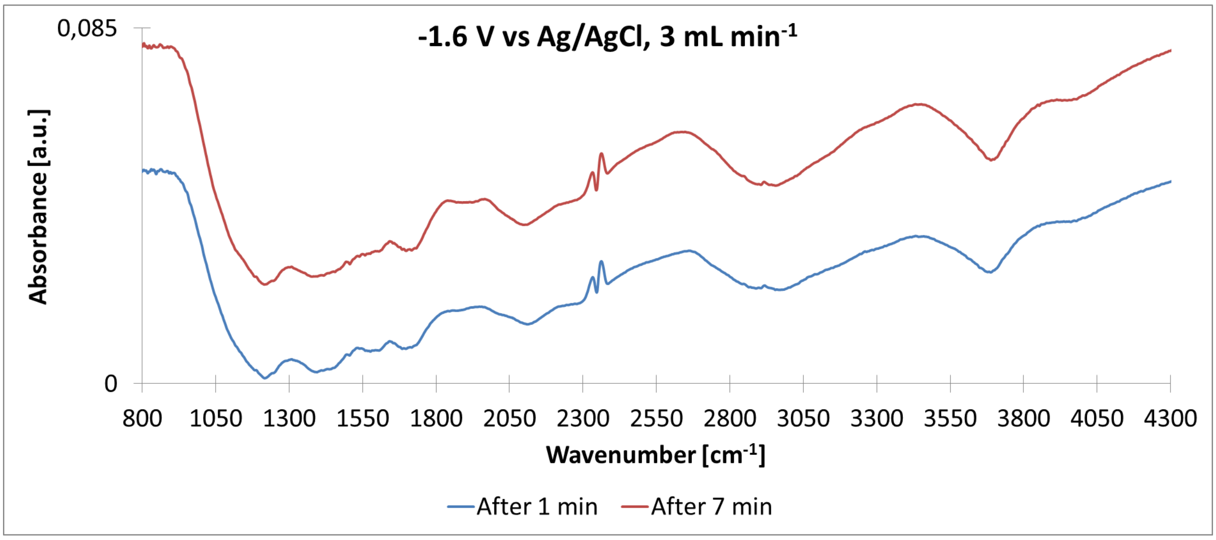
-1.6 V vs Ag/AgCl, 3 mL min-1
Absorbance [a.u.]
0,085
0
800
1050
1300
1550
1800
2050
2300
2550
2800
3050
3300
3550
3800
4050
4300
Wavenumber [cm-1]
After 1 min
After 7 min

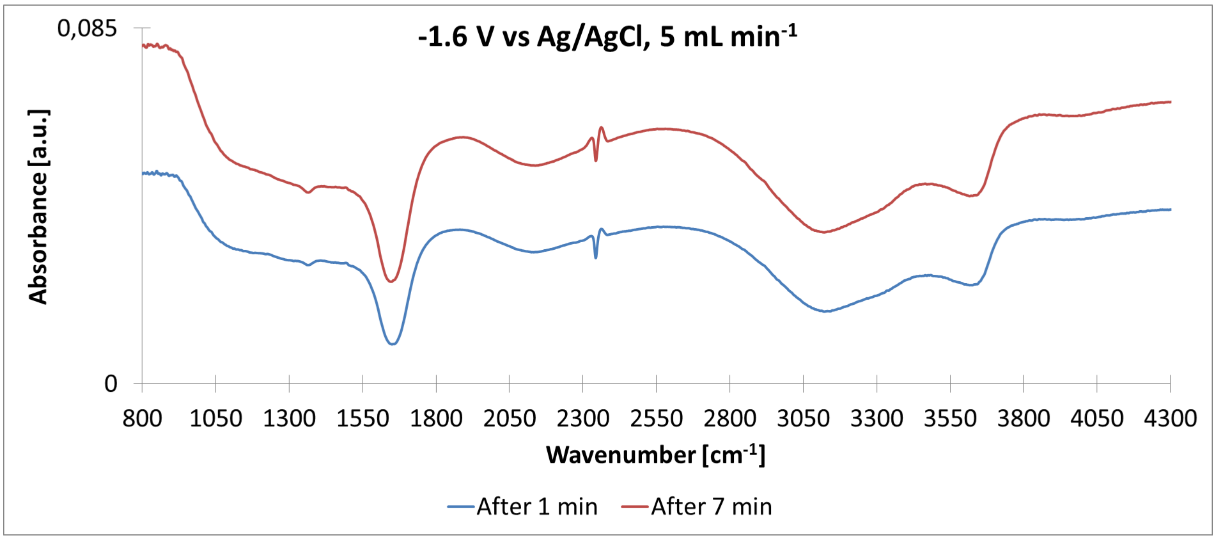
-1.6 V vs Ag/AgCl, 5 mL min^{-1}
Absorbance [a.u.]
0,085
0
800
1050
1300
1550
1800
2050
2300
2550
2800
3050
3300
3550
3800
4050
4300
Wavenumber [cm^{-1}]
After 1 min
After 7 min

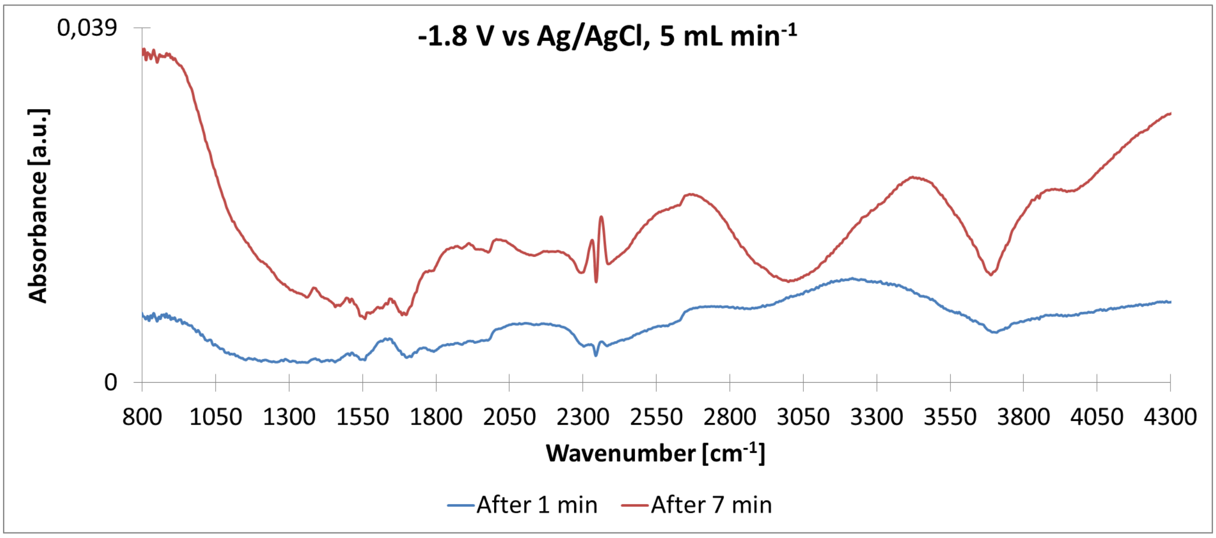
-1.8 V vs Ag/AgCl, 5 mL min^{-1}
Absorbance [a.u.]
0,039
0
800
1050
1300
1550
1800
2050
2300
2550
2800
3050
3300
3550
3800
4050
4300
Wavenumber [cm^{-1}]
After 1 min
After 7 min